Design, simulation, fabrication and measurement of a superconducting microwave resonator allowing the application of a DC bias through a symmetry point

P.M.L Gimbel

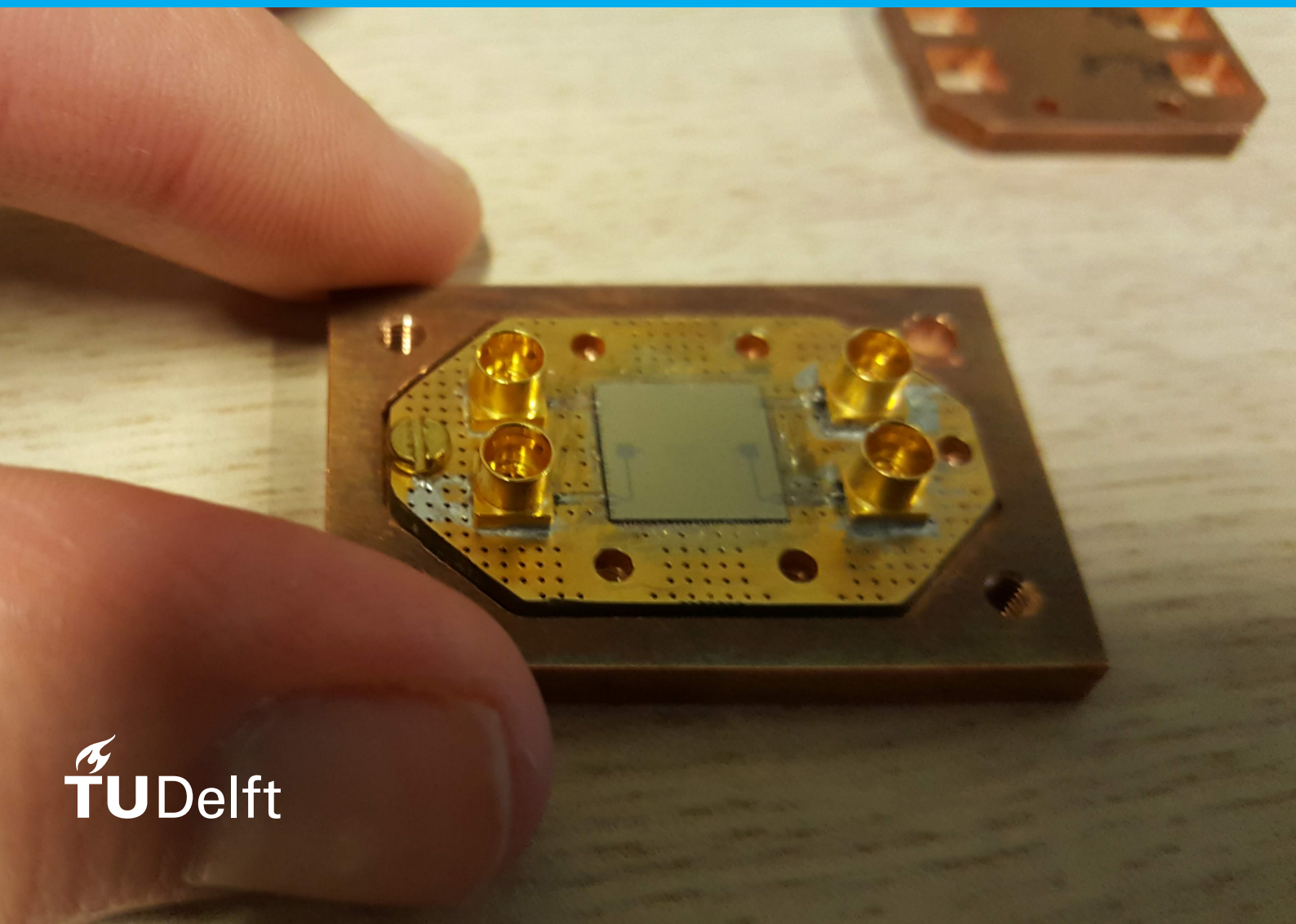

TU Delft

Design, simulation, fabrication and measurement of a superconducting microwave resonator allowing the application of a DC bias through a symmetry point

by

P.M.L Gimbel

to obtain the degree of Master of Science
at the Delft University of Technology,
to be defended publicly on Friday May 29, 2020 at 1:30 PM.

Student number:	4166965	
Project duration:	March 17, 2018 – May 19, 2020	
Thesis committee:	Prof. dr. ir. G.A. Steele,	TU Delft, supervisor
	Prof. dr. ir. L. M. K. Vandersypen,	TU Delft
	Dr. ir. J. M. Thijssen,	TU Delft

An electronic version of this thesis is available at `http://repository.tudelft.nl/`.

TU Delft

Abstract

Superconducting microwave resonators based on coplanar waveguides (CPWs), which allow for on-chip implementation, have a wide variety of uses, from the coupling of qubits to the detection of photons from interstellar clouds. With the integration of a bias circuitry, the already versatile resonator will become even more so. However, applying a DC voltage or current bias to the resonator without significantly degrading its quality factor Q is no trivial task.

One of the first superconducting microwave resonators with the ability to allow for the application of a DC bias, made use of symmetry points. In order to not rely on those symmetry points, our group came up with a different design that used a shunted capacitor instead. However, this design needs a more extensive and in particular more complicated fabrication process. As the groups focus is now completely away from the original design, we go back in this thesis, to honestly evaluate such a resonator by applying a bias to its center.

We present a design with the cavity length l to be a full wavelength ($l = \lambda$) terminated on both ends to ground, fed in by a capacitively coupled AC-feedline at $\lambda/4$ and a DC-bias line at its center ($\lambda/2$). After the first fabrication trial we were unable to successfully judge the performance of the microwave resonator as it suffered from bad internal loss, leading to a low internal $Q \sim 300$ at 4 K. The only thing that this showed us, is that its design is perhaps not as straightforward. On the other hand, interesting results specific to the design were obtained from QUCS simulations (using a combination of lumped and distributed elements). These simulations showed that the quality of the resonator is highly sensitive to the position of its galvanically connected bias line, with respect to the center of the cavity (voltage node). Where Q_{int} drops down to 10% of its maximum for < 0.1 mm ($= l/320$) away from the center. Furthermore, we saw that asymmetry in the ports causes the maximum Q_{int} (voltage node) to be off-center by 9 μm, and that adding an extra feedline in symmetry to the existing one puts it back on-center. Demonstrating the voltage node susceptibility to asymmetries of the cavity mode.

Despite the unpromising signs the results show, suggestions have been put forward about better isolation of the bias line that have the potential to still make the design attractive. While these isolations still baring the traits of a faster and less complex fabrication.

Acknowledgements

It was not the most straightforward path that led to the project at hand. When I started the master thesis more than two years ago, we were not concerned with microwave resonators, but with the fabrication of Josephson junctions. The fabrication was supposed to be done by atomic layer deposition (ALD), which in theory was perfectly suited for the in-situ stacking of the layers of these junctions. I took on this project under the guidance of Felix Schmidt and Mark Jenkins. Who I would like to thank for helping me throughout the project. Teaching me the necessary skills in the cleanroom, which they seem to know like the back of their hands. They provided me with the required knowledge and tools, and were always willing to answer any questions I had.

As the project progressed the prospect of a useful outcome became dimmer and dimmer. The ALD seemed to be chronically ill, suffering from many failures with only a temporary cure. Even with the great expertise of Marc Zuiddam in everything concerning the ALD and Alessandro Bruno's expertise in growing the desired layers, it remained a struggle. Their help and assistance is much appreciated. In the final stages of the project Marc and I spent an increasingly amount of time on the ALD to keep the system up and running. I was spending so much time on the ALD, to a point that I was even teaching people the necessary operating details in order for them to grant access to the machine. After more than half a year of trying, we had almost nothing to show for. Although I really enjoyed working in the cleanroom and it was difficult to accept that we wasted all that time, we had to abandon the project.

Once we dropped the previous project, we started afresh. This was the point where we began to study (DC accessible) microwave resonators, the subject of this thesis. To kick things of, Mark Jenkins used his last two weeks at the university to fabricate and measure the device with me, for which I am thankful. Prof. Gary Steele who was already involved in the other project took on full supervision. His help and assistance was much more than anybody could wish for. From a weekly face to face meeting to answering chats in the middle of the night, or even in the weekends. I am very grateful for his guidance and I can only admire his involvement knowing how busy his agenda is. The quote of Benjamin Franklin seems to be in place: 'If you want something done, ask a busy person'. And all that, taking in mind that the thesis looked like a never ending story with me taking a considerably more time than I supposed to. So, I also would like to thank Gary for all his patience.

Lastly, I would like to thank my family and friends. Roel Horeman for the endless talks and sometimes fruitful discussions we had during the coffee and lunch breaks. My parents and my sisters for their support. Emma and Martien van Winden for allowing me to study at their home, where I was finally able to finish the thesis in a full week of complete isolation. In that way the corona crisis we are still currently in, did not make a difference then. But it certainly will during the defence, which will be held without an audience. Something that I have never done or seen before. And last, but certainly not least, a special thanks to my beautiful girlfriend Jacky for her love and support. And to my wonderful son Roger, who has been my greatest motivation since the day he was born, more than 8 months ago.

Contents

1 Introduction

From going back and forth on a swing to the precise ticking of your watch, resonators play an important role in everyday life. For a swing it is the transfer of potential to kinetic energy that allows it to resonate, whereas for the watch it is the interchange between the electric field and the deformation of the quartz. Generally speaking, a resonator is a device that oscillates energy back and forth from one form to another at a well defined frequency. Resonators play also a very important role in microwave engineering, which finds its origin in 1873 with James Clerk Maxwell's idea that light was a form of electromagnetic energy. But it was not until the invention of radar during World War II that the field of microwave engineering got serious attention. Thirty years earlier in 1911, the Dutch scientist Heike Kamerlingh Onnes discovered the phenomenon that for certain materials caused the DC electrical resistance to vanish, the AC losses to get extremely small and any external static magnetic fields to be expelled, and called it superconductivity. The use of superconductivity in microwave circuits has led to low loss (high-Q) resonators [1]. It is in these superconducting microwave resonators based on coplanar waveguides (CPWs), to allow for on chip implementation by means of lithography, that we are interested in this thesis. And in particular, one that is DC accessible.

Nowadays, superconducting CPW microwave resonator(/cavities) are subject of intense study and are used for a wide variety of applications. At cryogenic temperatures of the order of millikelvin and operating frequencies of > GHz these resonators are firmly in their ground state. Enabling them to provide thermal isolation to embedded system and facilitating non-destructive readout at microwave frequencies. This makes them perfect candidates for the integration of quantum systems such as qubits [2–4] and to function as a quantum bus [5, 6]. For the same reason they play a key-role in the study of interaction between matter and light in circuit quantum electrodynamics (QED) [7, 8]. Furthermore, their superconducting nature makes it possible to change their kinetic inductance, which in turn changes the resonance frequency. In combination with having quality factors on the orders of a million, they are able to detect photons [9, 10] and the motion of nanomechanical resonators (NRs) [11]. And are even able to cool the NRs down by up-conversion of the microwave photons [12]. Although this is already an impressive array of uses, allowing for the introduction of a DC-bias will add another function to the resonator, making it even more versatile. With the additional DC access the resonance of the cavity can now be tuned in a controllable manner to couple/decouple qubits [13], or uncontrollably to detect currents via kinetic inductance or vice versa [14]. Besides, it could form a bridge between the already mentioned microwave based circuit QED and DC quantum transport [15], where in the Cooper pair transistor it facilitates the injection of photons in a Josephson laser [16].

In spite of greatly expanding the spectrum of uses, applying a DC bias to the resonator without significantly degrading its quality factor Q is no straightforward task [17–21]. The reason being that while gaining DC access to the cavity, it also forms an potential path for the signal of the cavity to escape by. One of the first ones that successfully made it possible to introduce a DC bias to the superconducting microwave resonator with no significant drop in its Q were Chen et al. [17]. In order to leave the cavity mode undisturbed, they made use of symmetry points to apply the bias. If the bias line is perfectly placed at one of the voltage nodes, it will lead to zero leakage of the resonator on resonance due to its voltage being zero there. While this seems attractive, improper boundary conditions, asymmetry in the design or anything else that effects the voltage node will lead to the resonator decaying in greater or lesser extent into the DC line. To achieve DC access without relying on those symmetry points our group came up with a different way to integrate the bias circuitry [18]. Replacing the dedicated bias lines by shunting one of the two ends of the resonator by a capacitor.

As this solved the issues concerning the sensitivity of the symmetry points, our group focus was completely on the latter design. But it comes at a price. In order to fabricate the device, a more extensive and in particular a more complicated process is needed. This raises the question if the price is worth the pain. And that is what we will try to answer. In this thesis we go back to the original design to honestly evaluate such a resonator by applying a bias to its center.

To evaluate a superconducting microwave resonator with DC access through a symmetry point at the center of the cavity, which is actually summarized in one sentence in the the title of the thesis, we will design, fabricate, simulate and measure the device. To elaborate on that, in the Theory chapter 2 the design is schematically shown and discussed. Further necessary theoretical background is found there too, most importantly how the Q is obtained and extracted from the fit-functions we use for almost all of the results (Theory subsection 2.5.1). For the physical implementation of the design Fabrication Process & Techniques chapter 3 will take you through the required steps to make the resonator on a 1x1 cm chip by means of e-beam lithography. In Experimental Methods chapter 4 the dilution fridge 4 K measurements of the fabricated device is explained as well as how the various types of QUCS and Sonnet simulations are set-up. The Results chapter 5 shows QUCS simulations on the initial design and influences of symmetry of its ports, Sonnet simulations on microwave equivalent lumped elements of the design, and the outcome of the cryogenic measurements of the physical device. Ending it all of with the Conclusion 6, where the results are reflected and a prospect for its future is given.

2

Theory and Background

In this thesis we consider a superconducting microwave resonator with the ability to apply a DC bias current or voltage to its center, a symmetry point. This idea is certainly not new, and therefore it seems appropriate to go back to where it al begun. Giving a solid background on what was once state-of-the-art by showing the working principles of a microwave resonator and how a symmetry point allows for the application of a DC bias. But not only that, in addition it is useful to understand what makes the idea of our group, with the use of a shunt capacitor, different. From the background we dive into the theory of *RLC*-circuits, which seem to be not so different in operation than microwave resonators. When we go one step deeper, we arrive at transmission line theory. Bridging the gap from basic circuit theory to the more realistic picture of waves. As we stepped away from lumped elements with uniquely defined currents and voltages, we also need to change to the more appropriate microwave network analysis. This all puts us in the position to fully understand the used figure of merit, the quality factor Q, and the used described fits to determine its value in practice. To end it all of, we will show how the waves speed is affected in a typically composed resonator's medium.

2.1. DC biased superconducting CPW microwave resonators

There exists a wide range of superconducting microwave resonators. . One way is to make use of a coplanar waveguide (CPW) a type of transmission line (TL) (see section 2.3). What makes a CPW different to an ordinary TL, is that the conductors are planar with one central conductor and two grounded outer conductors. In this section, we discuss three different superconducting CPW microwave resonators with the ability to inject a DC bias. These resonators have a large variety of applications, including current detection by means of a changing cavity resonance used for cameras [22], coupling to superconducting qubits [7] or to quantum dots [23], as persistent current traps for ultra-cold atoms [24], and many more [13–16].

We begin the section with the resonator that was one of the first ones to report such a DC biased superconducting microwave resonator, the Dual-Port resonator (DP). This resonator makes use of symmetry points to allow for a DC bias. It matches the two bias lines to the mode of the cavity to form perfect microwave mirrors. However, if the mode is not perfectly matched the resonator is in greater or lesser extent free to decay into the DC lines. A couple of years later our group came up with a different way of introducing a DC signal to the cavity. They got rid off the dedicated bias lines in the Side-Port resonator (SP) by introducing the DC signal on one of the two sides of the resonator by means of a shunted capacitor. As this tackled the problems occurring in the DP our group focus was completely on the SP. But it comes at a price. In order to fabricate the device, a more extensive and in particular a more complicated process is needed. This raises the question if the price is worth the pain. That is what the Center-Port resonator (CP), used in the Thesis, will try to answer. It makes use of the same working principle as the DP by applying the bias to the center of the cavity. And with the CP we will conclude the section.

2.1.1. Dual-Port resonator

In 2011 Chen et al. [17] were among the first to publish a superconducting microwave cavity capable of applying a DC voltage or current to the cavity. We will refer to their resonator as the Dual-Port, the DP, because of the two bias lines. An illustration of the DP is shown at the top of Figure 2.1 and at the bottom the physical realization is shown.

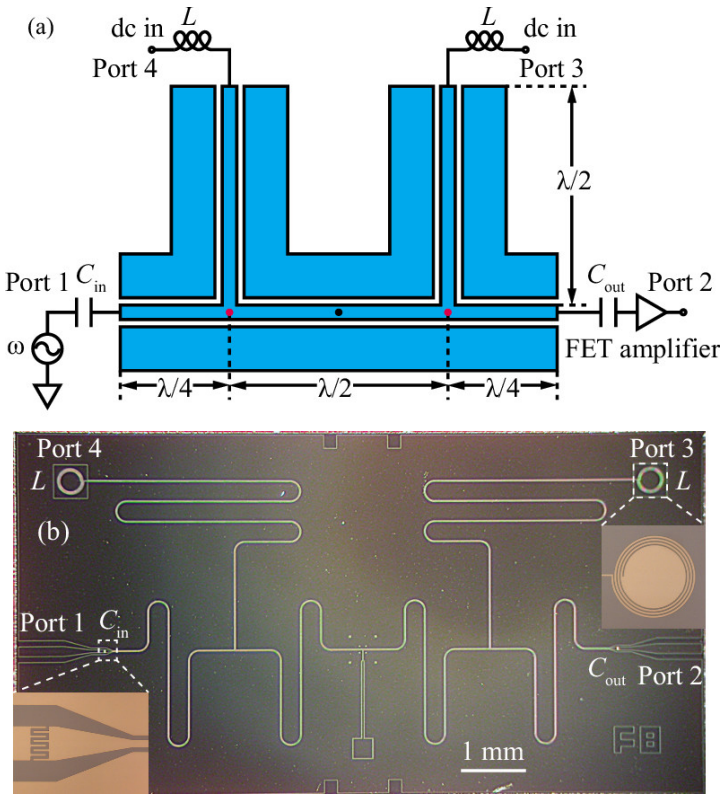

Figure 2.1: (a) Schematic illustration of the DP for the case where a full wave fits the cavity ($l = \lambda$). At port 1 the cavity is fed and at port 2 it is being measured. Both port 1 and 2 are coupled by gap capacitors forming high impedance points (voltage antinodes, current nodes). And again a high impedance point occurs a half wavelength further at the center of the cavity, indicated by a black dot. In between those high impedance points, low impedance points (voltage nodes, current antinodes) exist (red dots). These are the points where the DC lines are connected to in order to allow for the application of a DC bias without disturbing the cavity resonance. (b) An optical microscope image of the niobium DP on a silicon substrate is shown. Here the 8-finger gap capacitor is displayed in the inset on the left and on the right inset the spiral inductor of 3 turns is shown. (Figure from Chen et al. [17])

From the figure you can see that the DP is made out of three branches. The main branch, running from port 1 to port 2, is the resonator. A transmission line of one full wavelength $l = \lambda$ at resonance. The other two branches form the two (dual) DC bias lines, allowing for the application of a DC bias to the main line.

The signal enters the main line $l = \lambda$ from port 1, the feedline. In order to feed the resonator, an AC sinusoidal source is capacitively connected by C_{in}. Where the capacitor acts as a frequency dependent microwave mirror, allowing more or less of the signal to pass through. On the other side of the cavity the signal is measured with $C_{\text{out}} = C_{\text{in}}$, having the same frequency dependent transparency. Operating very similar to the Fabry-Pérot interferometer where instead of capacitors optical mirrors are used. Like the Fabry-Pérot interferometer most of the signal is transmitted from one side to the other at resonance. In fact, if there is no loss in between the mirrors or in the case of the DP there is no loss both on the cavity and out of the DC lines, then all of the signal is transmitted and none is reflected. What happens at resonance is that the propagating waves interfere constructively on the cavity, forming standing waves. And this is what allows for the transmission of the waves from port 1 to port 2. On the other hand, off-resonant is where most, or all, of the signal is reflected back. Here the waves interfere destructively. Therefore around resonance a peak in the transmission parameter (here S_{21}) will be observed, or a dip in the reflection parameter (here S_{11}).

To understand how the standing waves that will form on the resonator look like, we take a look at either end of main line. At both ends the resonator is terminated by gap capacitors. As these capacitors are close to being an open circuit they form current nodes ($I = 0$) and voltage antinodes (V max). This puts a restriction on the waves that are allowed to exist on the line. Only multiples of half a wavelength ($\lambda/2$).

However, only certain modes will allow for the application of a DC bias. This has to do with the impedance match of the DC port to those particular modes. Based on the relation between the impedances, more or less of the wave is reflected. For the reflection, Γ, viewed from the mode to the port, it holds:

$$\Gamma = \frac{Z_{\text{mode}} - Z_{\text{port}}}{Z_{\text{mode}} + Z_{\text{port}}} \tag{2.1}$$

where Z_{mode} and Z_{port} are the mode and port impedance, respectively. What makes the full wave mode (2nd mode) so special is that for this mode the voltage nodes (current antinodes) are at the exact same location as the DC ports. Therefore at $\lambda/4$ and $3\lambda/4$ the mode impedance equals zero ($Z_{\text{mode}} = 0$). A $\lambda/2$ further (along the DC lines) the impedances are again zero at the points where high impedance inductors ($Z_{\text{port}} = j\omega L$) are connected. This causes an impedance mismatch. And according to equation 2.1, it leads to perfect reflection ($|\Gamma| = 1$). Resulting in lossless bias lines.

It is even true that as long as the port impedances at the DC bias lines are anything other than zero, full reflection is obtained. Assuming that the mode impedance at those points are really zero. In reality however, this assumption will almost never hold. As was mentioned at the beginning, the capacitors termination is close to being an open. Close to, but certainly not equal to. This discrepancy, along with the losses that in practice occur on the cavity, are of great importance as it causes the mode impedances at the discussed points to be unequal zero. In that case it does matter a great deal how large the port impedances are. If it is high enough than full or close to full reflection is still obtained. And that is why the DC bias lines are connected to an inductor. Creating a high impedance point in the microwave regime $j\omega L$, while allowing low frequencies (DC) to pass.

To conclude this section, we will look how well the DP works based on the working principles discussed above. To determine its performance, Chen et al. measured the magnitude of the transmission parameter from port 1 to 2, $|S_{21}|$. The data (in dB) was fitted by Lorentzians with its centers around the resonance frequency. From the fits the total quality factors $Q_A = 3750$ and $Q_B = 2500$ were determined. Differences between the two resonators, A and B, come from the different capacitors that are used. For resonator A a smaller 4-finger capacitor of around 4.4 fF and for resonator B a 8 finger of around 11.1 fF was used.

2.1.2. Side-Port resonator

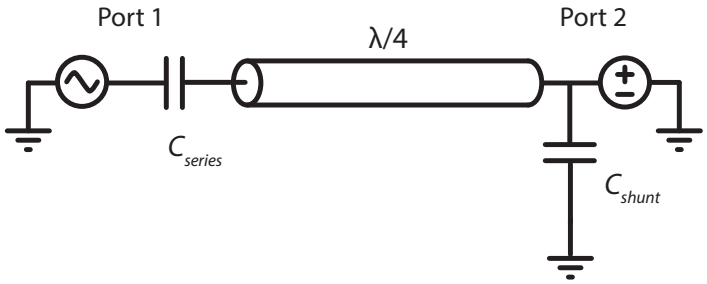

Figure 2.2: Schematic of Bosman et al. [18] SP where, instead of dedicated lines at symmetry points, a shunt capacitor is used to allow for a DC bias (port 2). This capacitor serves as a high reflective point for microwaves while the cavity is still galvanically accessible. For microwaves this high reflective point is close to being a short and therefore forms a voltage node (current antinode) for the allowed standing waves. On the other end of the cavity, at port 1, there is like the DP a gap capacitor, which forms a voltage antinode (current node). Furthermore, it is at this point where the main line is being fed by an AC sinusoidal source. The boundaries formed by both types of capacitors at either end of the cavity determine the standing waves that will form. Therefore, the first mode is a quarter wave and that is why the cavity is labelled by $\lambda/4$.

Our group came up with a different way to allow for a DC bias to be applied to the microwave resonator. Instead of making use of the symmetry points that are used for the DP they make use of a shunted capacitor at one end of the cavity. This was reported by Bosman et al. [18]. A schematic illustration of their design is shown in Figure 2.2. Again, the name we base on the way the DC port is connected. Now it is on the side, so therefore we will call it the Side-Port resonator (SP).

By looking at the figure the first thing to notice is that there are no dedicated DC lines like there are for the DP. Only a main TL resonator of a quarter wavelength $l = \lambda/4$ at resonance, instead of a full wavelength. Feeding of the line is, however, no different then for the DP and the signal is fed to the main line via the gap coupled port, port 1. What is different, is that on the other side the resonator is terminated by a capacitor to ground. Despite this difference, the operation of the resonator is essentially the same. Where at resonance most or all (lossless) of the signal is transmitted due to the formation of standing waves on the cavity.

Although the operation is really similar, the standing waves that will form on the SP are dissimilar. This has to do with the different way port 2 is connected to the resonator. Port 2 is connected with a shunt capacitor

to ground creating a voltage node and current antinode. Together with the gap capacitor on the other side, which forms a voltage antinode (current node), they make up the boundary conditions of the standing waves. Where only odd multiples of $\lambda/4$ are allowed. Therefore the largest wavelength that exists, the first mode, fits just a quarter of its full wavelength, and this is labelled in the illustration in Figure 2.2.

For the SP no mode is 'special' and every mode allows for a DC bias to be applied. This has to do that with the fact that port 2 is galvanically coupled with a shunted capacitor. Making it easy to apply a DC signal. On the other hand, for high frequencies the shunt capacitor is like a short to ground causing most of the signal of the resonator to be reflected. Thereby minimizing the leakage through port 2. Mind the use of the word leakage, as no signal will be lost as there are no extra DC ports. Therefore, every signal that leaks out will attribute to the signal to be measured.

This all seems very promising for the SP, which it is, but there is a downside. The fabrication of the device is more extensive and especially more complicated because of the shunted capacitor, shown in the microscope image of Figure 2.3. Instead of just one e-beam step, it needs three. For every step different material needs to be deposited, coated, exposed, developed and etched. As the fabrication process consists of so many steps it is more prone to error. Besides that it is much more extensive it is also more difficult. It needs precise alignment to correctly stack the three layers on top of each other. In the inset (e) of the figure these layers are shown.

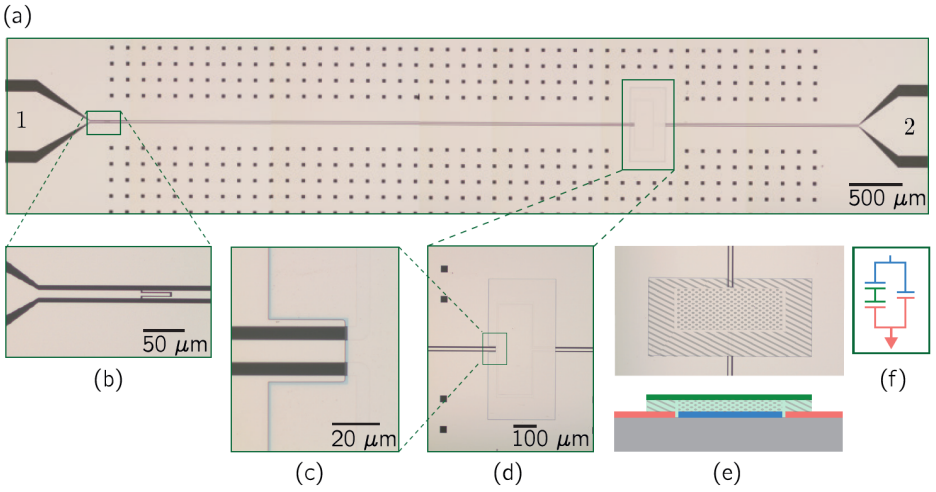

Figure 2.3: Optical microscope image of the SP. (a) the realization of the schematic shown in Figure 2.2. The sapphire substrate is shown in black and in beige Molybdenum-Rhenium alloy is shown. (b) Zoomed in image of the coupling of port 1 to the main line by a 3-finger gap capacitor. (d) Zoom in on the shunt capacitor. (c) Zoomed in further on the left boundary of the shunt capacitor showing in blue the Si_3N_4 dielectric layer. (e) Schematic top-view and cross section of the shunt capacitor respectively from top to bottom. Here the blue color is used to indicate the central conductor, in red the ground plane is shown and green is used for the top plate of the shunt capacitor. (f) lumped-element equivalent model of the shunt capacitor. (Figure from Bosman et al. [18])

Like the DP we end this section with the loaded Q in order to compare the performance of the SP. Bosman et al. determined the Q by means of the response function of the system. This function was obtained from network analysis of the system parameters. They reported loaded quality factors in the range of Q $\sim 10^3$. By performing reflection measurements at both ports they also obtained an internal loss rate $\kappa_{\text{int}} \sim 2\pi \times 230$ kHz at a resonance frequency of $\omega_0 = 2\pi \times 5.3889$ GHz and thus according to equation 2.35 $Q_{\text{int}} = 2.3 \times 10^4$.

2.1.3. Center-Port resonator

The CP is a TL resonator with the possibility to inject a DC bias at its center (port 2) as shown in Figure 2.4. Where we make use of the same working principle as the original DP design. Its name, Center-Port, we derived from the Center Tap [25] that is used for transformers to indicate the connection halfway along the windings. Based on that similar connection, where for the CP it is made in the middle of the TL, the name was chosen.

For this type of resonators the focus in the group has been on the SP, as described in the previous section. They were the first ones to publish such a device, which does not need dedicated DC lines for the application of a DC bias. And therefore no signal is lost via those lines. However, the downside of the SP is due to its relatively complicated fabrication. It needs three e-beam steps with precise alignment in order to perfectly

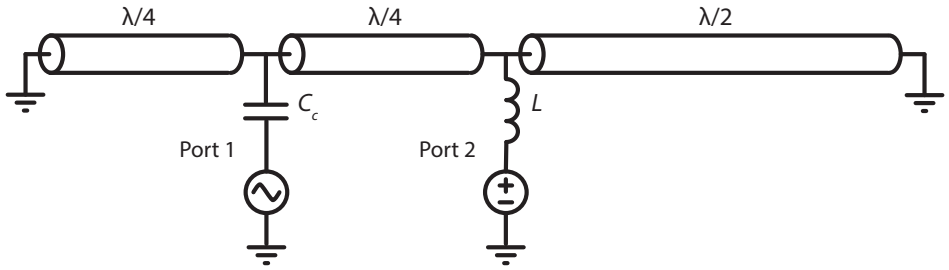

Figure 2.4: Schematic of the CP of length λ. Via port 1, the feedline, at a quarter of the length of the cavity the AC signal is applied. When the applied signal is at resonance, standing waves will form on the cavity. These waves will have voltage nodes (current antinodes) at either end of the main line because of the termination to ground. And for a full wave, in the middle of the cavity there is again a voltage node. This allows for the application of a DC bias without disturbing the resonance. And that is why the DC port, port 2, is connected here.

stack the multiple layers. Mainly due to this reason we wanted to explore a device like the DP, the CP, which only needs one e-beam step to complete. Besides its potential easier and faster fabrication, it is also a good way to check how well this different design will work compared to what was originally used.

In Figure 2.4 there are again three branches like there are for the CP. Only now one of the branches is not a DC line but the feedline, port 1. Where the main line does not run between two ports but ends on both sides to ground. With a full wavelength ($l = \lambda$) at resonance. The DC signal enters the cavity half way at $\lambda/2$.

As was just mentioned the feedline is port 1 and here the signal goes into the resonator. And again most of the signal is transmitted at resonance by the standing waves that will form. But if the resonator is lossless then all of the signal will be reflected back and none is thus transmitted. This has to do with the fact that the port that feeds the cavity is also the port that measures. Nonetheless, even if the magnitude of the signal is unchanged the phase (or real and imaginary part) of the reflection parameter is not. So you are still able to measure the performance of the resonator in that case.

To understand the shape of the standing waves that form at resonance will looks like we need to take the discontinuities at either end of the main line into account. These discontinuities are the terminations to ground and therefore the voltage will equal zero there. Therefore the standing waves will have voltages nodes (current antinodes) at both ends of the cavity. This means that they will be multiples of $\lambda/2$.

However, as was the case with the DP only certain modes allow for the application of a DC bias. Only if the voltage node of the mode matches the location of the DC port, then a DC bias can enter while leaving the cavity undisturbed. Just repeating the argument for the DP. Once more, this holds for the 2nd mode. Where a full wave fits the cavity. And for the same reason as the DP an inductor (high impedance) is coupled to the DC line to make sure that even if the point is unequal zero still most of the signal is reflected. Only now, the inductor is directly coupled to the line instead of the $\lambda/2$ segment of TL in between. Although this is in principle just the same. So the DC line of the CP are really similar to the ones of the DP and are potentially lossless for particular modes like the 2nd mode ($l = \lambda$).

To conclude this section we show the realization of the illustration of Figure 2.4 in Figure 2.5. Where the insets of the figure display the two-finger gap capacitor on the left and the meandering inductor on the right. In the upcoming chapters we will show how the device shown in the figure, the CP, is fabricated (chapter 3), show how it is measured (chapter 4) and present and discuss the final results of the CP (chapter 5).

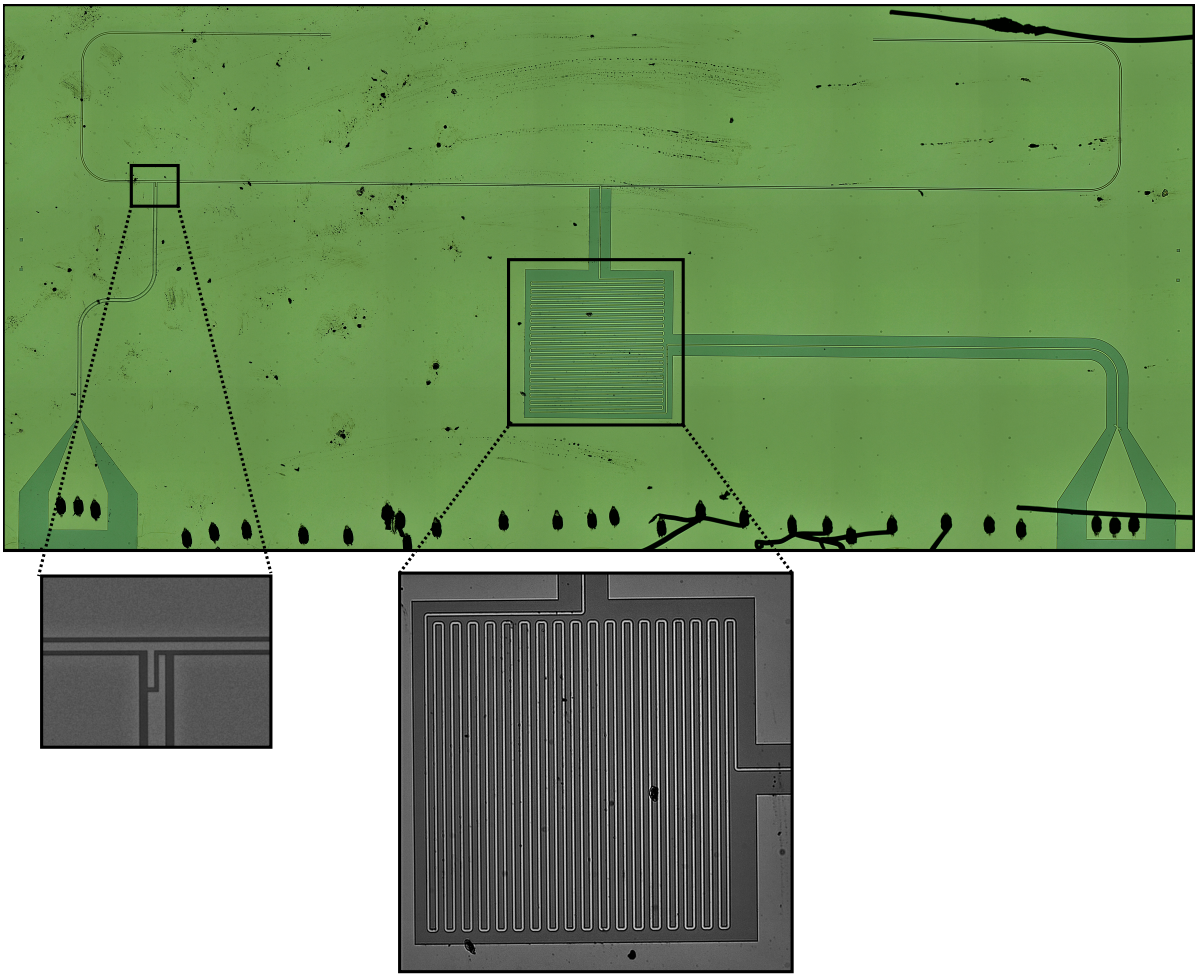

Figure 2.5: Automatic stitching optical microscope image of one of the two CP devices of a 1x1 cm chip. A schematic of this image is shown in Figure 2.4. At the bottom of the chip two launchers run to the two ports. On the left the AC-port and on the right the DC port, both connected to the cavity. Note, the black dots and lines at the boundary of the chip are scars from the removal of wire-bonds. The smaller black dots which occur almost everywhere on the chip are dirt that was collected over a period of several months after fabrication and measurement. In contrast, the magnified image on the bottom left is taken just after fabrication (and just prior to measurement) and does not show any dirt. It shows the capacitor that couples the AC-source to the cavity. The other enlarged image is just a zoomed in version of the main image, showing the meandering inductor coupled at the center of the cavity.

2.2. Parallel resonant *RLC*-circuit

Microwave resonators behave really similar near resonance to lumped-element resonators. In most cases they can be modelled by either a series or a parallel *RLC*-circuit. Here we will review the parallel circuit as it operates similar to the CP. This is because the CP can be approximated near resonance by a TL capacitively coupled parallel *RLC*-circuit, which in turn is equivalent to a parallel *RLC*-circuit as shown in Figure 2.8c. Although we only review the parallel case, the results for the series *RLC*-circuit can be easily obtained by applying the appropriate dualities.

A *RLC*-circuit oscillations occur in the form of energy that is transferred back and forth between the inductor's magnetic and the capacitor's electric field. The behaviour of a parallel *RLC*-circuit is described by the following second order linear differential equation:

$$LC\frac{\mathrm{d}^2 i_L(t)}{\mathrm{d}t^2} + \frac{L}{R}\frac{\mathrm{d}i_L(t)}{\mathrm{d}t} + i_L(t) = i_\mathrm{s}(t) \tag{2.2}$$

where $i_L(t)$ and $i_\mathrm{s}(t)$ are respectively the current of the inductor and that of the source. This result is obtained by applying Kirchhoff's current law and taking into account that for a parallel circuit the voltages over the elements are equal.

Simple harmonic oscillator When the system is neither damped nor driven equation 2.2 changes to:

$$LC\frac{\mathrm{d}^2 i_L(t)}{\mathrm{d}t^2} + i_L(t) = 0 \tag{2.3}$$

where different to equation 2.2 the second term corresponding to the resistor R on the left hand side is left out and $i_\mathrm{s} = 0$. Following along the lines of Boyce et al.[26] the solution to this simple harmonic oscillator, which is actually just an undriven LC-circuit, is given by:

$$i_L(t) = A\cos(\omega_0 t - \delta) \tag{2.4}$$

where A is the constant amplitude and δ the phase, oscillating with angular frequency

$$\omega_0 = \frac{1}{\sqrt{LC}} \tag{2.5}$$

ω_0 is often referred to as the natural frequency.

Damped harmonic oscillator If we now allow for damping the differential equation becomes:

$$LC\frac{\mathrm{d}^2 i_L(t)}{\mathrm{d}t^2} + \frac{L}{R}\frac{\mathrm{d}i_L(t)}{\mathrm{d}t} + i_L(t) = 0 \tag{2.6}$$

Solving for this differential equation results in [26]:

$$i_L(t) = Ae^{-\zeta t/\omega_0}\cos(\omega_\mathrm{d} t - \delta) \tag{2.7}$$

with

$$\omega_\mathrm{d} = \omega_0\sqrt{1-\zeta^2} \tag{2.8}$$

and

$$\zeta = \frac{1}{2R}\sqrt{\frac{L}{C}} \tag{2.9}$$

where ω_d is the damped oscillating frequency and ζ is the damping ratio. Only for the case that $\zeta < 1$ oscillations occur. This is the underdamped case with the amplitude gradually decreasing to zero as the energy of the system is lost in the resistor. For the case where $\zeta > 1$ the system's amplitude will go to zero without undergoing any oscillations.

Sinusoidal driven harmonic oscillator The last situation we will review is the case where the system is both damped and driven. This the same case as we showed at the beginning and its behaviour is described by equation 2.2. The only difference here is that the system is sinusoidal driven, $i_\mathrm{s} = I_0\cos(\omega t)$. This type of source is relevant when an AC source is used, which is also the case for the CP. In steady-state the solution to equation 2.2 is:

$$i_L(t) = B\cos(\omega_\mathrm{d} t - \delta) \tag{2.10}$$

with

$$B = \frac{I_0}{\sqrt{(\omega_0^2-\omega^2)^2 + 4\zeta^2\omega_0^2\omega^2}} \tag{2.11}$$

where ω is the driving frequency. The driving frequency for which the amplitude of i_s (B) achieves it maximum value is given by [26]:

$$\omega_\mathrm{r} = \omega_0\sqrt{1-2\zeta^2} \tag{2.12}$$

with ω_r the resonance frequency. Although, as we can see ω_r is typically not equal to ω_0, we will refer to the resonance frequency as ω_0 throughout the thesis. Note that although they look similar ω_r and ω_d are different. The oscillation corresponding to ω_d is determined by the initial conditions and die out due to damping, while

the oscillation corresponding to the driving source will persist. And thus its frequency is fully described by the systems response to the driving source. Furthermore what is important to take into account is that only for $\zeta < 1/2\sqrt{2}$ the current of the system i_L has a maximum amplitude. For $\zeta > 1/2\sqrt{2}$ the amplitude equals zero. This is true for any resonator with $Q > 1/2\sqrt{2}$ obtained from equation 2.37.

2.3. Transmission-line resonator

At the heart of superconducting microwave resonatorsis the transmission line (TL), of which the CPW is one, as shown in Figure 2.6a consisting of two wires. Acting as a resonator for electromagnetic waves where voltage and current vary over the length of the wires due to its length being several wavelengths in size. In this section we will follow an approach in line with the book by Pozar [27] and discuss the parts that are deemed necessary to understand how standing waves are formed on a TL resonator.

In Figure 2.6a a piece of TL is represented by two conducting wires of length Δz and its lumped-element equivalent circuit is shown just below that in Figure 2.6b. Here resistance, inductance, capacitance and conductance are represented by R, L, C and G. Where the parallel capacitor, C, is used to take into account the capacitive coupling between the two conductive lines. To take care of the self-inductance and the inductance imposed from the opposite parallel wire a series inductor L is used. Losses of the line are represented by R and G, respectively loss of the conductor and dielectric.

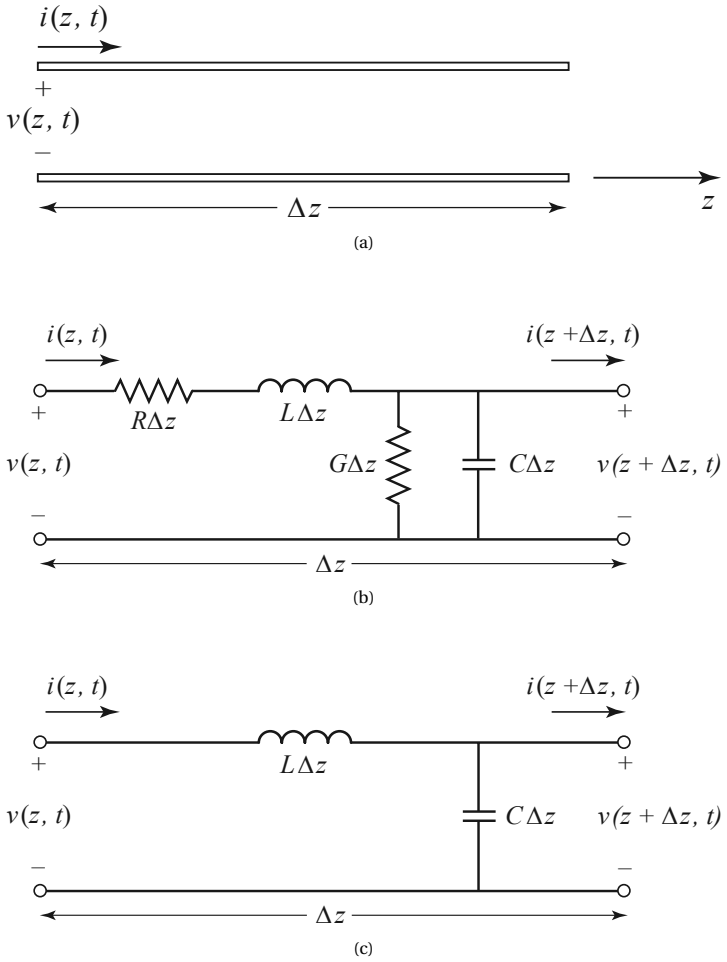

Figure 2.6: Illustration of a TL segment Δz. (a) TL as represented by two conducting wires and (b) the lumped-element equivalent circuit. (c) is a modification of (b) where R and G equal zero, no loss. (Figure from Pozar [27] and (c) a modified version)

Now that the right equivalent circuit is obtained we are ready to derive the spatial and time dependent voltage and current. We start off by making use of Kirchhoff's voltage and current laws. The voltage law states that the voltages in a closed loop add up to zero. For the current law the currents that flow into a node is equal to what is flowing out of that node, and thus the currents at the node adds up to zero as well. First going

around the loop, the voltage equation reads:

$$v(z,t) - R\Delta z i(z,t) - L\Delta z \frac{\partial i(z,t)}{\partial t} - v(z+\Delta z,t) = 0 \tag{2.13}$$

And for the currents:

$$i(z,t) - G\Delta z v(z+\Delta z,t) C\Delta z \frac{\partial v(z+\Delta z,t)}{\partial t} - i(z+\Delta z,t) = 0 \tag{2.14}$$

Taking $\Delta z \to 0$, we arrive at the differential equations:

$$\frac{\partial v(z,t)}{\partial z} = -Ri(z,t) - L\frac{\partial i(z,t)}{\partial t)} \tag{2.15a}$$

$$\frac{\partial i(z,t)}{\partial z} = -Gv(z,t) - C\frac{\partial v(z,t)}{\partial t} \tag{2.15b}$$

These two equations are known as the telegrapher equations.

The telegrapher equations can be simplified by assuming that they are sinusoidal, time-harmonic. This assumption can be made because using a sinusoidal source will result at every point in the circuit again in a sinusoidal behaviour, if the circuit is linear and time-invariant. And indeed a transmission line is linear and time-invariant. Therefore the voltage can be written in the form:

$$v(z,t) = v(z)\cos(\omega t + \varphi(z)) \tag{2.16}$$

Which can be rewritten as:

$$v(z,t) = Re\left\{v(z)e^{j(\omega t+\varphi(z))}\right\} = Re\left\{V(z)e^{j\omega t}\right\} \tag{2.17}$$

The same goes for the current.

As we arrived at the form of equation 2.17 where the only unknown part is $V(z)$, and thus it comes down to solving for $V(z)$. Note that $v(z,t)$ can always be recovered by the last equality of equation 2.17. Taking the time-derivative of equation 2.17 and its current counter part, results in:

$$\frac{\partial v(z,t)}{\partial t} = Re\left\{j\omega V(z)e^{j\omega t}\right\} \tag{2.18a}$$

$$\frac{\partial i(z,t)}{\partial t} = Re\left\{j\omega I(z)e^{j\omega t}\right\} \tag{2.18b}$$

Putting the equations above in the telegrapher equation 2.15a and 2.15b, we get:

$$\frac{dV(z)}{dz} = -(R + j\omega L)I(z) \approx -j\omega L I(z) \tag{2.19a}$$

$$\frac{dI(z)}{dz} = -(G + j\omega C)V(z) \approx -j\omega C V(z) \tag{2.19b}$$

The approximations taken in the last step of equations 2.19a and 2.19b are valid for the high frequency limit where $R \ll j\omega L$ and $G \ll j\omega C$. For our case, where the conducting wires will operate in the superconducting regime, R will equal zero and is therefore not even an approximation. Here the losses are thus taken out and these equations then describe a lossless TL. Solving for $V(z)$ and $I(z)$ will give the following wave equations:

$$\frac{d^2V(z)}{dz^2} = \gamma^2 V(z) \tag{2.20a}$$

$$\frac{d^2I(z)}{dz^2} = \gamma^2 I(z) \tag{2.20b}$$

with

$$\gamma = \omega\sqrt{LC} \tag{2.21}$$

Then, the general solutions for a lossless TL is a wave travelling in the positive and negative z-direction:

$$V(z) = V_0^+ e^{-j\gamma z} + V_0^- e^{+j\gamma z} \tag{2.22a}$$
$$I(z) = I_0^+ e^{-j\gamma z} + I_0^- e^{+j\gamma z} \tag{2.22b}$$

where the wavelength is given by:

$$\lambda = \frac{2\pi}{\gamma} = \frac{2\pi}{\omega\sqrt{LC}} \tag{2.23}$$

Now that we have established the solution for the lossless TL we can apply this to the cavity line we use as a resonator with appropriate boundary conditions (BCs). These BCs for the voltage are:

$$\text{for } z = 0 = l: \quad V = 0 \tag{2.24}$$

With l the length of the line. Why these BCs hold is because the cavity line is terminated on both ends to ground, and thus $V = 0$. Applying the first boundary condition (BC) for $z = 0$ to the general solution of the lossless transmission line equation 2.22a leads to:

$$V(z = 0) = V_0^+ + V_0^- = 0 \tag{2.25}$$

Which implies that $V_0^+ = -V_0^-$. Next we apply the second BC for $z = l$ to the same equation, resulting in:

$$V(z = l) = V_0^+ e^{-j\gamma l} + V_0^- e^{+j\gamma l} = 0 \tag{2.26a}$$
$$\rightarrow V_0^+ e^{-j\gamma l} = V_0^+ e^{+j\gamma l} \tag{2.26b}$$
$$\rightarrow e^{-j\gamma l} = e^{+j\gamma l} \tag{2.26c}$$

Where in the second step we a made use of the result of the first BC, $V_0^+ = -V_0^-$. By making use of Euler's formula we can rewrite the last equation as:

$$\cos(\gamma l) - j\sin(\gamma l) = \cos(\gamma l) + j\sin(\gamma l) \tag{2.27}$$
$$-\sin(\gamma l) = \sin(\gamma l) \tag{2.28}$$

Which only holds if γl is a multiple of π:

$$\gamma l = \frac{2\pi l}{\lambda} = n\pi \qquad \text{with } n \in \mathbb{Z} \tag{2.29}$$

In any real case n can only take on positive value, other solutions will physically be impossible. This leads to the possible allowed waves to exist on the cavity line:

$$l = \frac{1}{2}\lambda n \qquad \text{with } n \in \mathbb{N}^+ \tag{2.30}$$

So multiples of half a wavelength are allowed.

2.4. Microwave circuit parameters

At low frequencies the system can be described by its lumped element model, where its electrical components are considered to be ideal and concentrated to a single point. This assumption is only valid when frequencies are low enough. Low in the sense that the operating wavelength is much larger than the physical length of the circuit. However, for microwave circuits this assumption does not hold, having a much larger frequency with a wavelength that fits the system size several times. Therefore the voltage and current in the circuit are not well defined at every point, which makes it difficult to measure voltages and currents directly. This means that we need another way to describe the systems behaviour. And that is where the scattering parameter (S-parameter) comes into play.

2.4.1. S-parameter

The scattering (S) parameter makes use of the relation between incident and reflected waves instead of relating the total voltages and currents. And these ratios of waves can be measured directly with a vector network analyser (VNA) or calculated by means of network analysis techniques. When more than one port is used, the scattering parameter becomes a scattering matrix. The scattering matrix considers the network to be a black box and fully describes the network from its ports.

Following along the lines of Pozar [27] with V_n^- the amplitude of the voltage wave incident on port n and V_n^+ the amplitude of the voltage wave reflected from port n for an N-port network. The scattering matrix for an N-port network is then given by:

$$\begin{bmatrix} V_1^- \\ V_2^- \\ \vdots \\ V_N^- \end{bmatrix} = \begin{bmatrix} S_{11} & S_{12} & \dots & S_{1N} \\ S_{21} & S_{22} & \dots & S_{2N} \\ \vdots & \vdots & \ddots & \vdots \\ S_{N1} & S_{N2} & \dots & S_{NN} \end{bmatrix} \begin{bmatrix} V_1^+ \\ V_2^+ \\ \vdots \\ V_n^+ \end{bmatrix}$$

When considering a single element of the matrix, one uses:

$$S_{ij} = \left. \frac{V_i^-}{V_j^+} \right|_{V_k^+ = 0 \text{ for } k \neq j} \tag{2.31}$$

What this means is that S_{ij} is given by driving only port j, no other port, and measuring at port i.

For a N-port network that is free of any losses, it holds that:

$$|S_{11}|^2 + |S_{22}|^2 + ... + |S_{NN}| = 1 \tag{2.32}$$

This is just a form of the law of conservation of energy, here in terms of power ratios. Stating that the signal should go somewhere. Because it is given in power ratios the magnitudes of the reflection parameters at the ports are squared as the S-parameter is in voltage and not in power ratios.

2.4.2. Y- and Z-parameters

Admittance (Y) and impedance (Z) parameters do relate the total voltages and currents at the ports. But, at the beginning of the section it was stated that the voltages and currents are not well defined for microwave signals. So it seems strange to list those parameters here as it is very difficult to measure them. However, for advanced simulations the electric and magnetic field are known at all points in space by solving Maxwell's equations and therefore are able to return the Y- and Z- parameters. Also, those parameters are related to the the S-parameters and can be inferred from them. The main reason to make use of Y- and Z- parameters is that it is easy to extract values of equivalent lumped elements, e.g. capacitance and inductance in an intuitive way.

The parameter Z_{ij}, driving port j with current I_j and leaving all other ports open (i.e. $I_k = 0$ for $k \neq j$), while measuring the voltage at port i, is given by:

$$Z_{ij} = \left. \frac{V_i}{I_j} \right|_{I_k = 0 \text{ for } k \neq j} \tag{2.33}$$

In a similar fashion the parameter Y_{ij} can be found by driving port j with the voltage V_j and shorting all other ports (i.e. $V_k = 0$ for $k \neq j$) while measuring the current at port i:

$$Y_{ij} = \left. \frac{I_i}{V_j} \right|_{V_k = 0 \text{ for } k \neq j} \tag{2.34}$$

2.5. Q-factor

In general to quantify the performance of a resonator the dimensionless Q-factor is used. We will define the quality factor in terms of the linewidth κ and the resonance frequency ω_0 as follows:

$$Q = \frac{\omega_0}{\kappa} \tag{2.35}$$

where κ corresponds to the full-width at half the maximum power (FWHM) as can be seen from Figure 2.7. The smaller κ gets, the larger the Q becomes. So for a high Q the graph in the figure gets narrower and the resonator is better at discriminating signals of different frequencies.

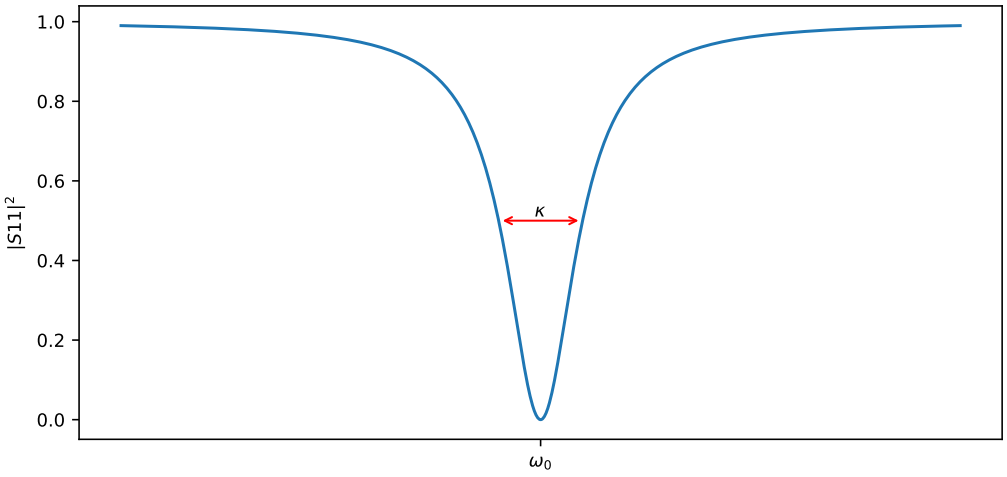

Figure 2.7: An example of a reflection (S_{11}) measurement around resonance (ω_0) for critical coupling which shows the linewidth κ at $|S_{11}|^2 = 0.5$. From κ and ω_0 the total/loaded Q can be determined by equation 2.35

Q can also be defined as the fraction of the energy stored W to the energy dissipated per cycle P_{loss}/ω at ω_0:

$$Q = \omega_0 \frac{W}{P_{\text{loss}}} \tag{2.36}$$

Both definitions of Q agree increasingly well for higher Q and are very precisely related for high Q. However, there exists no functional relation between the Q defined in terms of energy and the one defined by the bandwidth as is shown by Čapek et al.[28]. Even for high Q both definitions are not always in good agreement. This is the case when there is dephasing, which will leave the energy loss unaffected but will 'smear out' the resonance peak making κ larger than it actually is. Dephasing occurs because during the time you measure the resonance of the system changes making the resulting resonance peak appear wider.

There is yet another way of defining Q and that is by its damping ratio ζ as follows:

$$Q = \frac{1}{2\zeta} \tag{2.37}$$

where this definition is directly related to the one given by the energy in equation 2.36. To see how these equations are related we take the decay factor of the damped harmonic oscillator as discussed in section 2.2 $e^{-\zeta t/\omega_0}$ and rewrite equation 2.36 to:

$$Q = \omega_0 \frac{U}{-\mathrm{d}U/\mathrm{d}t} \tag{2.38}$$

Solving this first order differential equation leads to:

$$U(t) = Ce^{-\omega_0 t/Q} \qquad \text{with } C \text{ a constant} \tag{2.39}$$

By comparing this to $e^{-\zeta t/\omega_0}$, and by noting that the energy scales with the square of the amplitude, we indeed obtain equation 2.37.

The Q's defined above are actually not only characterizing the resonator itself but will inevitably contain the coupled external circuitry. Therefore these Q's are considered to be the total- or loaded-Q's. To distinguish between contributions from the resonator and the external circuitry the Q is respectively separated in the unloaded- or internal-Q (Q_{int}) and the external-Q (Q_{ext}) as follows:

$$\frac{1}{Q} = \frac{1}{Q_{\text{int}}} + \frac{1}{Q_{\text{ext}}} \tag{2.40}$$

In order to quantify the level of coupling between the resonator and its external circuitry the coupling coefficient η is used, defined as:

$$\eta = \frac{Q}{Q_{\text{ext}}} = \frac{Q_{\text{int}}}{Q_{\text{int}} + Q_{\text{ext}}} \tag{2.41}$$

where η ranges from 0 to 1. It relates the total amount of power lost to the power lost in the internal circuit. If $\eta < \frac{1}{2}$ ($Q_{\text{int}} < Q_{\text{ext}}$) then more power is dissipated in the external circuit than in the resonator and the system is said to be undercoupled. For the case $\eta = \frac{1}{2}$ ($Q_{\text{int}} = Q_{\text{ext}}$) critical coupling is achieved and the same amount of power is dissipated internally as it is dissipated externally. In that case the feedline and the resonator are matched and maximum power transfer from the feedline to the resonator is achieved ($|S_{11}|^2 = 0$). When $\eta > \frac{1}{2}$ ($Q_{\text{int}} > Q_{\text{ext}}$) then the system is overcoupled and the loss in the resonator is greater. To sum it up, the three different coupling cases:

$$\eta < \frac{1}{2} (Q_{\text{int}} < Q_{\text{ext}}) : \text{undercoupled} \tag{2.42a}$$

$$\eta = \frac{1}{2} (Q_{\text{int}} = Q_{\text{ext}}) : \text{critically coupled} \tag{2.42b}$$

$$\eta > \frac{1}{2} (Q_{\text{int}} > Q_{\text{ext}}) : \text{overcoupled} \tag{2.42c}$$

2.5.1. Reflection parameter of a TL capacitively coupled parallel RLC resonator

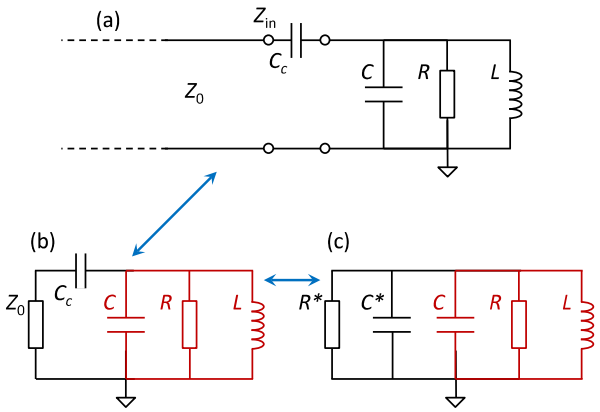

Figure 2.8: (a) Schematic of the CP approximated at resonance by a TL with a real-valued Z_0 capacitively coupled to a parallel RLC circuit. Here the RLC circuit replaces the TL cavity of the CP. (b) Its equivalent circuit where the lumped element Z_0 replaces the TL. In (c) the coupling capacitor (C_c) and Z_0 are transformed into their parallel equivalents C^* and R^*. Note that in (b) and (c) the black part is considered to be the external circuit, whereas the internal circuit is indicated in red. (Figure from Daniel's document [29])

The CP can be seen as a TL capacitively coupled to a RLC resonator at resonance as shown in Figure 2.8. In (c) of the figure its equivalent parallel RLC-circuit is shown. From this circuit and by using the results of Daniel's document [29] we get close to resonance ($\omega \sim \omega_0$) for the interal quality factor (Q_{int}) and the external quality factor (Q_{ext}) with the assumption $\omega^2 C_c^2 Z_0^2$:

$$Q_{\text{int}} \approx \omega_0 R(C + C_c) \tag{2.43a}$$

$$Q_{\text{ext}} \approx \omega_0 R^* (C + C_c) \qquad \text{with } R^* \approx \frac{1}{\omega^2 C_c^2 Z_0^2} \tag{2.43b}$$

for which the reflection parameter, S_{11}, around resonance is given by [29]:

$$S_{11} = 1 - \frac{\eta\kappa}{\kappa/2 + j\Delta\omega} \tag{2.44}$$

where $\Delta\omega = \omega - \omega_0$, the difference between the probing frequency ω and cavity resonance frequency ω_0. The coupling efficiency η relates κ to the external decay rate $\kappa_{ext} = \eta\kappa$. Besides the part that is attributed to the external circuitry, κ_{ext}, there is the other part coming from the internal, κ_{int}. Together they add up to κ, $\kappa = \kappa_{int} + \kappa_{ext}$. From κ and ω_0 you are able to calculate Q as was shown in the beginning by equation 2.35. When η is known as well you can get Q_{int} and Q_{ext} as follows:

$$Q_{int} = \frac{\omega_0}{\kappa_{int}} = \frac{\omega_0}{\kappa(1-\eta)} \tag{2.45}$$

$$Q_{ext} = \frac{\omega_0}{\kappa_{ext}} = \frac{\omega_0}{\kappa\eta} \tag{2.46}$$

In the case above if the driving frequency is far away from resonance the $|S_{11}|$ will reach its maximum value and equals unity as all of the signal is being reflected. However, if between the input and the cavity attenuation occurs its maximum will no longer equal unity but a fraction, say A (the overall attenuation), of it. In our case this will be due to the lines that are coupled to the ports and the directional coupler. Additionally to A it could be that you have chosen the wrong reference phase. This could be because the measuring device like the vector network analyser (VNA) or the software you use chooses a different phase. To account for a constant ϕ_0 and a linear in frequency t_0 reference phase including an attenuation A, the reflection parameter will have the following form:

$$S_{11} = Ae^{j(t_0\omega+\phi_0)}\left[1 - \frac{\eta\kappa}{\kappa/2 + j\Delta\omega}\right] \tag{2.47}$$

Note that A, though related, is not the attenuation factor α.

2.5.2. Interpretation of κ_{int} as obtained from the reflection parameter of a port

The κ_{int} you will obtain from using the reflection parameter described in the previous section will not only contain contributions of the internal circuitry (i.e. the resonator). Unless of course you have only one port, than the κ_{int} will really be only from the internal. For more than one port, it will contain additional coupling from the ports (other than the port from which the reflection parameter is taken).

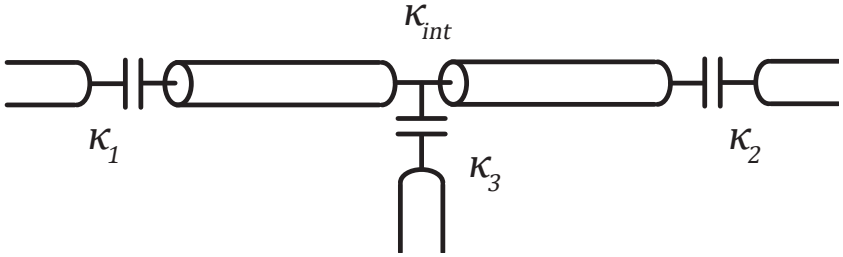

Figure 2.9

Lets have a look at Figure 2.9 to see what the κ_{int} is for a resonator consisting of three ports. For clarity we use only three ports, but the same procedure can be applied for any number of ports. We will we look at the κ's we obtain for the reflection of port 1, S_{11}. Although the same argument will hold by choosing port 2 or 3.

So, how do κ_{int} and κ_{ext} of S_{11} look like. For $\kappa_{ext(S_{11})}$ it is easy, as the external circuitry viewed from S_{11} is just everything coupled to the outside from port 1, indicated by the figure as κ_1. However, for $\kappa_{int(S_{11})}$ it is not only the internal circuitry κ_{int} but also the decay rates from port 2 and 3, κ_2 and κ_3 respectively. And thus the following holds:

$$\kappa_{ext(S_{11})} = \kappa_1 \tag{2.48a}$$

$$\kappa_{int(S_{11})} = \kappa_{int} + \kappa_2 + \kappa_3 \tag{2.48b}$$

From these equations it than follows that the total linewidth from S_{11}, $\kappa_{(S_{11})}$, is given by:

$$\kappa_{(S_{11})} = \kappa_{\text{ext}(S_{11})} + \kappa_{\text{int}(S_{11})} \tag{2.49a}$$
$$= \kappa_{\text{int}} + \kappa_1 + \kappa_2 + \kappa_3 \tag{2.49b}$$
$$= \kappa \tag{2.49c}$$

Thus the total linewidth is not specific for port 1. And because the same argument holds for port 2 and 3, it is not specific to those ports either. Or in general, for any port. This means that κ is always the same no matter from which port you look at it.

2.6. Effective dielectric constant

In vacuum electromagnetic (EM) waves travel at the speed of light c which Maxwell related to the electric constant ϵ_0 and the magnetic constant μ_0 as follows:

$$c = \frac{1}{\sqrt{\epsilon_0 \mu_0}} \tag{2.50}$$

This famous formula only holds for waves propagating through vacuum. If a wave travels to a different medium the phase velocity becomes:

$$v_{\text{ph}} = \frac{1}{\sqrt{\epsilon_{\text{r}} \epsilon_0 \mu_{\text{r}} \mu_0}} \tag{2.51}$$

where only the relative terms ϵ_{r} and μ_{r} the relative permittivity (or dielectric constant) and the relative permeability can change for different media.

For a CPW (see Figure 2.10a) the EM waves do not travel through one medium but to a combination of two, the dielectric beneath and the air above. In case of a CPW μ_{r} in equation 2.51 is set to 1 as the used media are not magnetic in nearly all cases. Furthermore, the medium is thus not a single one anymore but a combination of different media and therefore different ϵ_{r}'s, and that is why ϵ_{r} is replaced by the effective dielectric constant (ϵ_{eff}). This changes equation 2.51 to:

$$v_{\text{ph}} = \frac{1}{\sqrt{\epsilon_{\text{eff}} \epsilon_0 \mu_0}} = \frac{c}{\sqrt{\epsilon_{\text{eff}}}} \tag{2.52}$$

In order to find the effective dielectric constant (ϵ_{eff}) we first take a look at the distribution of electric and magnetic fields for a CPW in Figure 2.10b. By considering the metal thickness to be infinitesimal it looks from the figure like half of the fields are contained in the air and half of it in the dielectric substrate. Based on this, ϵ_{eff} will just be the average of both air (ϵ_{r}=1) and the dielectric ϵ_{r}:

$$\epsilon_{\text{eff}} = \frac{1 + \epsilon_{\text{r}}}{2} \tag{2.53}$$

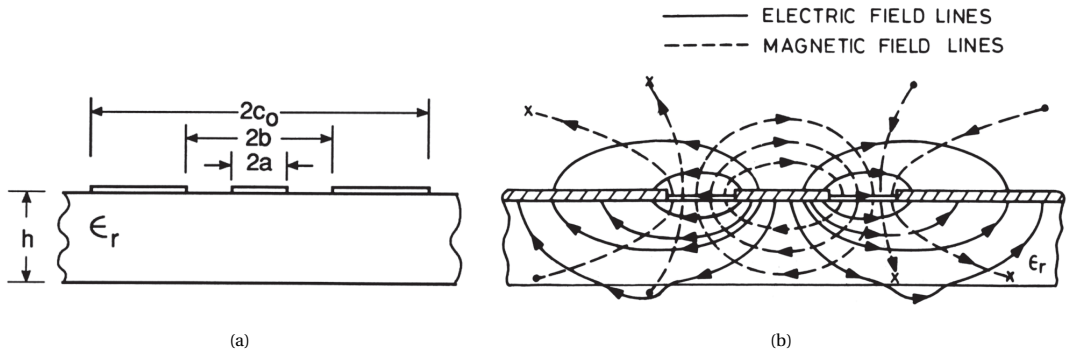

(a) (b)

Figure 2.10: (b) electric and magnetic field lines for pure TEM waves (the quasi-static approximation)(figures from Garg et al. [30])

Only this view is not completely correct, as, although the air above is certainly large enough to be considered infinite, for the substrate this is not clear. Additionally, it is also not apparent that the ground planes can be treated to extent to infinity. Therefore, we take the substrate thickness to be h and the extent of the outer sides of the ground plane to be $2c_0$ [31] as shown in Figure 2.10a. Then from from Garg et al. [30] we get for ϵ_{eff}:

$$\epsilon_{\text{eff}} = 1 + \frac{\epsilon_{\text{r}} - 1}{2} \frac{F(f_2)}{F(f_1)} \tag{2.54}$$

with

$$f_1 = \frac{a}{b} \sqrt{\frac{c_0^2 - b^2}{c_0^2 - a^2}} \tag{2.55a}$$

$$f_2 = \frac{\sinh(\pi a/2h)}{\sinh(\pi b/2h)} \sqrt{\frac{\sinh^2(\pi c_0/2h) - \sinh^2(\pi b/2h)}{\sinh^2(\pi c_0/2h) - \sinh^2(\pi a/2h)}} \tag{2.55b}$$

and where the factor $F(f)$ is given by Hilberg approximation [32] as:

$$F(f) \simeq \frac{\pi}{\ln\left[\left(1+\sqrt{f'}\right)\Big/\left(1-\sqrt{f'}\right)\right]} \qquad \text{for } 0 \le f \le \frac{1}{\sqrt{2}} \tag{2.56a}$$

$$F(f) \simeq \frac{1}{\pi} \ln\left[\left(1+\sqrt{f}\right)\Big/\left(1-\sqrt{f}\right)\right] \qquad \text{for } \frac{1}{\sqrt{2}} \le f \le 1 \tag{2.56b}$$

$$f' = \sqrt{1 - f^2} \tag{2.56c}$$

This approximation is used because it allows for the calculation of ϵ_{eff} directly from the design parameters, while still having a high accurate outcome. Its greatest relative error is smaller than 2.36×10^{-3}. If $c_0, h \to \infty$ then both f_1 and f_2 approach a/b and thus $F(f_2)/F(f_1) \to F(f_1)/F(f_1) = 1$ and ϵ_{eff} of equation 2.54 becomes just the average of dielectric and the air as we derived before in equation 2.53.

The calculations done above for ϵ_{eff} are based on the quasi-static approximation considering pure transverse electromagnetic (TEM) are used. Where the approximation is valid for up to 40 GHz according to Garg et al.[30] and backed by [33] where they studied the dispersion relation of ϵ_{eff}. But even if ϵ_{eff} is not constant and equal to equation 2.54 then at least $\epsilon_{\text{eff}} < \epsilon_{\text{r}}$, and approaches ϵ_{r} only in the infinite frequency limit.

3

Fabrication Process & Techniques

In this chapter we will walk you through the steps we have taken in order to fabricate the Center-Port (CP) microwave resonator as described in section 2.1.3. In electron-beam (e-beam) lithography electrons are used to write patterns. This technique allows for feature sizes in the 100 nm range for the Raith EBPG5000Plus, which is well below the smallest feature size used in our design of 3 μm. For the fabrication of our devices we used two silicon 1×1 cm chips that were both coated with NbTiN by means of reactive sputtering done in the pre-fabrication. The size of the chips is sufficient to allow two devices to be produced on a single chip. This means that we should end up with four devices. The reason for this surplus of devices, we only need one, is just as a precaution as many problems can occur during fabrication. Problems such as caused by human errors, like scratching the chip, or by dirty operation environments, like materials that fall off during processing, and many more that may break down the device. Before we can start the fabrication process we make sure that the used chip is clean. Cleaning is done by first spraying the chip with acetone and than with isopropylalcohol (IPA), and finally blow-drying it with N_2. Nitrogen is preferred as opposed to air as it will not cause oxidation of your chip during drying. The following cleaning procedure has been applied:

Pre-fabrication clean
acetone spray 10 s
IPA spray 10 s
N_2 blow-dry

The goal is to end up with the pattern of the device(s) composed of NbTiN on top of a silicon substrate. In the following sections we will walk through all the fabrication steps necessary to achieve this goal. We start off by applying the resist in section 3.1 in order to pattern the chip by means of the ebeam, section 3.2. Afterwards, the exposed resist will be removed by the developer, section 3.3. In between we will show how the resist can be removed in section 3.4. This stripping of the resist is also used after the last section 3.5, reactive ion etching (RIE). In the last section the metal that is unprotected by the resist will be etched away. Finally, after stripping away the residual resist, the chip is done.

3.1. Spin coating

To be able to write the desired pattern using the e-beam an electron sensitive resist, ARP6200.18 (18% solids content), will be applied. In order to apply the resist uniformly over the substrate, it is spin coated at high angular speeds between 1000-8000 rpm (see Figure 3.1). Not only the uniformity is determined by the spin-rate the thickness as well, the faster it spins the thinner the film will be. On one hand the centrifugal force is pushing the liquid off the plate and on the other hand it is the shearing which keeps the liquid in place. The shearing is due to the adhesion between the liquid and the substrate and is proportional to the viscosity of the liquid [34]. During the process the fast moving air above the plate will dry the solvent, increasing its viscosity. This is what finally prevents any more solvent to be pushed off and the film has reached its final thickness. After the resist is spun it will be baked to make it stick better and evaporate residual solvent. The spin coating recipe used here is:

Spin-coating	
Resist	ARP6200.18 (CSAR 62.18)
Spin resist	60 s: 10s at 500 rpm and 50 s at 4000 rpm
Bake resist	3 min at 155°C

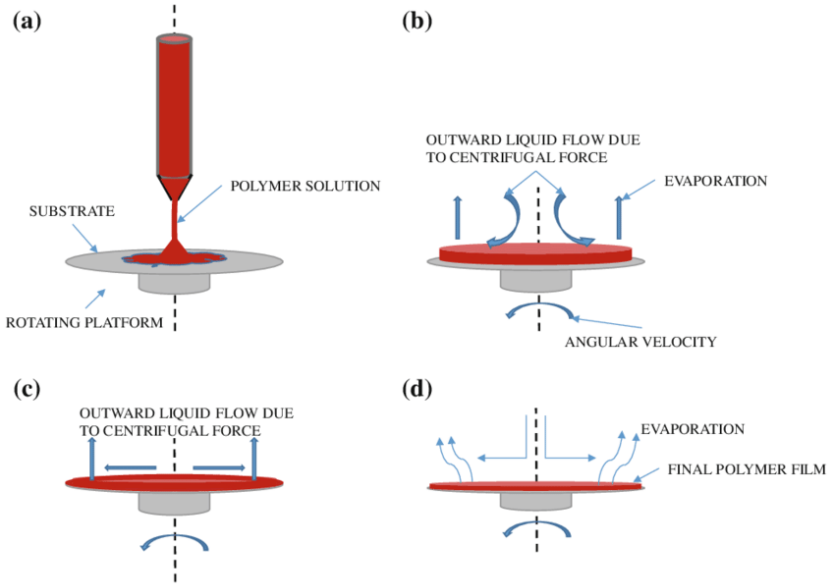

Figure 3.1: An illustration of the spin coating process. The chip is placed on top of the rotating platform and vacuumed tight. Then (a) the resist is deposited on top of the chip. Now, (b) the platform is starting to spin, first at a low rate (500 rpm for 10 s) after which (c) it will increase to a much higher rate (4000 rpm for 60 s). Finally (d) the film will evaporate most and reach its final thickness. During (b) and (c) and even (a) the resist is evaporating as well. (Figure from Das et al.[34])

3.2. E-beam

Now the chip is ready to be exposed by the e-beam, in our case the Raith EBPG5000Plus. On the location of the exposure the resist will either weaken or strengthen based on the type of resist that is used. The first type of resist we call positive tone resist, the other one we call negative tone resist (see Figure 3.2). The difference between the two types of resist comes from their reaction upon exposure. Where in positive resist the polymers are cut short making them easier to dissolve, in negative resist the polymers form cross-links making them more resilient to dissolve. Dissolving the resist happens in the next step, development discussed in section 3.3. To what extend the resist will dissolve is one of the main factors that determines how much a certain part of the chip should be exposed, the dose. We will discuss which dose to use for the type of resist we have used during fabrication, positive resist. Of course, for the negative resist the inverse holds. If the dose is too low parts of the pattern are not exposed long enough and resist will remain after development. This occurs mainly on the boundary where the dose is the lowest, shown in Figure 3.3a. Here you can see that the part in the center is exposed long enough where the color is even. However, at the edges the pattern is changing in color showing a varying reflectance with wavelength. The variance in the reflectance is caused by a change in thickness of the resist, as shown in silicon by Henrie et al. [35], with increasing thickness towards the edge. This residual resist will protect the metal underneath during etching, causing a gradual increase in the thickness from the boundary into the pattern. So the edges become less sharp with a reduced pattern size. On the other hand a too high dose causes too much of the surrounding near the edges to be exposed (see Figure 3.3c) Therefore less of the resist will remain where it should be resulting in more metal etched away in the end. Again this makes the edges less sharp, now with an increased pattern size. To get the right dose you should be just at the point where the resist on the pattern is free of resist. In that case the resolution is maximum and the desired pattern is obtained. The 'sweet' spot for our case is obtained in Figure 3.3b.

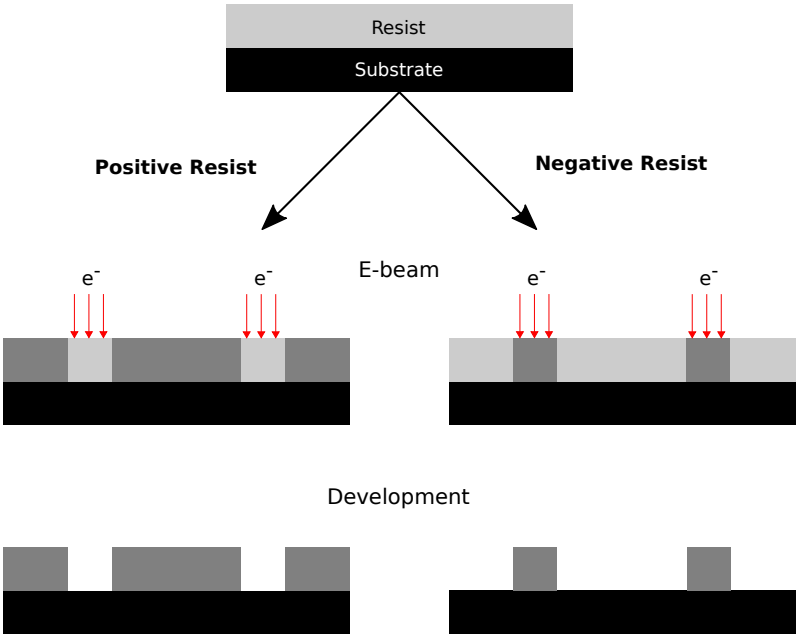

Figure 3.2: An illustration of the difference between positive and negative tone resist after e-beam exposure and development. Where for positive resist the exposed part is removed, for negative resist the unexposed part is removed. Exposure of the positive resist weakens the polymer chains by cutting them to smaller pieces. On the other hand, exposure of the negative resist strengthens the polymers by cross-linking them to form greater chains.

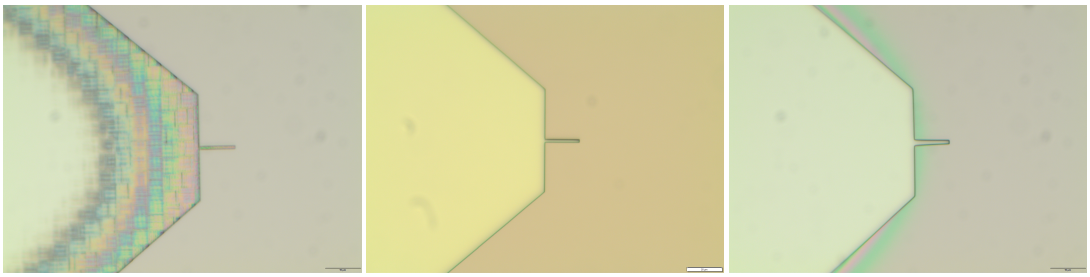

(a) (b) (c)

Figure 3.3: Microscope images of a dose test. In (a) a too low dose is used resulting in residual resist on the pattern. On the other hand in (c) the dose is too high where part of the resist of the surrounding is gone. With (c) showing the right dose with a sharp edge and fine features. Note that the label, indicating the scale, in the lower right corner is correct for (a) and (c) but incorrect for (b). All should be 10 μm which is also the length of the smallest feature pointing towards the right.

3.3. Development

Once the pattern is written by the e-beam, it is ready to be developed. This is done by a putting the chip in a chemical, the developer, which is able to dissolve the exposed part if positive resist is used and dissolves the unexposed part if negative resist is used. ARP-6200 is a positive resist and thus the exposed part will be removed after development, by Phentylacetate. It is not true that the unexposed part is immune to the developer, but it will dissolve at a much slower rate. This means that the time the chip is in the solution is crucial. Too long and you have less resist to protect the desired part during etching. Too short and there is still resist left on the places where you want to etch the material away. To stop the development and rinse off the developer a combination of methyl-iso-butylketon (MIBK) and IPA is used. The recipe we used for the development is:

Developing	
Developer	Phentylacetate 60 s
Rinser	MIBK:IPA 1:1 60 s
Drying	N_2 blow-dry

3.4. Resist stripping

When the result after baking of the resist is unsatisfying you can strip the resist and start all over. In our case this was done after the first development. Upon examining the chip under a light microscope we saw that there was a piece of dirt on the cavity line (see Figure 3.4a) on one of the two devices. This piece of dirt could potentially cause an electrical short and therefore break down the device. Although there was still one device that seemed fine we decided to strip the resist away. Also because the used dose seemed to be on the low side as can be seen in Figure 3.4b. From the figure you can see that the color on the lines ending up in the upper left corner are a bit darker, meaning that it is a bit elevated because not all resist there is gone. We could as well just start over with a new chip, but because of a shortage of NbTiN coated chips at the time we decided to strip the resist. To strip away the resist postive resist stripper 3000 (PRS3000) was used at an elevated temperature. The solution with the chip in it was covered with a silver foil. This was done to prevent too much evaporation of the solution, and maintain a constant temperature inside. The following recipe was used to strip away the resist:

Strip Resist	
Resist stripper	PRS3000 at 75 for 12 h+
Rinser	2× IPA 30 s
Drying	N_2 blow-dry

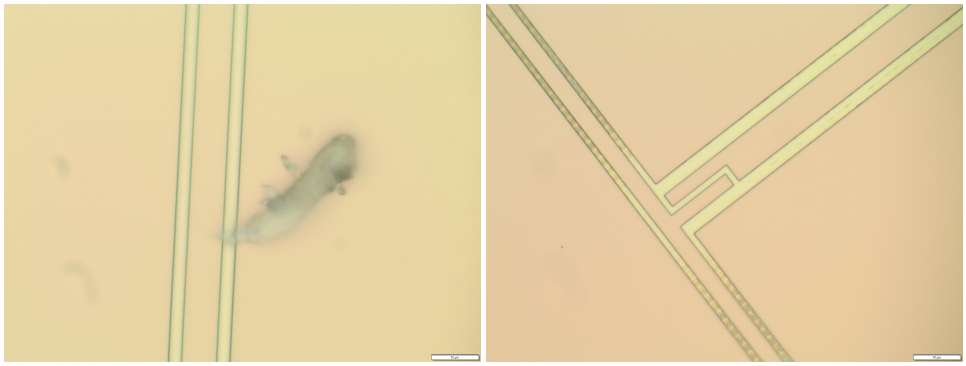

(a) (b)

Figure 3.4: Light microscope image of parts of the chip consisting of the Center-Port design that were unsatisfying and therefore stripped of resist afterwards. (a) Shows a potential electrical short on the resonator cavity line which could connect the central line with the surrounded grounded plane. (b) Shows the capacitor that couples the feedline to the resonator with a too low dose of 250 μC. This can be seen from the difference in color indicating different level of focus. This is because the darker part is a bit higher due to some resist that is still there, while in the yellow looking part it is completely gone.

3.5. Reactive-ion etching (RIE)

The final fabrication step for the chip is etching away the uncovered metal, not protected by resist, to end up with the desired pattern of NbTiN on top of the silicon substrate. This is done by RIE which is a type of dry-etching, as opposed to wet-etching. Where in wet-etching a solution is used as an etchant, in dry etching a plasma, ionized gas, is used.

The chip is placed in the etcher, here the VLL Leybold F3 is used, indicated by 5 in Figure 3.5 on the lower plate (4). On this plate a RF field can be applied by means of a power source. The chamber is then pumped down to high vacuum, 6 μbar. Next, the gases (O_2/SF_6) (2) will enter the system via the upper plate (1) and a RF power source operating at around 50 W creates a sufficiently large oscillating electric field to kick out the electrons and thus ionizing the gas. The electrons that come free during the ionization will accelerate away from or to the lower plate (4) upon each cycle of the field. Only if they strike down on the lower plate (4) will they build up (negative) charge as its the only part of the system that is not directly grounded. This surplus of negative charge will create a electric field between the two plates (3) with a DC voltage of nearly 300 V. The now created electric field will accelerate the positively charged ions (2) to the lower plate (4) with the chip on top of it (5). When the ions hit the plate they will not only knock away the surface but will also react with it.

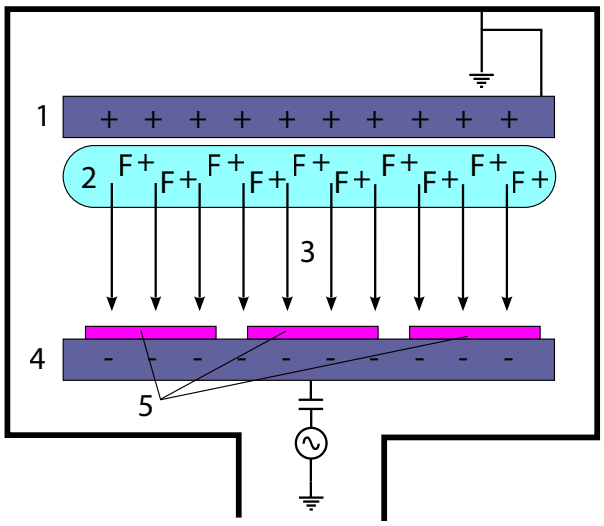

Figure 3.5: Illustration of the process during RIE. The AC power source applied to plate (4) ignites the plasma (2) and causes a negative charge on the plate. This creates an electric field (3) between the plates (1 and 4). Which in turn results in a positive charge on the upper plate (1). The electric field accelerates the ions (2) towards the lower plate where the sample (5) is placed. These ions will not only transfer there kinetic energy, knocking out atoms upon impact, but will also react with the sample. (figure modified from Wikipedia [36])

Resist		Before etch		Plasma			After etch	
Type	Recipe	Expected Allresist (nm)	Profiler (nm)	O2 flow (sccm)	SF6 flow (sccm)	Etch time (s)	AFM Δ(m)	Etch rate (nm/s)
ARP 6200.18	4000 rpm, 4min 155C	800	806	20	0	90	673	1.47
				13.5	5	30	765	1.36

Table 3.1: Etch rates of the used positive-tone resist in the VLL Leybold F3 etcher. Where the resist is applied by means of spin coating and baking on a hot plate. The etch rates are determined based on the etch time and the height measurements before and after. The height before etching was measured by scratching the surface with a tweezers and measuring the depth with the profilometer. After etching the same depth was measured, now with the atomic force microscope (AFM). The expected height is retrieved from Allresist [37].

NbTiN is almost resilient to an oxygen plasma, but it reacts really well with the fluor radicals from SF_2. This makes it possible to remove the uncovered metal. For the etching we used the following recipe including the pre-conditioning and the cleaning afterwards with actual operating parameters:

Pre-conditioning	
Gasses	5 sccm O_2
Pressure	50 μbar
RF power	30 W forward, 0 W reflected
DC bias voltage	~ 290 V
Time	25 min
Etching	
Gasses	5/13.5 sccm O_2/SF_6
Pressure	6 μbar
RF power	50 W forward, < 10 W reflected
DC bias voltage	274 V
Time	4 min 56 s
Cleaning	
Gasses	20 sccm O_2
Pressure	50 μbar
RF power	200 W forward, < 20 W reflected
DC bias voltage	~ 760 V
Time	2 hrs

To know when the metal part that is not protected by resist is indeed gone a laser beam is focussed on that part of the chip. The intensity of the lasers reflection is measured in order to check if a certain layer is etch through as different materials will absorb more or less of the incoming light. Therefore if a change is observed you know you have reached the next layer. After 4 min and 56 s the etching was stopped before such a change was seen, as it took more time than expected (around 4 min 10 s). This was because the laser spot was not located on the bare metal part but on the part that is covered by resist. The good thing was that indeed no change in the intensity occurred at this particular location which means that the part that should be protected had still some resist left. By looking at the etch rates of the resist, see table 3.1, only about 330 nm of resist was expected to be removed (O_2 and O_2/SF_6). So indeed there was still plenty, about 470 nm, of resist left.

To check if the etch time was really too long the chip was stripped of resist (same recipe used as in section 3.4) and placed under a profilometer. The profilometer measured a height difference between the part where the metal should be gone and its surrounding of roughly 300 nm. With an expected NbTiN layer thickness of 100 nm, this means that there was 200 nm over-etch. So at least all the metal was that was originally not covered by resist was etch al the way trough.

Now the chip is done. A picture of the final chip is shown in 3.6. However, this picture was taken after the wirebonds were removed (the big black scars) and months of lying around and collecting dirt (the black dots). After inspection of all four of the devices there was one abnormality observed, shown in 3.7. At the inductor there is a short between one of the meandering lines, this will most likely not destroy the device only lower the inductance. All other devices looked to be fine, so there was no reason to use the one with the expected lower inductance. That is the advantage of having several devices to start with. The chip with the fine looking devices was wire-bonded and mounted and is ready for measurement.

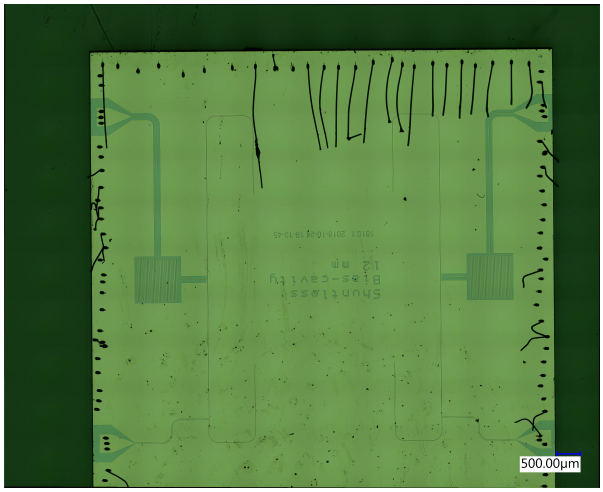

Figure 3.6: Confocal microscope image of the whole final chip, consisting of two Center-Port devices. The picture was taken a couple of months after measurement. The black lines are from the removed wire bonds and the black dots are coming from the dust that has settled in the period after measurement. The chip is 1×1 cm in size. There is also a label and a measure in blue indicating the scale of 500 μm.

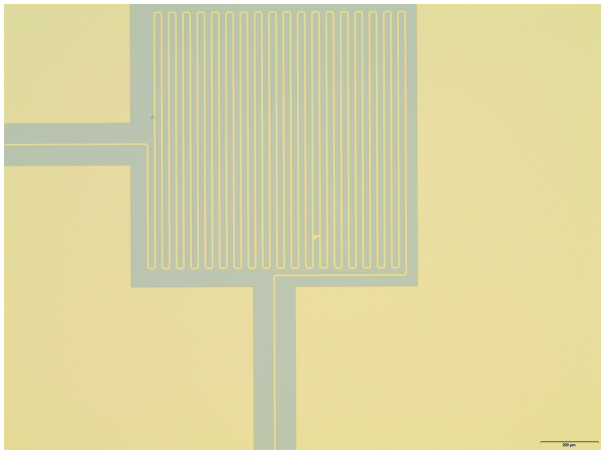

Figure 3.7: Light microscope image of the meandering inductor part of the Center-Port device after the full fabrication process. In this picture a short is visible on one of the inductor lines. This will most likely cause the inductance to be lower than expected but will not affect the operation in any other way. Still this device is therefore not used as there are three other devices that do not show any visible problems.

4

Experimental Methods

We will show and discuss here the DIY4K reflection measurement setup and the several QUCS and Sonnet simulation setups of the Center-Port resonator (CP). For the DIY4K measurement we will, besides showing how to setup the measurement, also show how the measurement is preformed. Furthermore, the QUCS setups consist of the initial design of the CP, and the ones where the bias line position is allowed to vary. Finally, we will demonstrate two elements of the CP, the meander-line inductor and the gap capacitor, in Sonnet.

4.1. Cryogenic microwave reflection measurements for determining Q

In order to check if the device fabricated in accordance with chapter 3 is working, we will measure the device's s-parameters in a dilution fridge. The dilution fridge we use for our measurements is the do-it-yourself 4K (DIY4K), which is a relatively small fridge capable of cooling down to less than 4 K. (Results: During measurement the temperature was 3.47 K.) For our measurements this is well below its critical temperature (T_c) of NbTiN of around 15 K [38]. This ensures that the compound is in its superconducting regime, necessary for the functioning of the device.

After fabrication the chip is not yet ready to be measured and first we need to connect to the chip from the outside. Connecting the chip is done by mounting the chip on a printed circuit board (PCB) and wire bonding the ports (Figure 4.1a). But not only the ports, also multiple wire-bonds are placed on the ground plane of the chip to make sure that any current that may appear on it can easily be transferred from the chip to ground. To be able to more effectively cool down the chip, it is placed in a metal box to increase the thermal conductivity (see Figure 4.1b). This metal box will serve as well as a shield to radiation from outside the box. From the metal box four silver plated cupronickel coaxial cables appear as can be seen in the same picture. These are connected to the two devices both consisting of two ports, the AC and DC port. The cables are not ordinary connected, but are connected via sub-miniature A (SMA) connectors which operate in the tens of GHz with a constant impedance of 50 Ω. Therefore they are perfectly suited for our device, as they will not change properties in the RF working regime.

Now the chip is ready to be placed in the fridge. The metal box is screwed down to the upper plate of the fridge as can be seen from Figure 4.2b. From here two of the four cables are used, the AC port is connected to a directional coupler, the blue piece in Figure 4.2b, and split into two. The directional coupler used here is the PASTERNACK PE2204-20 which attenuates by 20 dB in the frequency range 4-8 GHz. Because of the directional coupler an additional port of the fridge is required. This means that each device takes on three ports of a total of four of the fridge, so only one device can be hooked up at once. The directional coupler is set up in such a way that it is weakly coupled to the incoming signal, call it port 1, and directly coupled to the outgoing signal, port 2. In this way it attenuates the signal going into the chip, while leaving the signal coming out almost unaltered. Therefore the chip will heat up much less and no important information is lost. After everything inside is connected the fridge will first be pumped down for half an hour and then cooled down for about four hours.

To be able to measure the device that is inside the fridge, the fridge is coupled to a PNA N5222A VNA, capable of measuring both amplitude and phase properties. Looking at Figure 4.2a you can see the VNA on the left side, coupled to the fridge via blue cables. The VNA is typical instrument for measuring RF applications,

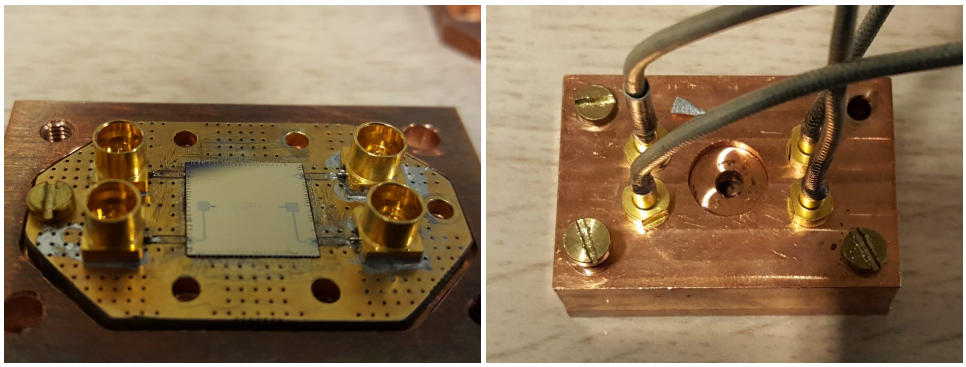

(a) (b)

Figure 4.1: Preperation of the chip before going in the fridge. In (a) the chip is mounted on a PCB and screwed down on the lower part of the metal box. Then in (b) the top part of the box is closed up and coaxial cabels are connected via SMA.

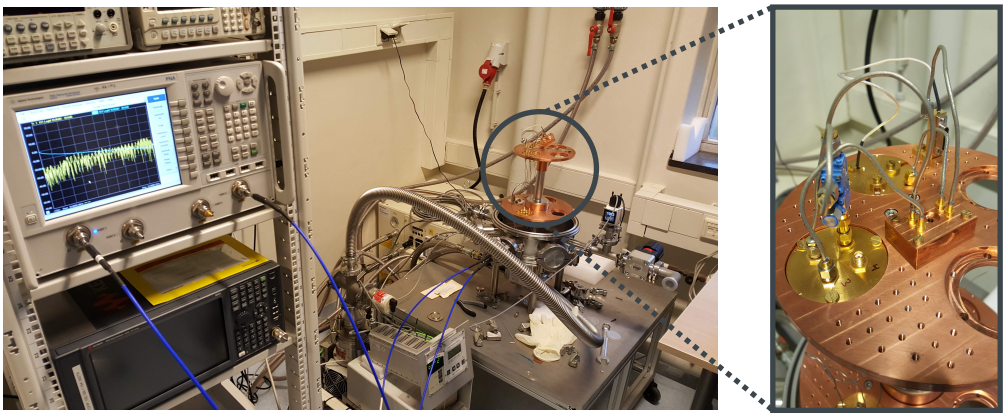

(a) (b)

Figure 4.2: Measurement setup of the DIY4K. In (a) the full setup is shown with the VNA on the left connected with blue cables to the open fridge on the right with the copper part sticking out. (b) Shows a zoomed in picture of the fridge upper part and from this the metal box, containing the chip, and the connections are seen. Here in blue the directional coupler is visible.

such as our cavity. It is used to measure transmission and reflection in the form of s-parameters, described in chapter 2.4.1. A power sweep was preformed to examine these s-parameters. What is meant by a sweep is that the parameter of interest, here power, is changed and measured for the whole frequency range for every value of that parameter. (Results: The current was swept from 0 to 50 mA and back again, and from 0 to 60 mA and back in a total of 101 steps with a power of -20 mdB. The power sweep was done from -30 mdB to 10 mdB with a increment of 1 mdB, one way.) These measurements were performed with all three cables connected, port 1 and 2 from the directional coupler and port 3 coming from the DC port of the cavity. The reflection parameter is given by driving port 1 and measuring the reflected wave coming out of port 2, S_{21}. The transmission parameter can be found by driving the same port 1, but measuring at port 3. Once the measurements are done the system is heated back up to room temperature after again about four hours and pumped back up to atmospheric pressure. From S_{21} we will fit the real part to a Lorentzian from which the Q_{int} will be determined. This quantifies how well the device is working.

4.2. QUCS simulation techniques for parameter sweeps of the Center-Port resonator design

The main part of this thesis is focussed on simulation done in quite universal circuit simulator (QUCS). QUCS is a simulation program that allows for the study of the signal behaviour of your circuit. This can be done by simulation types which are used here such as s-parameter and parameter sweeps. In the following sections we show how the QUCS simulations were set up.

4.2.1. Two-port device setup

Here we address the question of how to simulate the Q_{int} of the 2-port device as shown in Figure 4.3. To do so, we first focus on a sub-question of how to determine the coupling capacitor, Cc, for which the device is critically coupled. For this we perform a s-parameter simulation over a large frequency range, large enough that at least the second mode of the cavity is captured. The reason why we search for the second mode is explained in section 2.1.3. Once the second mode is found, we zoom in. In this way we keep the same number of points but increase the resolution significantly. The zoom is chosen such that there is no relevant information for determining the Q_{int} outside the zoom window. In other words, the full resonance dip is inside the chosen frequency range. A parameter sweep as explained in section 4.1 for multiple values of the Cc is carried out. The capacitance that gives zero for the real part of reflection parameter, S_{11}, is the value that critically couples port 1 to the cavity (see section 2.5). For this value the Real(S_{11}) is fitted by equation 2.44 (subsection 2.5.1) from which the Q_{int} is extracted. This answers the question at the start of the section.

4.2.2. Three-port device setup

In this section we address two main questions. Both of the questions concern the 3-port device for two cases. One where the ports are resistively and one where they are capacitively coupled to the cavity as can be seen from Figure 4.4 and Figure 4.5, respectively.

The first question we want to address is how to simulate the effect of moving port 2 from its center position on the Q_{int}. This is done for the case where port 3 is closed off, so actually this is a 2-port device not a 3-port one. The reason that is it is written here and not in section 4.2.1, is that the same setup, apart from closing off port 3, is used as in the 3-port case. Port 3 is closed off by setting the resistance of the power supply of port 3 ($R3$) to an absurdly high resistance of $10^{18}\Omega$ for the resistive case, Figure 4.4. For the capacitively coupled case (Figure 4.5), the resistor that couples the power supply of port 3 to the cavity (Rc) is set to the same absurdly high value. In order to simulate the effect of moving port 2, a parameter sweep (see section 4.1), *SW1* in Figure 4.4 and Figure 4.5, is preformed. *SW1* sweeps the parameter that offsets port 2 from its center position on the cavity (*offcenter*). The range of the sweep is limited by how far port 2 can be moved from the center. Beyond a certain point the dip in the s-parameter, caused by the resonance, will become too small to distinguish. But not only the value of the *offcenter* is important, also the frequency range of the s-parameter simulation. Here the range is set such that the dip is well between its bounds but small enough to clearly see the dip with the chosen number of simulation points. Similar to the previous section, section 4.2.1, the real part of S_{11} is fitted by equation 2.47 (subsection 2.5.1), but now for every value of *offcenter*. From these fits the Q_{int} for every value of the parameter can be determined.

Secondly, we want to concentrate on how to simulate the effect of including or leaving out port 3 on the Q_{int}. Again we consider the same circuits as we did in the paragraph above. The approach is exactly the same, the only change that we make is that we now set $R3$ to $R1$ and Rc to 0 Ω. In that way we include port 3. By

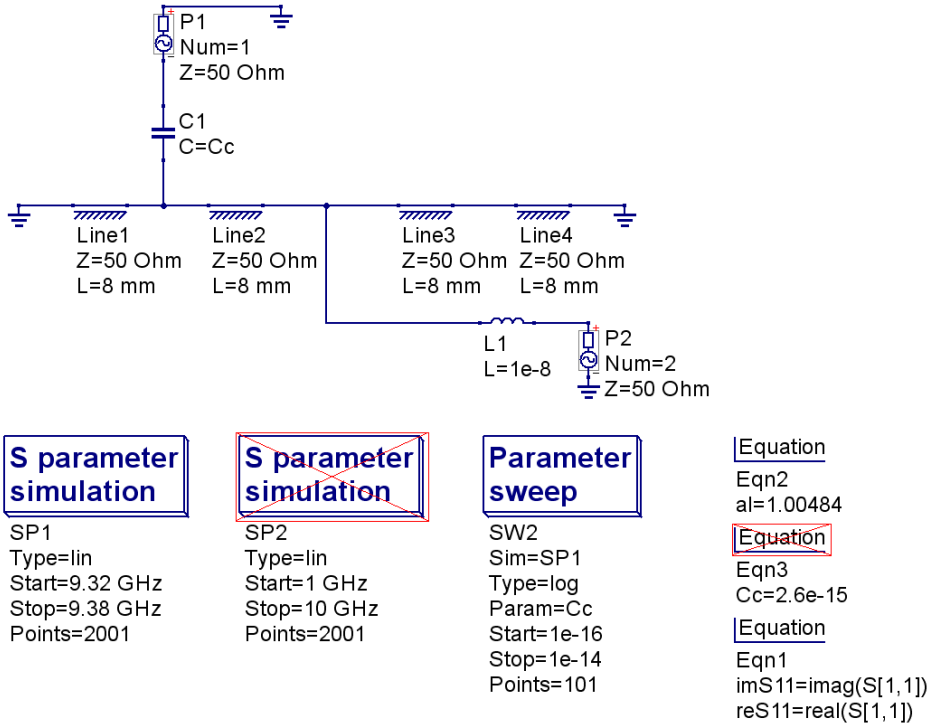

Figure 4.3: QUCS circuit diagram of the Center-Port design. The parameter sweep, $SW2$, of the coupling capacitor, Cc, is used to be able to obtain for which value critically coupling is achieved. From the same simulation the Q-factor is determined.

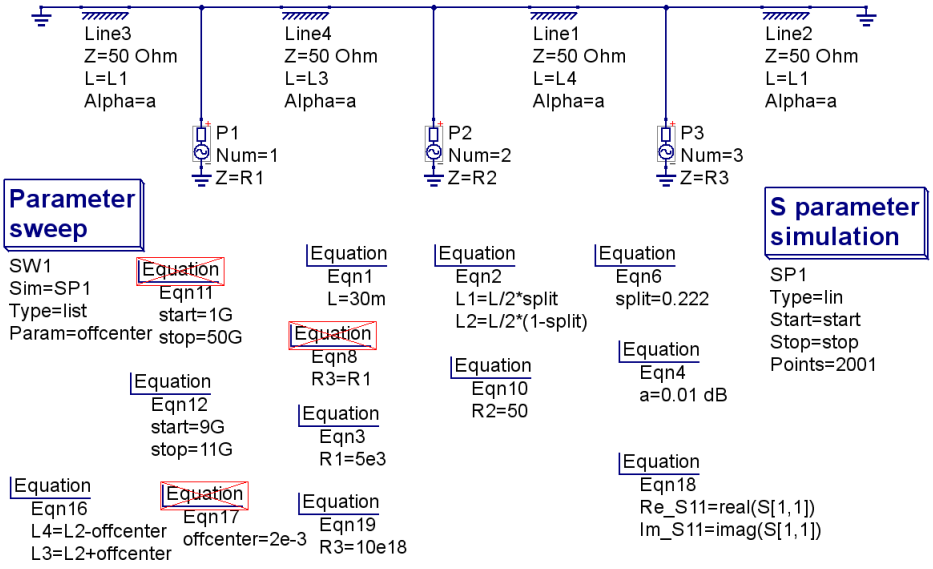

Figure 4.4: QUCS schematic setup of a resistively coupled 3-port cavity to be able to determine its influence of changing the center port, $P2$, position on the Q-factor. This is done by a parameter sweep, $SW1$, where the parameter *offcenter* is changed and simulated by S parameter simulation, $SP1$, for different frequency ranges set by the variables start and *stop*.

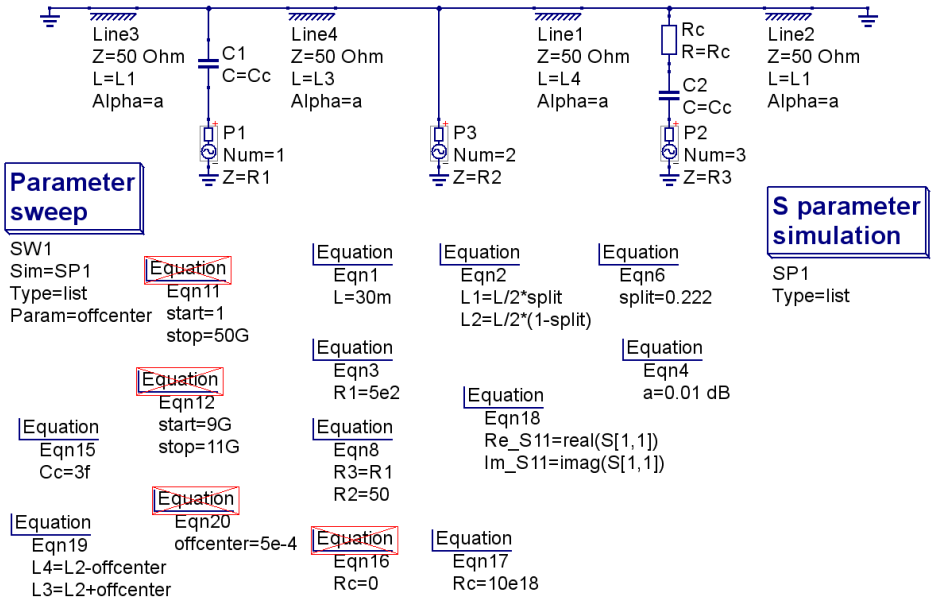

Figure 4.5: QUCS schematic setup of a capacitively coupled 3-port cavity to be able to determine its influence of changing the center port, $P2$, position on the Q-factor. This is done by a parameter sweep, $SW1$, where the parameter *offcenter* is changed and simulated by S parameter simulation, $SP1$, for different frequency ranges set by the variables start and *stop*.

comparing this case, with port 3 open, and the case of the previous paragraph, where port 3 is closed, we simulate the desired effect.

4.3. Sonnet Simulation Setup for Elements of the Fabricated Center-Port Device

In this section we go over to a different type of simulation, named Sonnet. Sonnet allows for the simulation of physical devices were elements are not considered lumped as is the case in QUCS. It provides *'..precise RF models (S-, Y-, Z-parameters or extracted SPICE model) for planar circuits and antennas. The software requires a physical description of your circuit (arbitrary layout and material properties for metal and dielectrics), and employs a rigorous Method-of-Moments EM analysis based on Maxwell's equations that includes all parasitic, cross-coupling, enclosure and package resonance effects.'* [39]. By making use of Sonnet we are able to figure out if the physical elements that we fabricated are in correspondence with the lumped elements designed in QUCS. For this we individually simulate the C_c from the AC-port and the inductor for the DC-port and discuss both separately in the following two sections. To make sure that there is a one-to-one correspondence between the fabricated device and the one we are simulating, we use the same file as the one that was send to the e-beam for fabrication. From this file only the part corresponding to the individual elements are taken in order to solely capture the behaviour of that element.

4.3.1. Meander-line choke inductor of the DC-port

The inductor (L) is the element that connects the DC-port to the cavity line. It is part of the design to function as a barrier for high frequencies preventing the high frequency signal to escape from the resonator while allowing low frequencies to enter. Such a inductor is often called a choke inductor as it effectively chokes, attenuates, high frequencies.

In order to check how the inductor behaves we took the part of the device shown in Figure 4.6. Showing only the meandering line of the device, the inductor, in Sonnet. It is surrounded by a box, the boundary of the figure, inside which the EM simulation is preformed. Because the fabricated chip is grounded, via wire-bonds, the used box is grounded from all sides as well. Two ports are placed at the ends of the meandering line connecting the inductor to the box. Between those ports the relevant parameters will be simulated. In the physical device port 1 is connected to the launcher that links the device to the outside and port 2 is what goes to the cavity line.

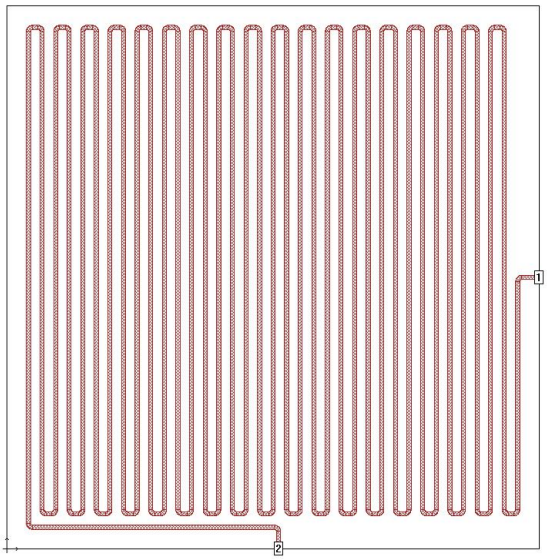

Figure 4.6: Sonnet EM simulation set-up of the inductor of the Center-Port device. The inductor consists of a meandering conductive line that connects the DC-port to the cavity line. A choke inductor which purpose it is to block-off high frequency signals while allowing DC signals to enter the cavity. Ports 1 and 2 are connected to the surrounding grounded box. Between the ports the simulation is preformed to obtain the relevant parameters in order to determine its inductance.

To see how the inductor behaves we preform an adaptive bandwidth sweep (ABS) [40] providing a S-, Y- and Z-parameter data sweep over the desired frequency range. From this we can calculate the Inductance. If the meandering line does indeed behave as expected, and thus behaves like a inductor, the design in Figure 4.6 is like a two-port network with a series inductor, indicated by L. And that is why we choose the following model shown in Figure 4.7a. To take care of any losses a resistor, R is connected in series. If no losses exist R will equal zero. In order to extract the value of L from this model the Y_{11} parameter, see section 2.4.2, is taken which effectively shorts port 2. This leads to the figure right next to it, Figure 4.7b. Where Y_{11} is given by:

$$Y_{11} = \left.\frac{I_1}{V_1}\right|_{V_2=0} = \frac{1}{R+Z_L} \tag{4.1}$$

where $Z_L = j\omega L$ with L the inductance. And thus to extract L from Y_{11} we first take the reciprocal:

$$\frac{1}{Y_{11}} = R + j\omega L \tag{4.2}$$

Now you can see that the reactive part is given by the inductor and by taking the imaginary part of the reciprocal of Y_{11} we get L as follows:

$$L = \frac{\mathrm{Im}\left\{\frac{1}{Y_{11}}\right\}}{\omega} \tag{4.3}$$

Finally, we have established the procedure to extract the inductance from the simulated data. Equation 4.3 thus gives the inductance for an inductor in series with two ports.

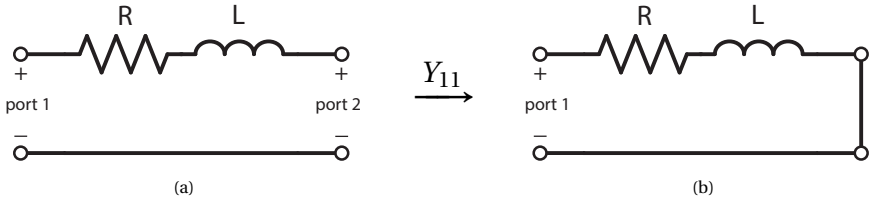

Figure 4.7: Y_{11} transformation on the RL model of the coupling capacitor in order to be able to determine the inductance L. (a) The 2-port series RL equivalent circuit of the inductor of Figure 4.6. Where R is used to account for loss that may appear on the line. Applying the Y_{11} transform which effectively shorts port 2 (b).

4.3.2. Gap coupling capacitor of the AC-port

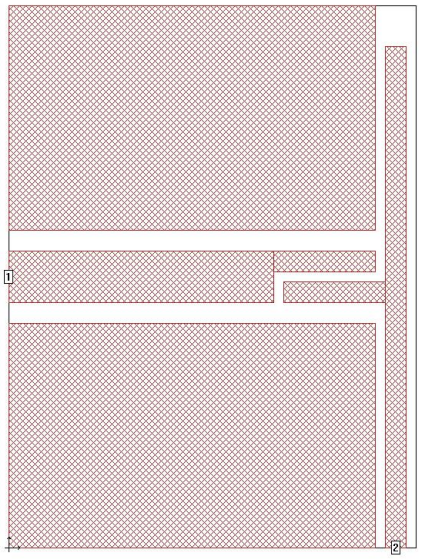

Figure 4.8: Sonnet EM simulation set-up of the capacitor of the Center-Port device. The capacitor consists of a two separate conductive fingers that connects the DC-port to the cavity line. Its purpose is to drive the cavity with maximum power transfer. Ports 1 and 2 are connected to the surrounding grounded box. Between the ports the simulation is preformed to obtain the relevant parameters in order to determine its capacitance.

Moving to the other element the (coupling) capacitor (C_c), that couples the AC line to the cavity. Linking the TL resonator to the external circuitry. Here we show how to simulate in Sonnet, and from those results, calculate the capacitance of C_c.

To simulate the behaviour of only the capacitor the part of the device, as can be seen in Figure 4.8, is taken. It shows two separated conducting fingers constituting the C_c in Sonnet. Again as was the case for the inductor here C_c is grounded from all sided by the box surrounding the design. The two-ports are set up in such a way to solely capture C_c. This is done by connecting port 1 to the feedline and port 2 to the resonator. Furthermore the other end of the resonator, where port 2 is connected to, is terminated before the end of the box. The reason for this is to be able to use two ports instead of three, which would make determining the capacitance a lot more complicated. By terminating in this way the influence of that 'port' is only marginal, as it is weakly coupled to the ground plane. This justifies the use of only two ports.

Between the two ports an ABS is preformed providing Y-(S- and Z-) parameter sweep over the set frequency range. From this result the capacitance can be calculated. For this the capacitor is modelled by its lumped element equivalence where a series capacitor (C) and resistor (R). The resistor is there to take into account any losses that exist in the design. To determine the capacitance the same approach is used as for the inductor, so we will not repeat this here but only show it in Figure 4.9.

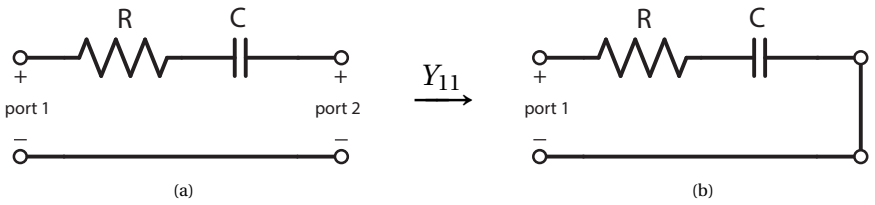

Figure 4.9: Y_{11} transformation on the RC model of the coupling capacitor in order to be able to determine the capacitance C. (a) The 2-port series RC equivalent circuit of the capacitor of Figure 5.10. Where R is used to account for loss that may appear on the line. Applying the Y_{11} transform which effectively shorts port 2 (b).

There is one difference, the impedance of the capacitor, $Z_C = 1/j\omega C$, is different to that of the inductor. This will change equation 4.2 into:

$$\frac{1}{Y_{11}} = R + \frac{1}{j\omega C} \tag{4.4}$$

And changing it into a function of C:

$$C = \frac{1}{\omega \operatorname{Im}\left\{\frac{1}{Y_{11}}\right\}} \tag{4.5}$$

Equation 4.5 allows us to determine the capacitance from Sonnet simulations for a series modelled capacitor with two ports.

5

Results

In this chapter, the core of the thesis, we will evaluate the Center-Port resonator at its full-wave (l=λ) resonance f_0. But first, in order to do so we will set the stage giving the appropriate framework to relate the results to. Once we have done that, we are in the position to evaluate the device. Starting off with the initial CP design in the quite universal circuit simulator (QUCS), allowing us to demonstrate the design in its optimal conditions while still being practically relevant. After this first check, we move on to the real physical device and show how it preforms in cryogenic conditions. Then, inspection of the physical device is done in Sonnet, allowing to set up the device in close to real circumstances with the use of EM analysis. Finally, we arrive at the point where the stage is actually set for, showing the CP design sensitivity to its symmetry by allowing the DC bias line, the center port, to move away from its center position in QUCS.

5.1. Finding the influence of the Center Position of the DC port on the internal Q

From the point of view of the AC port of the CP, any signal that is lost due to the cavity and via the DC port are considered to be internal. What is considered to be internal is also described in the Theory section 2.5.2. The cavity looses signal by several types of losses, namely resistive, radiative or dielectric. In our case where the cavity will operate in its superconducting regime resistive and radiative loss will be close to zero or at least it should be. On the other hand what does needs to be taken into account is any signal that goes out of the DC port, which is also considered loss. It is important that the loss out the DC port is smaller than what is typically expected to be lost via the cavity. This does not mean that it is important that one is smaller than the other. The only thing that matters is the overall internal loss (cavity + DC port). However the loss on the cavity is a given (depending on the used materials), but the loss out of the DC port is controllable and should be optimized such that it less. Optimizing it any further will not be very fruitful as its part in the overall loss will become insignificant. In contrast, when simulating, the loss on the cavity is controllable by changing the attenuation factor (α). We adjust α until the maximum Q_{int} is about 10^5. Of course, the higher the better. The reason we choose this value is that this is typically feasible when the device is fabricated well, but not exceptional. For Q_{int} we consider the following:

Rating	**Q_{int}**
poor	1,000 [17]*
decent	10,000 [18][19]*
good	100,000 [21]
exceptional	1,000,000 [20]

*only total (unloaded) Q was reported

based on what you would get from the sources of internal loss (e.g. resistive, dielectric, radiation and two-level system (TLS) [41]). Now that we have set a benchmark for Q_{int} we can relate to it and observe what the influence is of the center position of the DC port on it.

5.2. QUCS simulation of the initial design of the Center-Port resonator

In this section we try to find out if the CP as described in section 2.1.3 will work in principle by simulating the setup shown in 4.2.1 in QUCS and calculating its Q_{int} (section 2.5). In simulation with QUCS we can check the system under its ideal (lumped and distributed elements) operation conditions within its physical and technical realistic parameters. One of the main parameters, for which it is not apparent what the 'ideal' value is, is the coupling capacitor (C_c) as it depends on the other parameters and determines how much of the signal is being transferred. So before we are able to address if the CP will work in principle, we will first figure out for which C_c the AC port, the feedline, achieves maximum power transfer ($|S_{11}|^2 = 0$). At the end of the section we will examine what the effect is on the Q_{int} if we choose a different value of C_c.

When the system achieves maximum power transfer it is said to be critically coupled ($\eta = \frac{1}{2}$). For that case the resonator is matched to the feedline at resonance. It then holds that $Q_{\text{int}} = Q_{\text{ext}}$ or similarly when $\kappa_{\text{int}} = \kappa_{\text{ext}}$. And indeed, as a sanity check, this means that for critical coupling at resonance ($\Delta\omega = 0$) the reflection parameter $S_{11} = 0$ (see equation 2.44) and thus $|S_{11}|^2 = 0$. Why the magnitude of S_{11} is squared is because it is defined in terms of its voltage ratio (see section 2.4.1) and thus needs to be squared in order to obtain the power ratio.

In trying to find for which value of C_c the feedline of the CP is critically coupled, we use the in QUCS simulated circuit as can be viewed in Experimental Methods section 4.2.1 Figure 4.3. A parameter sweep of C_c from 0.1-10 fF with 101 logarithmic points was performed in the frequency range of 9.32-9.38 GHz in 2001 linear points. This is the range for the second mode, where a full wavelength fits the cavity ($l = \lambda$). For the used cavity length l = 32 mm this second mode corresponds to a resonance frequency of ($f_0 = c/l =$) 9.37 GHz (based on the speed of light in vacuum c) and falls nicely within this frequency range. The second mode is the first mode that allows for the application of a DC bias as described in section 2.1.3. For the attenuation of the cavity an α of 1.00484 was chosen. This value was obtained indirectly from Schmidt et al.[42], in order to get a typical value of α for NbTiN. In the *Appendix* it is described how this is translated from the value in the paper to QUCS value of 1.00484. Although the value they got is for MoRe and not NbTiN. The NbTiN we use is fabricated by SRON who optimized their deposition process and will therefore potentially have a slightly lower α. To block off the DC port (port 2 in the figure) for high frequencies, an inductor of 80 nH is used which is more or less typical. The greater the inductor the better it will block off high frequency signals. However, anything greater than 80 nH will be extremely hard to fabricate. As the inductance increases so will the area the inductor covers, and the more area the inductor covers the more sensitive it will get for any dirt that may fall down on the chip.

From the C_c parameter sweep simulation the following figure, Figure 5.1, is attained. It shows the power transfer in the form of the reflection parameter, S_{11}, viewed from the AC-port (port 1). In the figure $|S_{11}|^2$ is given as a function of the frequency (f) for every value of C_c. The color indicates how much of the power is transferred, with dark blue no power being transferred and dark red maximum power transfer. Or, in other words, for dark red all of the signal is transmitted and none is reflected back. The point where all of the signal is transferred is when the system is critically coupled.

In order to obtain the C_c for which the system is (closest to) critically coupled ($|S_{11}|^2 = 0$) the minimum of $|S_{11}|^2$ for every value of C_c is taken from Figure 5.1. The minima are extracted by taking the lowest value of every horizontal line. The lowest point is the point at resonance, which changes due to C_c as it becomes part of the resonator. The minima are presented in Figure 5.2, but not in $|S_{11}|^2$. Related terms such as the magnitude and the real part ($\text{Re}\{S_{11}\}$) of S_{11} are used. From the figure it can be seen that the minimum of $|S_{11}|$ occurring at resonance is indeed purely real in accordance with equation 2.44. $|S_{11}|$ shows also a direct relation between the real part and the power transfer. Just like $|S_{11}|$ (and therefore $|S_{11}|^2$) $\text{Re}\{S_{11}\}$ equals zero at resonance when critical coupling is reached. The point for which $\text{Re}\{S_{11}\}$ is closest to zero is indicated by the red dotted line, at the point where $\text{Re}\{S_{11}\}$ = -0.0086 and C_c = 3.02 fF. So we have obtained the value of C_c for which the feedline is critically coupled to the resonator. Well, closest to, it is a bit undercoupled as can be seen from real part as it is slightly negative. This information would have been lost when only the magnitude was displayed. The power transfer for this slightly undercoupled C_c is therefore not exactly 100%, but 99.97%.

Now that we determined the right C_c we are able to answer what was addressed at the beginning and figure out how well the QUCS simulated CP works. In order to answer this we take a look at $\text{Re}\{S_{11}\}$ as a function of f for C_c = 3.02 fF, which can be seen in Figure 5.3. This is just a different representation of the horizontal line of Figure 5.1 at C_c = 3.02 fF. In the plot a dip occurs at resonance frequency (f_0) of 9.35528 GHz. Fitting this graph to the reflection parameter of equation 2.44, see section 2.5, the red solid line in the figure yields in agreement (with corresponding uncertainties due to fitting errors) f_0 = 9.35527967 GHz ± 0.09 kHz with κ = 465.2±0.3 kHz and η = 0.5043±0.0002. The first two parameters will give us by means of equation 2.35 the

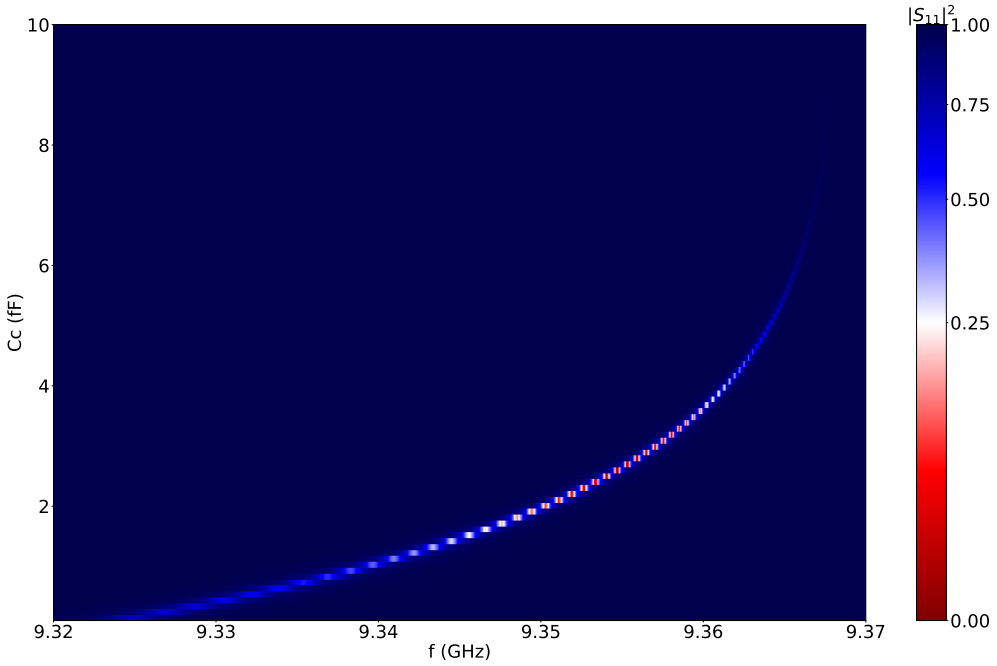

Figure 5.1: Heat map representation of the QUCS simulation as described in 4.2.1 of the Center-Port cavity design to show the power transfer. A parameter sweep of the the coupling capacitor (C_c) by means of s-parameter simulation. Every horizontal line corresponds to a s-parameter sweep of a certain C_c value as a function of the frequency (f). Where the color indicates the value of $|S_{11}|^2$. If $|S_{11}|^2$ is zero, indicated by a dark red color, then there is maximal power transfer. If it is dark blue, then $|S_{11}|^2 = 1$ and no power is transferred.

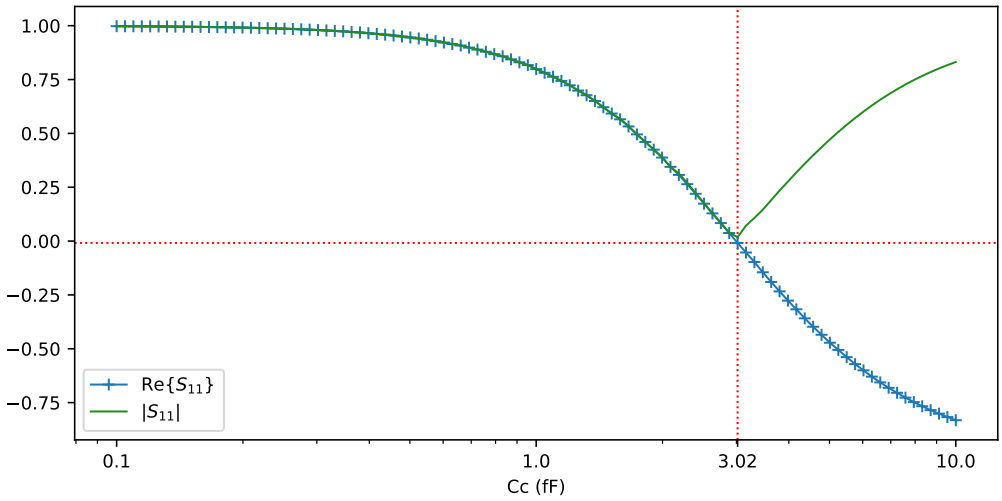

Figure 5.2: QUCS simulation of the CP to determine when C_c for the AC-port is critically coupled. The minima of the real part and the magnitude of the reflection parameter S_{11}, Re$\{S_{11}\}$ and $|S_{11}|$, in the frequency range 9.32-9.38 GHz are displayed. Critical coupling happens when $|S_{11}|^2 = 0$ or likewise when Re$\{S_{11}\}$ or $|S_{11}|$ equal zero at resonance. The point that is closest to critical coupling is the point where the red dotted lines cross.

total or loaded Q, $Q = 2.011 \cdot 10^4 \pm 1 \cdot 10$. And η will then give from equations 2.45 and 2.46 $Q_{int} = 4.056 \cdot 10^4 \pm 3 \cdot 10$ and $Q_{ext} = 3.988 \cdot 10^4 \pm 3 \cdot 10$. What we can see from the fact that η is not identical 0.5 and therefore that Q_{int} and Q_{ext} are not the same, is that the resonator is not critically coupled although close to it. This we already knew from Re$\{S_{11}\}$ at resonance, which did not equal zero. But most importantly, what these values further show, is that the device should work. They are more or less in the same order of magnitude of 10^5, a good resonator, as described in section 5.1.

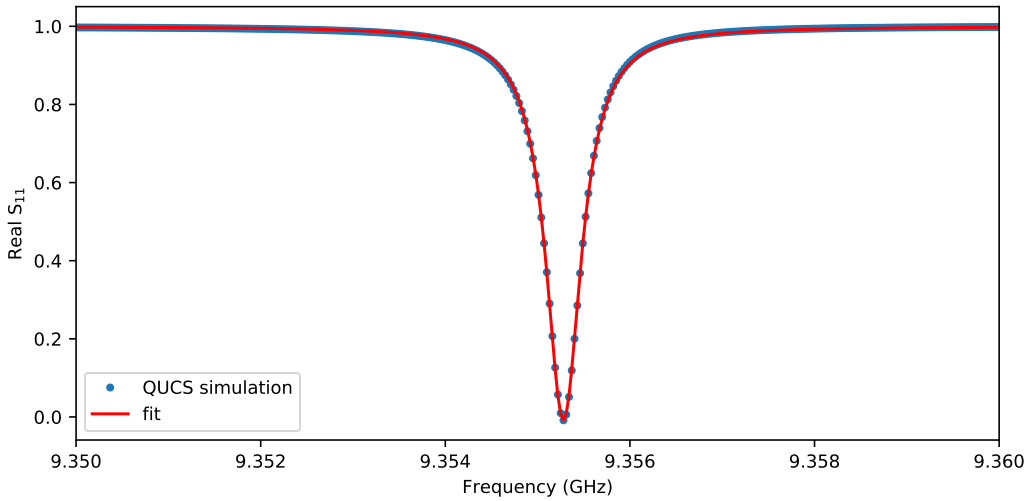

Figure 5.3: QUCS simulation of the CP for the (closest to) critically coupled AC-port. The real part of the reflection parameter, S_{11}, for $C_c = 3.02$ fF as a function of frequency. Fitted by equation 2.44 from which a Q_{int} of $2.5 \cdot 10^5$ is extracted.

What would happen if we had picked a different coupling capacitor. In order to check what the Q_{int} then would have been, we will determine Q_{int} for every simulated value of C_c (0.1-10 fF). This we do by using the exact same procedure as was used by the paragraph above. Only now we will repeat the procedure for the whole range of capacitances. From this we got the following figure, Figure 5.4. The first thing to notice is that Q_{int} is almost constant for all C_c. This is not surprising as there is no loss associated with the capacitor and therefore the Q_{int} should be independent of C_c. But when you look closer, at the inset of the figure, you see that there is some dependence. Q_{int} decreases from the lowest value of C_c to 8.7 fF, after which it starts increasing till the largest value of C_c. However, the uncertainty of Q_{int} does becomes increasingly large on increasing the difference in Q_{int} from its mean as can be seen from the light blue error-bars of Figure 5.4. Still, the uncertainty is not large enough to contribute Q_{int} deviation from its mean to it. So, this will not explain the behaviour of Q_{int}, and why it behaves as such we cannot say. What we can say, is that although the value of C_c determines the coupling to the cavity it is to a good approximation of no influence on the Q_{int} (for C_c of 0.1-10 fF). So, if we have a low Q_{int} we know it will not be very effective to spend a lot of time on changing C_c.

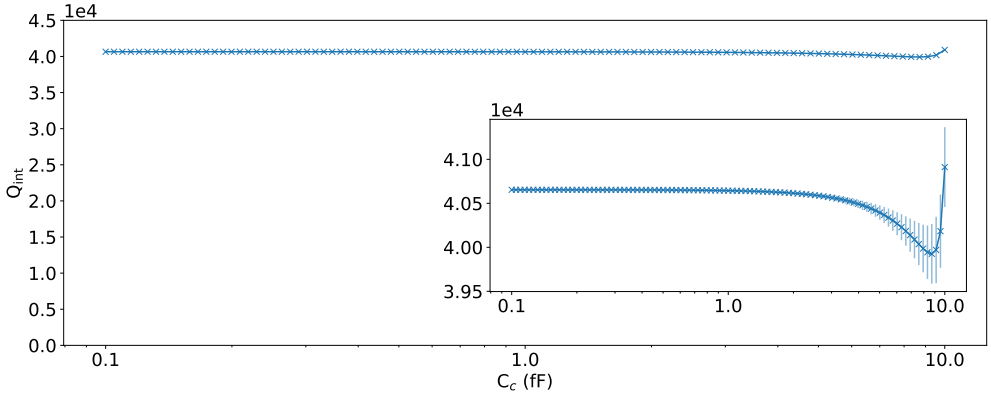

Figure 5.4: QUCS simulation of CP with the setup shown in Figure 4.3. Q_{int} is determined by the same procedure and over the same frequency range as was used for Figure 5.3. From the inset, which is just a copy of the main figure but with a different range of the y-axis, the details of the behaviour of the graph are better visible. Also, for the inset the uncertainty of Q_{int} is added and displayed by the light blue vertical (error-)bars.

5.3. Cryogenic low measured Q of the fabricated Center-Port resonator

We just established in section 5.2 that the CP should, in theory, work according to the QUCS simulation. Next we would like to know if the device we made following the fabrication steps described in chapter 3 will work as well, in order to make practical use of it. Just like before this means that we will determine its Q_{int}.The fabricated device that we will examine is based on the QUCS simulations and therefore also referred to as the CP.

The CP we will test is shown in Figure 2.5 and again in Figure 3.6. Its relevant geometric parameters are:

S	7.5 µm
W	3.125 µm
h	525 µm
t	100 nm
o	100 nm

with S the width of the center conductor, W the gap width between the center and the outer conductors, h the height of the dielectric substrate, t the metal thickness and o the over-etch as made visible in Figure 5.5.

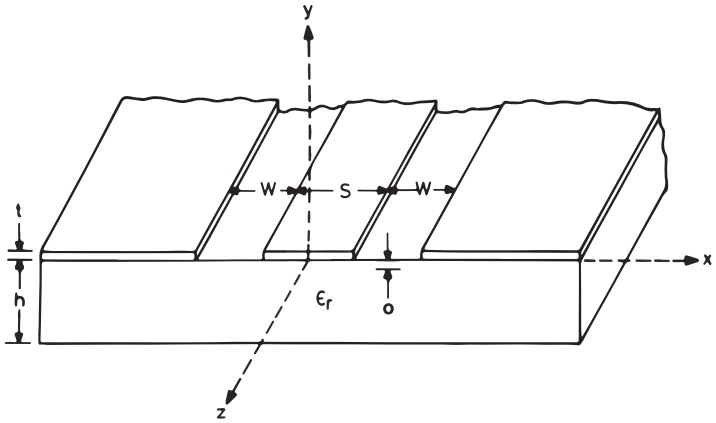

Figure 5.5: Schematic cross-section of a CPW(Figure modified from Garg et al. [30])

For preforming the measurement the chip was placed inside a dilution fridge and cooled down to 3.47 K. Then, reflection and transmission of the AC port was measured by means of a VNA. This was done by a power sweep from -30 dBm to 10 dBm with an increment of 1 dBm as described in section 4.1 for a frequency range of 4-8.934 GHz. Note, that here the reflection parameter is not described by S_{11}, but by S_{21} because of the directional coupler that is used.

After measurement the reflection parameter, S_{21}, is obtained and represented in Figure 5.6. The first thing to notice is that the data taken from measurement shows a sinusoidal behaviour in the frequency domain. From it, it is hard to see where the resonances occur and therefore to extract the wanted Q_{int}. The reason why the signal shows sinusoidal behaviour is because the coaxial cables, a transmission line, connected from the fridge to the VNA adds a time-delay (t_0) by $e^{j\,t_0\omega}$. To get rid of the added t_0, we need to know t_0. In order to determine t_0 the phase (Ph$\{S_{21}\}$) is fitted linearly, as can be seen from the inset of the figure. From the slope the value of t_0 is retrieved, taking on the value $t_0 = 54\pi$. And the offset is given by $\phi_0 = 214\ \pi$. Correcting for this phase offset will not allow you to better distinguish the resonances, but will allow you to fit without the use of an additional parameter to account for the reference phase. So in order to correct for the time-delay and the wrongly chosen reference phase we use the following:

$$S_{21}^* = e^{-j(t_0 f + \phi_0)} S_{21} \tag{5.1}$$

where S_{21}^* is the phase corrected reflection parameter. From the resulted real, Re(S_{21}^*) and, especially, the absolute value, $|S_{21}|$, it seems that at around 7 GHz a resonance is present. Note that $|S_{21}|$ takes on the amplitude of Re(S_{21}) , as it should, being the magnitude of the sinusoid. Also Re$\{S_{21}^*\}$ is not the amplitude and differs every so slightly from $|S_{21}|$.

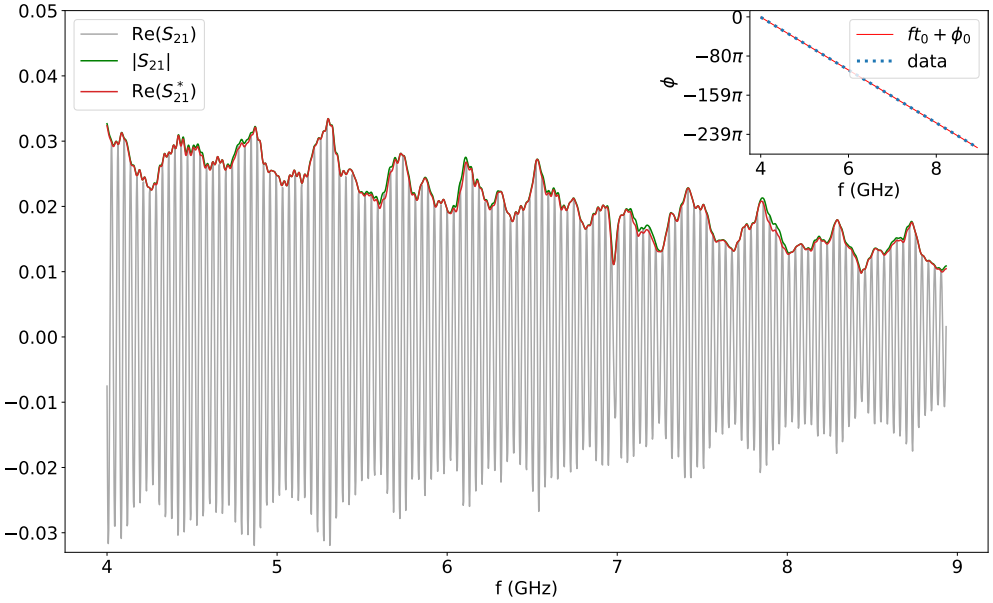

Figure 5.6: Phase correction of the real part of the S_{21} (Re$\{S_{21}\}$) data obtained from the DIY4K measurement of the CP at 3.47 K and 10 dBm. The grey graph shows the data directly obtained from measurement and contains both a time-delay (t_0) and a phase offset (ϕ_0). To correct for both t_0 and ϕ_0, the phase of S_{21} is fitted by a first degree polynomial as shown in the inset. From this fit we obtained $t_0 = 54\ \pi$ and $\phi_0 = 214\ \pi$. By applying $e^{-j(f\,t_0+\phi_0)}$ to Re$\{S_{21}\}$ the red curve is obtained, labelled as Re$\{S_{21}^*\}$. The reason to correct the data is that in this new form it allows for the determination of the Q-factor. There is also a green curve, $|S_{21}|$, which shows as expected the amplitude of the sinusoidal data. It also shows that Re$\{S_{21}^*\}$ is not the amplitude, although close to it.

To identify the resonance better we take a look at the magnitudes of the transmission parameter, $|S_{32}|$, in Figure 5.7. So indeed, there appears to be a resonance around 7 GHz, with a clear peak in $|S_{32}|$ at 6.98 GHz. Beside that, there are two more clear-cut peaks visible, one at 6.01 GHz and one at 8.44 GHz. But, because of its correspondence with the dip in $|S_{21}|$, its seems most likely that the resonance is at 6.98 GHz. The one we want to check for its internal quality factor.

Now that we have identified the resonance we are ready to determine its Q_{int}. In order to do so we again make use of the real part of equation 2.44. We fit this equation to the phase corrected real part of the reflection parameter Re$\{S_{11}^*\}$ shown in Figure 5.8. By using the data containing the phase correction we do not have to introduce any new fit parameters for the phase. This will not only result in a less complicated fit function but also in a better fit as can be seen in the Appendix. But we do need an extra fit-parameter to take the

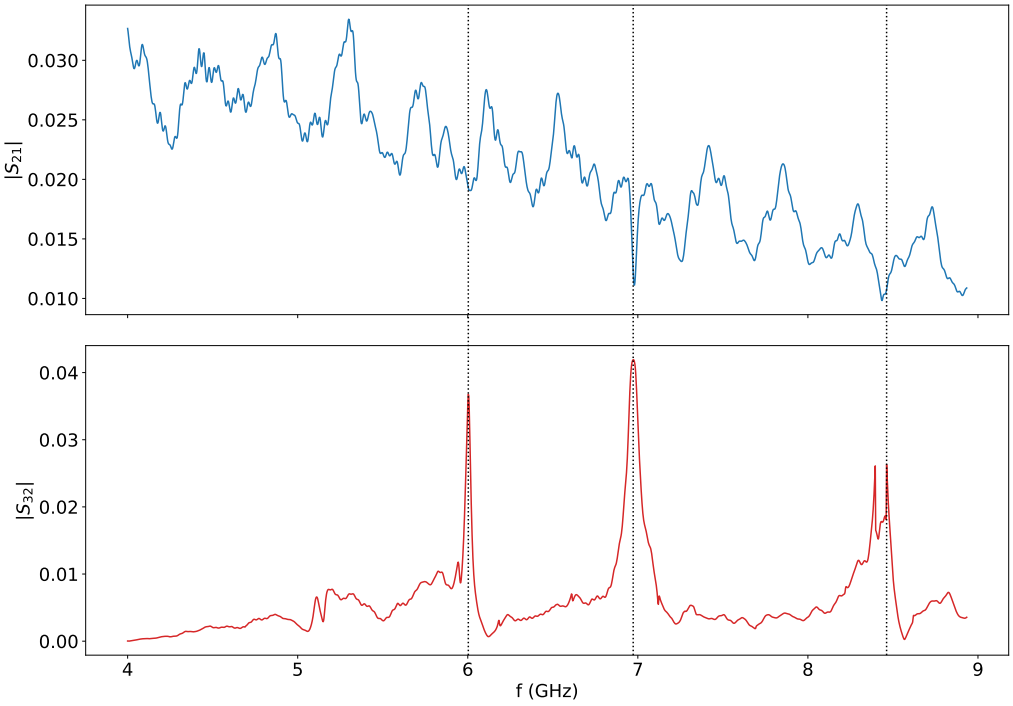

Figure 5.7: Reflection (S_{21}) and transmission (S_{32}) DIY4K measurement of the CP at 3.47 K and 10 dBm. S_{32} shows in red where the resonances of the cavity occurs, which are at 6.01, 6.98 and 8.44 GHz. With the second resonance mode most likely at 6.98 GHz, as it corresponds to the most prominent dip in the blue graph S_{21}. This mode is where Q_{int} of the resonator is determined. The reason that S_{32}

attenuation coming from both the directional coupler as well as the line leading to the ports into account. This is done by using equation 2.47 with t_0,ϕ_0 = 0, which introduces the overall attenuation factor (A). In order to use this fit-function appropriate and really get the Q of the resonance, the frequency range for the fit is set closely around it. The part of the data that is used to extract the fit parameters can be seen in Figure 5.8a. From the fit we retrieved the fit-parameters A = 0.0202±0.0001, f_0 = 6.9802 GHz ± 0.5 MHz, κ = 35±2 MHz and η = 0.2364±0.006 (< 0.5, undercoupled). These values give in turn by means of equation 2.35 Q = $2.0{\cdot}10^2{\pm}1{\cdot}10$, Q_{int} = $2.6{\cdot}10^2{\pm}1{\cdot}10$ and Q_{ext} = $8.5{\cdot}10^2{\pm}5{\cdot}10$. On a side note, these are all uncertainties of the fit only, not taking into account any measurement uncertainties. The measurement will have stochastic as well as systematic errors. Of these errors, likely the most prominent will be the systematic error coming from the uncalibrated cable resonances. Back to the results, the Q_{int} is much lower than what we got from the QUCS simulation and is also much lower than the 10^5 set in 5.1 for a good resonator. It is even so low, an order of magnitude lower than what we deemed a poor resonator, that we can conclude that the device does not work.

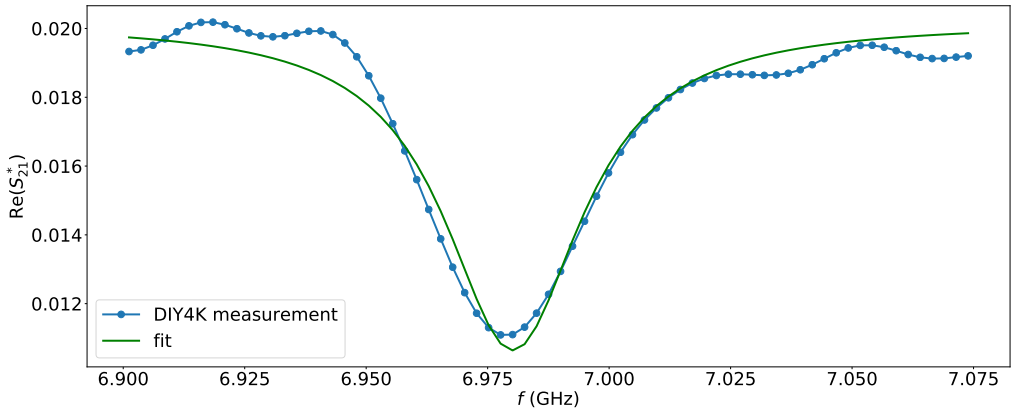

(a)

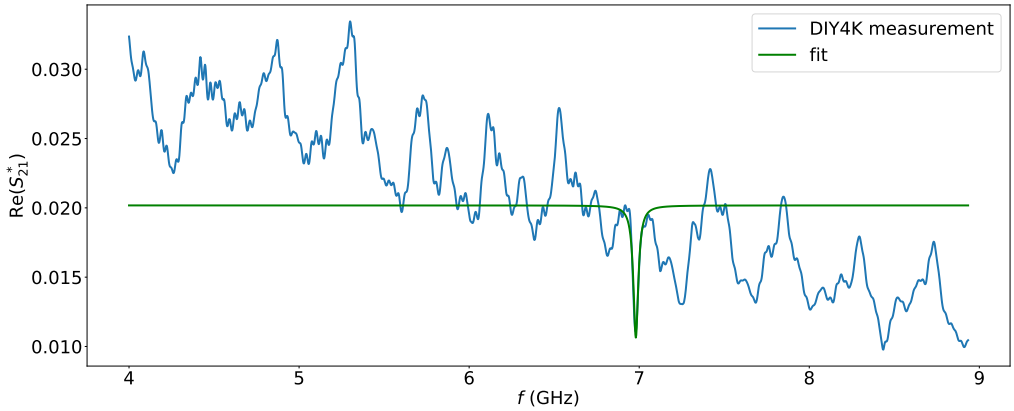

(b)

Figure 5.8: DIY4K reflection S_{21} measurement at 3.47 K and 10 mdB to determine Q_{int}. The real part of S_{21} shown here is corrected, indicated by *, for both a time-delay (t_0) as well as the reference phase (ϕ_0) by means of equation 5.1 (ϕ_0 and t_0 are obtained from fitting the phase of S_{21} shown in Figure 5.6). This data is fitted by equation 2.47 with t_0,ϕ_0 = 0 over the reduced range from 6.900-7.075 GHz as shown in (a). From the fit we obtained A = 0.0202, f_0 = 6.9802 GHz, κ = 35 MHz and η = 0.2364, which in turn gives Q_{int} = 264. η shows that the system is undercoupled being significantly smaller than 0.5. In (b) the fit for the whole measured frequency range is shown.

5.4. Inspection of the fabricated Center-Port resonator

In order to better understand why the fabricated CP (see Figure 5.9a) does not work ($Q_{\text{int}} \ll 10^6$) we need

to find out what is causing it. From what we learned in Theory (section 2.5.2) and at the beginning of this chapter (section 5.1) is that there are actually two types of loss that attribute to Q_{int}. One is what you would expect, the internal loss, consisting of radiative, resistive and dielectric loss of the lines and in particular the frequency dependent loss of the cavity line. This loss is however depending on the material and the operating environment but not specific to the design and is therefore hard to control. On the other hand, the other type of loss, the loss out of DC port is specific to the design and is something we have control over. For this loss we want to check how good the (choke) inductor (L) (see Figure 5.9c) of the DC line is at blocking off the high frequency signal of the cavity (i.e. how well it behaves like an inductor). But first we will determine the capacitance of the coupling capacitor (C_c) (see Figure 5.9b) to check if it indeed behaves like an capacitor, if it agrees with measurement (section 5.3) being undercoupled ($Q_{\text{int}} < Q_{\text{ext}}$) and how its capacitance corresponds to what was originally intended in the design of the CP. We will end this section with the part where we want to figure out how much of the signal is actually leaking out of the DC port. This will give us insight which of the two types of loss (internal or via the DC port), that are of influence on the Q_{int}, plays the bigger part.

5.4.1. Sonnet Simulation of the Gap Coupling Capacitor (C_c)

As promised, we start of with the the coupling capacitor (C_c) shown in Figure 5.9b. We would like to know if the fabricated capacitor is working as expected. What this means is that it only allows to effectively pass high frequency signals. In order to find this out we will determine its capacitance as a function of frequency.

In designing C_c our goal was to obtain a capacitance equal or at least close to 3.2 fF, the value we obtained from the QUCS simulation (section 5.2) for which the desired (close to) critical coupling was obtained. To achieve the desired value we based our design on the different types of capacitors and corresponding capacitances of Goppl et al. [43]. From these capacitors we decided on the two-finger gap capacitor as shown in Figure 5.9b. To determine its capacitance we simulated the S-, Y- and Z-parameters of the design in Sonnet EM as described in section 4.3.2 with the set-up displayed in Figure 4.8 over a frequency range of 0.0-9.0 GHz (ABS). With the upper limit well above the measured resonance frequency of around 7 GHz. For the simulation we used the following tabulated parameters for the top-layer consisting of air and the bottom layer, the substrate, of (intrinsic) silicon:

	Top-layer (Air)	**Bottom layer** (intrinsic Silicon)
d (μm)	525	525
ρ (Ω·m)	0	0.044
ϵ_r	1	11.9
$\tan\delta_\epsilon$	0	0.004
μ_r	1	1
$\tan\delta_\mu$	0	0

Table 5.1

where d is the thickness, ρ the resistivity, ϵ_r the electric relative permittivity, $\tan\delta_\epsilon$ the dielectric loss tangent, μ_r the relative permeability and $\tan\delta_\mu$ the magnetic loss tangent. The d = 525 μm is chosen as this is typical for the silicon wafers we use. For air we used the same size for symmetry sake so that the propagating EM waves will be realistically simulated up to 525 μm both above and below. To simulate the structure of C_c we used in between both dielectric layers a 2D metal layer that is, apart from its kinetic inductance of 1.5 pH/sq, lossless. This means that its sheet resistance R_s = 0 as we are under the assumption that the metal is superconducting.

The result of the $Im\{Y_{11}\}$ simulation in the form of the capacitance (see equation 4.5) are presented in Figure 5.10. From the data (blue line) in the figure the first thing that is apparent is that the capacitance varies only slightly. So slightly, that by looking at the main figure you could not tell. Therefore we can safely say that to a good approximation C_c is constant and behaves like an ideal capacitor with a capacitance of 21 fF in its operating regime. Only when zooming in vertically the variation becomes visible. It start of at 0 GHz around C_c = 20.75 fF and reaches at the end of the range a value of 20.78 fF at 9 GHz. Periodically the value of the capacitance is jumping up and then decreases for a certain range, ending up with a value higher than before the jump. This results in the general exponential increasing behaviour captured in the fit ($b\exp(af)+c$) by means of the least squares method, the red line, with a = 0.1774, b = 0.0081 and c = 20.74. What is further of notice when looking at the inset is that the data fluctuates and that these fluctuations are decreasing with increasing frequency. These fluctuations hint on numerical errors caused by the calculations of finite accuracy used in the simulation. Still, it is unclear why the fluctuations appear to be depending on

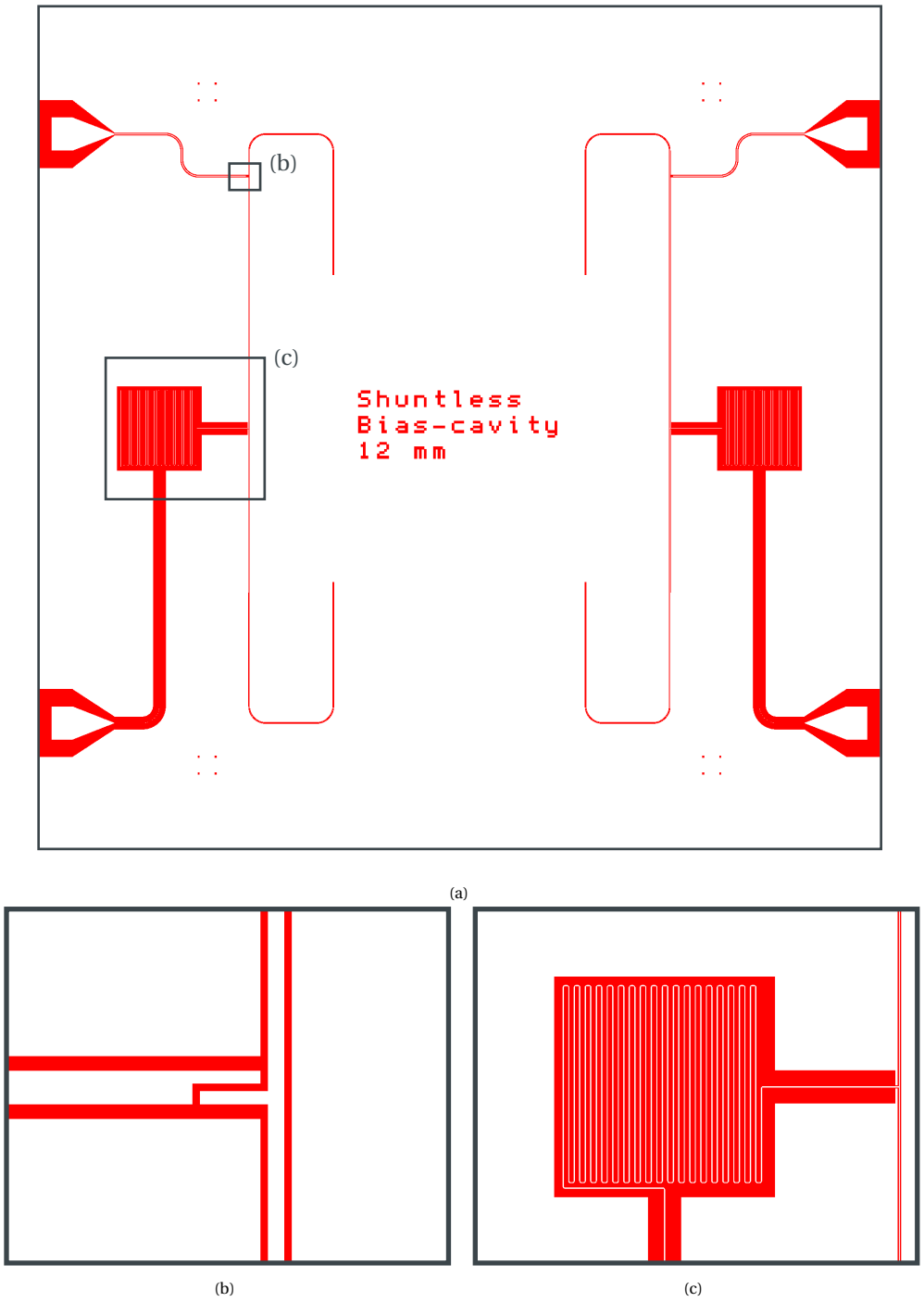

Figure 5.9: The design as it was send to the e-beam containing two mirrored CPs. The outer box shows the border of the to be exposed 1×1 cm chip. Where in red the part is shown that will be exposed, and, because positive resist is used, it is the part that after fabrication shows the substrate Si. In white the unexposed part is shown and will after fabrication represent the metal NbTiN. The TL cavities are the C-shaped lines closest to the center of the chip. Connected to it is are the AC-line via the coupling capacitor (C_c) (b) and the DC-line via the choke inductor L (c). (b) a zoom of C_c, a two-finger gap capacitor. And (c) another zoom but less magnified showing L, the meander-line inductor of 36 turns.

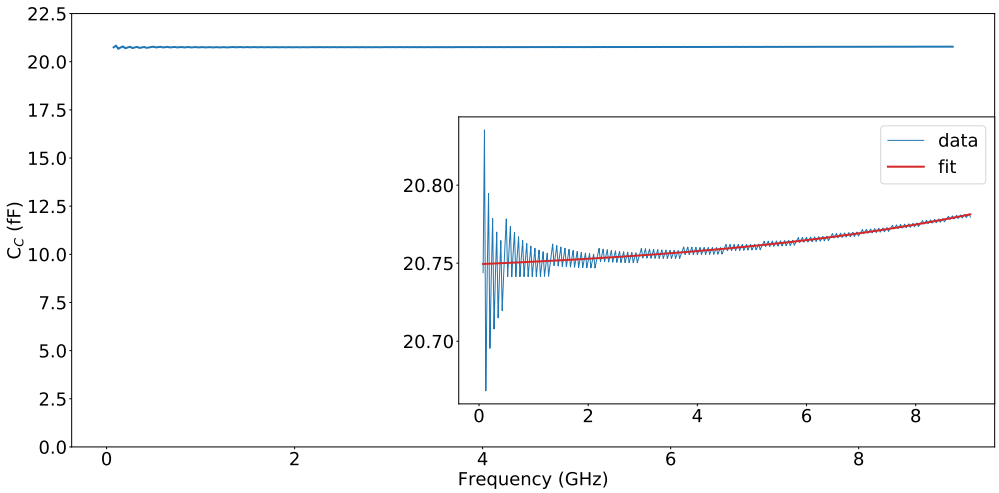

Figure 5.10: Sonnet EM simulation of the coupling capacitor (C_c) as shown in Figure 5.9b using the parameters of Table 5.1. C_c is obtained from simulation by Y_{11} using equation 4.5. From the main figure C_c appears to be constant. This is not quite true as can be seen from the inset, showing a slight increase in the capacitance. The data is fitted by $b\exp(af)+c$ with a = 0.1774, b = 0.0081 and c = 20.74, and shown in red in the inset. From the fit we obtain C_c = 20.75 fF at f = 0 and at the end of the frequency range at f = 9 GHz a C_c of 20.78 fF. Therefore, to a good approximation C_c behaves like an ideal capacitor with a capacitance of 21 fF.

the frequency. It could be that it is related to the method we use to simulate, ABS, that allows to simulate a lot faster.

So the capacitance of 21 fF we obtained from the simulation is almost four times greater than the intended 3.2 fF. This raises the question of what the effect is of this higher capacitance of C_c. For the Q_{int} we already discussed in section 5.2 that the value of C_c is not of influence as can be seen in Figure 5.4 of . Backed by the argument that there is no loss associated to the capacitance itself. On the other hand, for the Q_{ext} this is a different story. Because C_c determines how the external circuitry is coupled to the resonator, it is of direct influence on the Q_{ext}. What we saw from Figure 5.2 of the same section is that values higher than 3.2 fF are in the undercoupled regime. In agreement with the measurements in section 5.3 that the system is undercoupled.

5.4.2. Sonnet Simulation of the Meander-Line Choke Inductor (L)

Moving to the other component that was simulated in QUCS by a lumped element, the choke inductor (L). The part of the CP that is considered to represent the choke inductor (L) and what we will discuss here is shown in Figure 5.9c. In contrast to C_c the inductor will definitely effect Q_{int}. Not by its inductance itself as (just like the capacitance) there are no losses associated to the inductance, but by how much of the signal of the cavity it is able to block off. It does so as it forms the node that connects the DC line to the main line. For L, the piece of CPW of Figure 5.9c, we want to know how well it is capable of preventing high frequency signals to escape, while still allowing low frequencies to pass. This we will try to figure out by determining its inductance. Where we can simply state that based on the impedance ($j\omega L$), the larger the inductance the better.

In order to determine the inductance of L we simulated the S-, Y- and Z-parameters of the design shown in Figure 5.9c in Sonnet EM with the set-up shown in Figure 4.6 following the steps in section 4.3.1. The inductor consist of a meandering CPW line of 36 turns with a total length of 34 mm, a separation of the lines of 17.5 μm and, just like the cavity line, a line thickness of 7.5 μm. We performed the simulation over the frequency range of 0.01-10 GHz with the same parameters as listed in the table of section 5.4.1 and discussed in that same section.

The results of the simulation are presented in Figure 5.11. In Figure 5.11a the inductance, obtained from $Im\{Y_{11}\}$ by means of equation 4.3, is shown. The other figure, Figure 5.11b, is realized by taking the magnitude of the reciprocal of Y_{11} and shows the magnitude of the total impedance $|Z|$. Figure 5.11a looks quite different than the result we got for C_c (see Figure 5.9b). Opposite to the capacitor L is not close to being ideal (i.e.

constant), but far from it. That L is no ideal inductor is also really clear from 5.11b where an ideal inductor of around 22 nH (= $L(f = 0)$) is plotted on top of the data. There are clear resonance peaks visible in both figures, where L and R reach their maximum value at around 2.1 GHz, 5.7 GHz and 8.4 GHz, its so called self resonant frequencies (SRFs). These resonances show that the inductor behaves like a TL, which is not surprising considering that its total length of 34 mm is even greater than the length of the cavity of 12 mm. Therefore its size is certainly comparable to the wavelengths that exists.

In determining L by means of equation 4.3 we mistakenly considered the meander-line inductor as an ideal inductor. Close to resonance the supposedly ideal inductor L (Figure 5.11a) can be approximated by an series inductor L_0 and a parallel parasitic capacitor C_p , by:

$$L = \frac{L_0}{1 - L_0 C_\mathrm{p} \omega^2} \tag{5.2}$$

where the capacitance now arises from the close proximity of the central conductors and not from the central conductor to its outer conductors like for a 'normal' line of CPW. Only the lumped elements containing imaginary impedances are considered as they are the only one contributing to L as it is derived from $Im\{Y_{11}\}$ by equation 4.3. From the equation 5.2 you can see why L changes sign immediately after reaching its maximum. This is the point where the parasitic capacitance gets the overhand ($L_0 C_\mathrm{p} \omega^2 > 1$). Note that even though the graph shows that L becomes equal to zero, it does not reach zero or comes close to it at resonance. What is evident from equation 5.2. The graph incorrectly connects the maximum point to its minimum point at resonance. That L is indeed behaving like a capacitor from the point it reaches its minimum at resonance can be nicely seen from Figure 5.11b, where the impedance goes down on increasing frequency, just like a capacitor ($|Z_L| = 1/\omega C$).

It is already quite clear that the inductor is not working as expected. It is not constant (Figure 5.11a) and its impedance is for the majority of the frequencies much lower than for its ideal case (Figure 5.11b). Moreover it is not working as an inductor, with a impedance that is not increasing upon increasing frequency. Lets quantify how it relates to the ideal case. For this case we use 22 nH, the value L has at zero frequency (which for an ideal inductor would not vary over frequency). This gives us at f_0 = 6.98 GHz an impedance of 967 Ω. What we really got as indicated by the red dot in Figure 5.11b is a marginally 87 Ω. Less than a tenth of the ideal case. Besides, this ideal case is based on a much lower value than we initially intended and used in the QUCS simulation of section 5.2 of 80 nH. In that case the impedance would be about four times greater than for the 22 nH case with $|Z|$ = 3509 Ω. So, besides that it is not working as an inductor, it is also performing much worse at f_0 than we tried to achieve, with an impedance 40 times smaller.

What we can learn from the bad performance of the meander-line inductor is that one should be careful about the total length of the inductor. The reason for this is that it is the most likely cause of its low SRF (2.1 GHz). Supported by the fact that its length (34 mm) is several times larger than that of the cavity (12 mm) and therefore standing waves could form in the operating frequency range. Why one should stay clear of the SRF is because after this frequency its inductance will only function better than its ideal counterpart for very limited frequency ranges as shown in Figure 5.11b. Also it is really difficult to know beforehand were these resonances occur and therefore the changes are that you are much worse off.

In order to prevent operating above the inductor's SRF one could decrease the length of the inductor. But its inductance of 22 nH is already much less than the intended 80 nH and therefore decreasing its length would make it even lower. The main problem of a meander-line inductor is that the current through adjacent tracks is flowing in opposite directions, and thereby significantly lowering its inductance. Even a straight wire of the same length has therefore a larger inductance. So one could perhaps adapt a different type of inductor like a spiral inductor, although this would make fabrication a lot harder as it needs a air bridge to connect to the center part of the spiral. And that is the whole idea of the CP, an easier design. However there is another way to decrease the inductors length while increasing its inductance. That is by making use of the kinetic inductance (L_k) as proposed by Annunziata et al. [44] instead of the magnetic self-inductance like we used here. Because kinetic inductance (L_k) scales inversely with the cross-section of the wire, opposed to the self-inductance which only scales logarithmically on the diameter [45], L_k can become quite large while significantly reducing its length if the cross-section is small. Annunziata [44] reported typical values of 1 nH/μm for NbN with t = 15 nm and S = 100 nm. To put this in respect, for our inductor this is only 0.65 pH/μm for NbTiN with t = 100 nm and S = 7.5 μm. So, this could potentially both solve the low SRF and increase its overall inductance.

In conclusion, the meander line inductor L we designed does a very poor job at preventing the high frequency signals to escape from the cavity. Therefore it could potentially be the cause of the low Q we measured

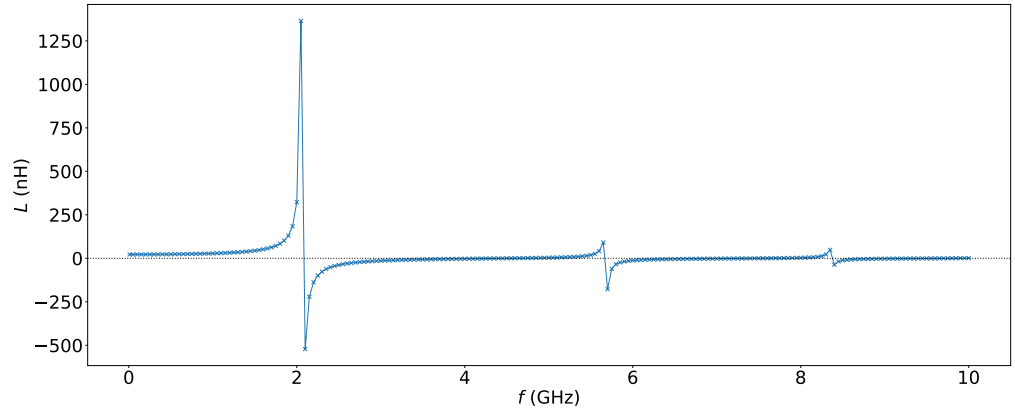

(a)

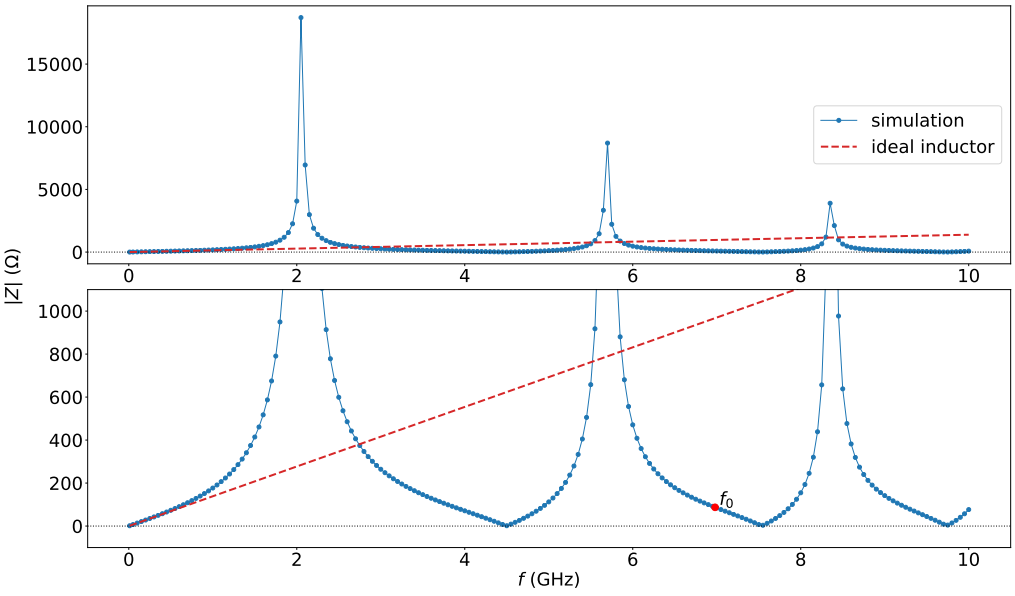

(b)

Figure 5.11: Sonnet EM simulation of the meander-line inductor (L) as shown in Figure 5.9b using the parameters of Table 5.1. L is obtained from simulation by Y_{11} using equation 4.3. The figures show three self-resonance frequencies in the range 0.01-10 GHz occurring at 2.1 GHz, 5.7 GHz and 8.4 GHz. In (a) the inductance flips sign at those resonances in accordance with equation 5.2. The inductor's effective impedance is shown in (b), where the bottom figure shows a vertical zoomed in version of the top one. In the bottom figure the resonance frequency f_0 = 6.98 GHz is indicated by the red dot. It shows that CP operates far above its first self-resonance frequency. And as a consequence its impedance is much smaller than that of an ideal inductor with a inductance equal to the value reached at f = 0 of L = 22 nH.

in section 5.3. In the next section we will discuss if it is the leakage out of the DC port discussed here that is the main cause of the low measured internal Q or that it is the loss associated with the cavity itself.

5.4.3. Cryogenic Measured Leakage of the DC Port

In this last subsection we will try to answer where the low measured internal Q in section 5.3 is coming from. If it is coming from the leakage out of the DC line, because of the poorly designed inductor L which seems to be unable to effectively prevent the signal of the cavity to escape, as we discussed in subsection 5.4.2. If that is not the case, then it would apparently be that the cavity itself has significant internal loss. This will show us if its an issue related to the design of the CP (leakage) or if it has to do with the fabrication or measurement of the CP (internal loss of the cavity). In order to address the question we will relate the power measured in the DIY4K that is transmitted to the DC port $|S_{31}|^2$ to the total transmission $1-|S_{21}|^2$.

For determining the leakage we will use the same measurement as described in 5.3. From that measurement we obtained Figure 5.12, a digital display of the VNA. The reason why we present it like this is because we did not retrieved the data corresponding to S_{31}. However, we did retrieve the data for both S_{21} and S_{32}. Where we can get S_{31} from S_{32}. This is because both S_{31} from S_{32} represent the same signal, transmission from the AC-port (1 and 2) to the DC-port (3). Only there is a difference in the attenuation. Mainly because of the directional coupler that attenuates the signal coming from 1 to 3 by 20 dB, while leaving the signal from 2 to 3 unattenuated. The actual attenuation difference between S_{32} and S_{31} that we get by relating the red dots in the figure using WebPlotDigitizer is -18.6 dB ($S_{32} \rightarrow S_{31}$) at $f_0 = 6.98$ GHz. Why this differs from the -20 dB of the directional coupler is due to the difference in the attenuation of the lines. Where apparently the cables connected to 2 attenuate the signal by 1.4 dB more than the cables that are connected to 1. And thus S_{31} is given by:

$$S_{31} = S_{32} - 18.6 \text{ dB} \tag{5.3}$$

where of course S_{31} and S_{32} are taken in dB.

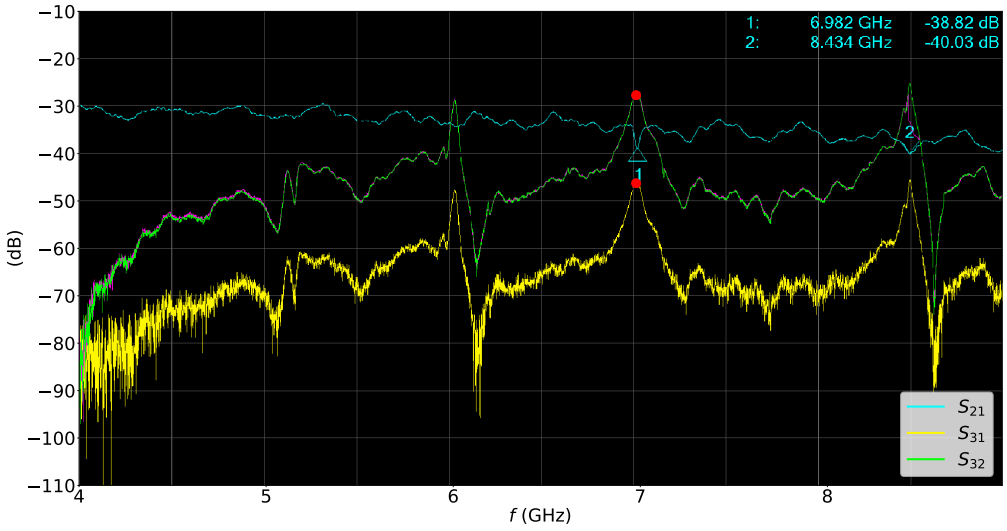

Figure 5.12: VNA display window of a power-sweep at 0 dBm for several S-parameters. It shows two different transmission parameters S_{31} and S_{32} which are actually the same parameters aside from their path differences and the fact that S_{31} passes a -20 dB directional coupler. Only, for S_{32} the data was taken, but for S_{31} it was not. In order to check their attenuation difference the red dots at $f_0 = 6.98$ GHz are extracted by WebPlotDigitizer to relate the two transmissions. From it we got an attenuation difference of -18.6 dB ($= S_{31} - S_{32}$) and therefore S_{31} and S_{32} are related by equation 5.3.

Now that we have the right data we are ready to determine the leakage of the DC port. But first we will normalize the reflection S_{21} and the transmission S_{31} using the following norm:

$$\text{norm} = \frac{1}{|S_{21}|^2 + |S_{31}|^2} \tag{5.4}$$

here the powers of S_{21} and S_{31} are taken at resonance f_0 = 6.98 GHz, where $|S_{21}|$ reaches its maximum within the frequency range 6.900-7.075 GHz. By taking S_{31} from S_{32} using equation 5.3 and applying the norm to both S_{21} and S_{31} Figure 5.13 is obtained. It shows the reflection, the leakage and the internal loss in terms of power. From the reflection $|S_{21}|^2$ we can see that not all of the power is reflected back at resonance but that part of it is lost to the system. The part that is not reflected back (1-$|S_{21}|^2$) is either lost via the DC-line ($|S_{31}|^2$) or lost internally by the cavity. Loss of the DC line is captured by $|S_{31}|^2$ whereas the internal loss is obtained indirectly. It is the only loss remaining and therefore retrieved by subtracting the leakage from the part of the signal that is not reflected 1-$|S_{21}|^2$-$|S_{31}|^2$. Of the loss, the signal that is not reflected back, 8.2% is leakage and the other 91.8% is lost internally at f_0. So the loss out of the DC port is thus much less than that is lost internally, what was already quite clear from the figure.

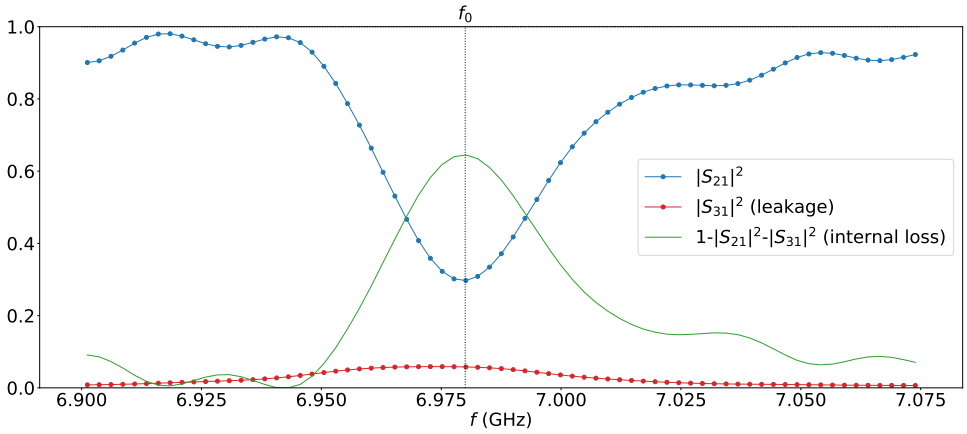

Figure 5.13: DIY4K measurement of the reflection (S_{21}) and transmission (S_{31}) in terms of power. $|S_{31}|^2$ is not measured directly but inferred by equation 5.3 and Figure 5.12. Both $|S_{21}|^2$ and $|S_{31}|^2$ are normalized by the same norm given in equation 5.4 under the assumption that the attenuation of both S_{21} and S_{31} are equal. From the power that enters the cavity 1-$|S_{21}|^2$ = 0.702 at resonance f_0 one part is lost (leaked) via the DC port $|S_{31}|^2$ = 0.058 and the remainder is lost internally 1-$|S_{21}|^2$-$|S_{31}|^2$ = 0.645. This leads to a relative leakage loss of 8.2% and 91.8% internal loss.

To conclude this section, the main reason of the low measured internal Q ($Q_{\text{int}} \ll 10^5$) of section 5.3 is due to the bad internal loss which is more than 10× higher than the loss of the DC port. Even though the choke inductor L, as we saw in subsection 5.4.2, does a very poor job at preventing high frequency signals to leave the cavity (much less than the already low ideal inductor of 22 nH). Because the internal loss is much higher than the leakage of the DC port we cannot say if it is an inherent problem of the CP design. Especially because the inductor was not designed well and could potentially preform much better. What we can say is that the internal loss is the biggest issue and is much more than we would expect based on the QUCS simulations of section 5.2, where we used a typical attenuation factor [42]. Also, much higher Q's have been reported for NbTiN resonators with $Q > 10^5$ [10]. It is hard to say what is actually causing the internal loss to be so high as there are many factors that could potentially be the cause. For example, it could be that the temperature during measurement was too high. Or that the chip suffered from significant contamination during or after fabrication. It remains a guessing game, we do not know.

5.5. Simulating in QUCS the influence of symmetry on the internal Q of the Center-Port design

Up until now we could not say much about the CP design and how well it is performing. By performance we mean the internal Q, which is affected by the design in the form of the DC port and how much of the signal is lost/leaking there. In section 5.3 we measured a low internal Q of the CP. However, we saw in section 5.4 that this low Q_{int} was not only caused by the leakage but was mainly because it suffered form large internal loss. In this section we will investigate the influence of symmetry on Q_{int}. To do so we will simulate the effect of moving the galvanically connected DC-port off-center in QUCS. After that we will also simulate what adding an identical extra symmetric AC-port will do. These simulations will be performed for both resistively coupled AC-port(s) as well as capacitively coupled AC-port(s). Where the latter single AC-port case is in accordance

with the CP design.

5.5.1. Sensitivity of the Center-Port design to the exact position of the DC galvanic port

We will try to determine what will happen to Q_{int} if we move the DC-port away from its center position. It will show us how sensitive the CP is to the exact position of its center-port. What the influence on the Q_{int} will be if you are, for example due to an error in fabrication or design, a bit off-center. In that case will your resonator still operate close to its maximum or will it significantly worsen. We will check its Q_{int} influence on the position of the DC-port for two coupling cases of the AC-port, namely resistive and capacitive.

What we will do to check the DC-port's sensitivity to its position being off-center is to simulate the set-up shown in Figure 4.4 and Figure 4.5 of Method section 4.2.2 in QUCS. In both set-ups the DC port (port 2) is galvanically connected to the cavity, meaning that its impedance matches the impedance of the TL. For the AC-ports, port 1 and 3, we will start off with the case where port 1 is resistively coupled ($R3$ = 5 kΩ) and port 3 is closed off ($R3$ = 10 EΩ). Although coupling the AC-port in this way is not in correspondence with the CP design nor is it likely that anyone would, but it is easier to understand without the frequency dependent impedance of the capacitor. For the set-up we performed a S-parameter simulation from 9 to 11 GHz for every value of the parameter *offcenter*. *offcenter* is the distance of the DC port with respect to the center position of the TL cavity, where negative values correspond to the center moving to the left and positive values to the right. This parameter we ran for a list of 201 values that ranged from -0.5 to 0.5 mm logarithmically from zero, in order to have more points close to zero, and we included zero. For the total length of the TL cavity we choose l = 30 mm with its resonance at $f_0 = c/l$ = 10.0 GHz, in the middle of the set frequency range. The attenuation we set in such a way as to get a Q_{int} of around 10^5 as we discussed in section 5.1, which let to α = 0.01 dB.

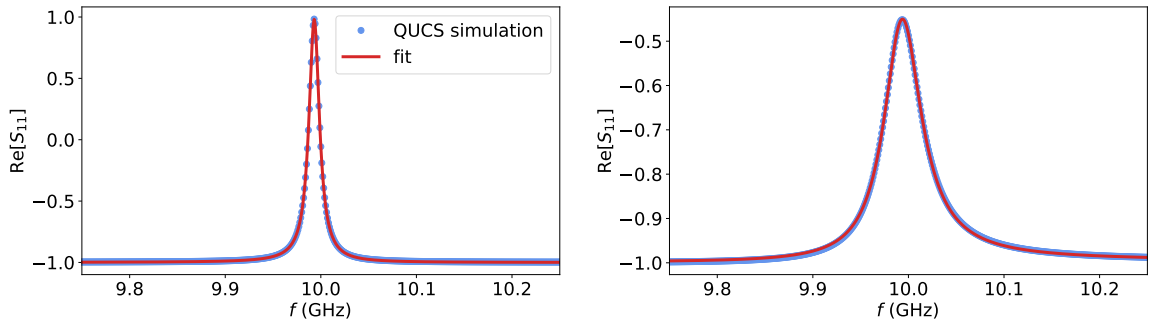

(a) (b)

Figure 5.14: QUCS S_{11} simulation of the 2 ports CP setup with a resistively coupled AC-port as shown in Figure 4.4 with $R3$ = 10 EΩ for *offcenter* equalling (a) 0.0 and (b) -0.5 mm. The fits are obtained by means of equation 2.47 with A = 1 and t_0 = 0 fixed. From the two fits the parameters listed in 5.2 are obtained. These parameters allow you to calculate the different Q's, where Q_{int} is retrieved by the use of equation 2.45. This gives (a) $Q_{\text{int}} = 8.1{\cdot}10^4 \pm 4 \cdot 10^3$ and (b) Q_{int} = 288.1±0.3.

The results of the S_{11} simulations in QUCS of the 2-port case with port 1 resistively coupled for *offcenter* = 0.0 and -0.5 mm are presented by the blue dots in Figure 5.14a and Figure 5.14b, respectively. These data-sets were fitted by means of equation 2.47 with A = 1 and t_0 = 0 fixed and are thus not part of the fit parameter, but ϕ_0 is. This makes it different to the ideal case of equation 2.44 and is needed to take care of the wrongly (and constant) chosen reference phase by the simulation. From the shape of the graphs in Figure 5.14 you can see why. The graphs show in both cases (*offcenter* = 0.0 and -0.5 mm) an almost symmetric peak instead of a symmetric dip, meaning that ϕ_0 is about π off. From the fit we obtained the red lines in the figures and the following values for the fit parameters including their corresponding uncertainties (standard deviations) coming from the error in the fit:

***offcenter* (mm)**	**0.0**	**-5.0**
f_0	9.993115 GHz ± 4 kHz	9.992828 GHz ± 0.02 MHz
η	0.9907 ± 0.0005	0.2737 ± 0.0002
$\kappa/2\pi$	13.271 MHz ± 9 kHz	47.757 MHz ± 43 kHz
ϕ_0	0.9972 ± 0.0001 π	1.0261 ± 0.0001 π

Table 5.2

where you can see that the resonance frequency f_0 is indeed equal to the calculated 10.0 GHz and that the phase shift is close to π. What we can see from the fit is that both for *offcenter* = 0.0 and -0.5 mm the fit nicely follows the data which is reflected in the small standard deviations. Still, for *offcenter* = -0.5 where the peak is much broader you can see that the left 'tail' is a bit off. This has to do with the multiple resonances of the cavity that are not taking into account into the fit-function of equation 2.47 as it is derived from the single resonance of the capacitively coupled *RLC*-circuit. We only showed the S_{11} simulation for when the DC-port is on center and furthest away from center to give you a clear idea, even though there are 199 more simulations for every other value of *offcenter*.

From the S_{11} fits and with the use of equation 2.35 we calculated Q_{int} for every value of *offcenter* as shown in Figure 5.15a by the black curve. The curve shows a sharp peak reaching its maximum close to zero *offcenter*. Why Q_{int} reaches its maximum there is because of the two types of internal losses the one associated with the DC-port is minimal. This is what you would expect based on the working principles of the CP as discussed in the Theory section 2.1.3. Where at resonance f_0 a full standing wave exists with its voltage node occurring at the center of the cavity (*offcenter* = 0), preventing any signal to leave the cavity via anything connected there. However, Q_{int} does not reach its maximum exactly at *offcenter* = 0, but at 0.57 μm as made visible by the zoom-in of Figure 5.15b and which is indicated by the red cross. But when we take the uncertainties of the fit into account (see Figure 5.15d) we see that both *offcenter* = 0.57 μm and *offcenter* = 0 attain the same value $Q_{\text{int}} = 8.1 \cdot 10^4 \pm 4 \cdot 10^3$. Therefore we cannot tell if the maximum of Q_{int} is really off-center or not.

To get a sense of what the consequence is of picking the wrong position of the center port (i.e. a position *offcenter* $\neq$ 0) we will check when the resonator regarded as good (~ 100,000) drops down one and when it drops down two ratings (see section 5.1). However, its maximum of Q_{int} is close but not equal to 100,000 we take instead 10% and 1% of $8.1 \cdot 10^4$ for respectively a decent and a bad rating. From Figure 5.15a it is evident that its Q_{int} deteriorates upon moving the DC-port away from the center of the cavity. And that it deteriorates fast in the shown range of 0.5 mm to either side of the center, which is 1/60 of the total length (here equal to the electrical length). When we move the DC-port 87 μm from its center position we end up with a Q_{int} = $8.44 \cdot 10^3 \pm 5 \cdot 10$ on the left and $8.47 \cdot 10^3 \pm 4 \cdot 10$ on the right. At this point our resonator is about a tenth of its maximum value and no longer regarded as a good resonator but a decent one. The point where the resonator reaches roughly a hundredth of its maximum Q_{int} and becomes poor is at *offcenter* = 0.29 mm with Q_{int} = 846.0±0.3 and 848.5±0.1 for respectively left and right.

Next we will simulate the other type of coupling, the capacitive one, shown in Figure 4.5 of Method section 4.2.2. For this set-up we perform the same simulation as described in the second paragraph of this subsection, again with port 3 closed off. Different to the simulation there, we now used for *offcenter* 203 points with 161 points linearly spaced between -0.1 and 0.1 mm and the other 44 points spaced similarly between the remaining range. Furthermore for the range of the S-parameter we did something similar using the same type of spacing with 1001 points for 9.9-10.1 GHz and for the rest of the frequencies we used the remaining 1002 points.

The results of the S_{11} simulation of the 2-port set-up with port 1 capacitively coupled for *offcenter* = 0.0 and -0.5 mm are presented by the blue dots in Figure 5.16a and Figure 5.16b, respectively. Here we used a slightly different fit as we did for the previous case, where we now included t_0 as a fit parameter and only fixed A (= 1) in equation 2.47. We included t_0 to take care of the approximately linear slope of the phase as shown in the grey dotted line in Figure 5.16b. This linear slope is caused by the input capacitor for the simple reason that it did not occur for the resistive coupling. This has to do with the addition of the frequency dependent impedance of the capacitor as opposed to having only a resistor. How this linear slope of the phase affects the real part is most clearly seen in again Figure 5.16b. Here the real part seems to have just like the phase an overall linear shape, but because of the used linear phase term this is actually fitted by a cosine with a significantly larger period than the shown range. By applying the fit we obtained the following values for the fit parameters including their uncertainties:

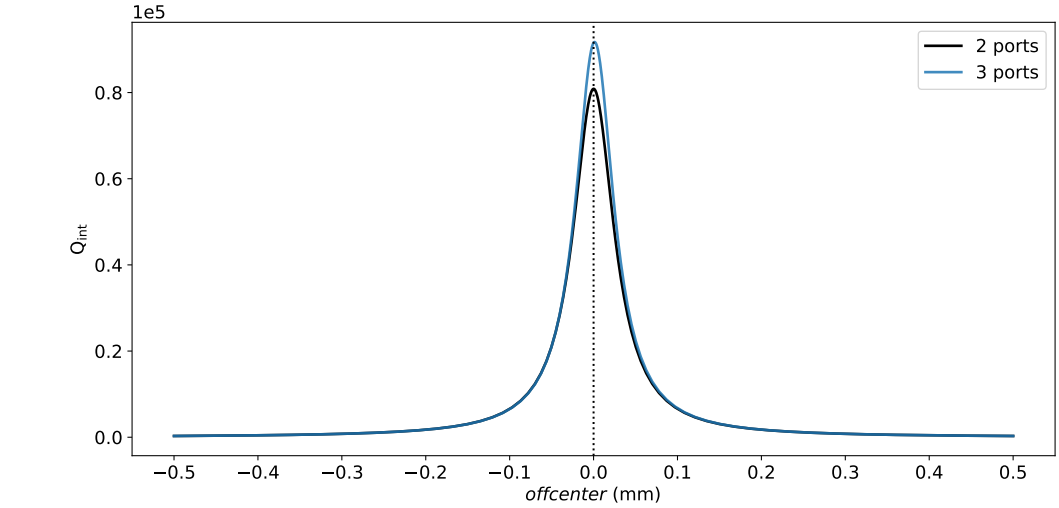

(a)

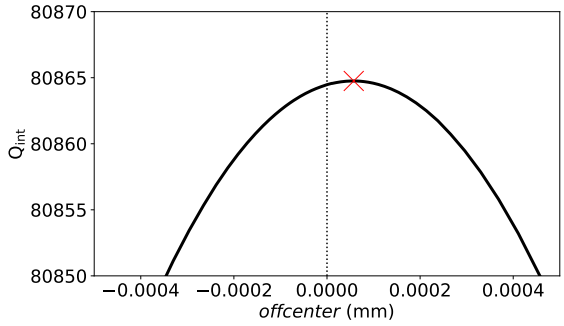

(b)

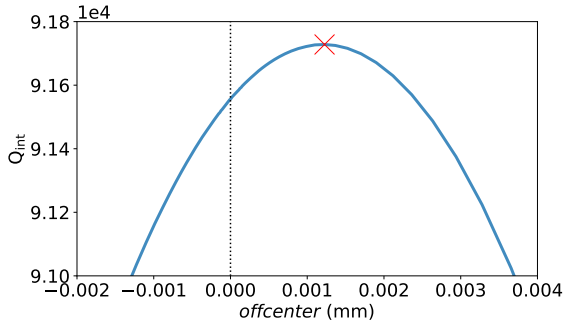

(c)

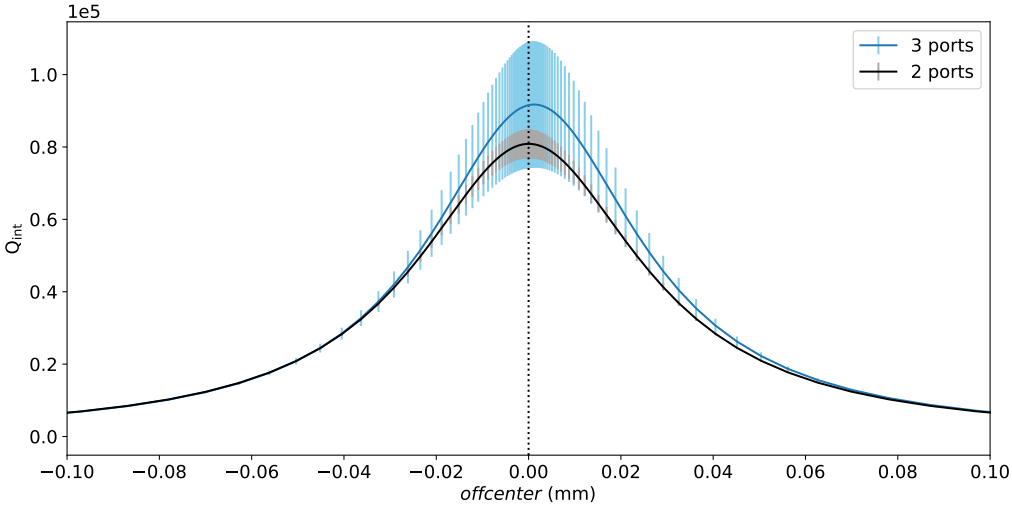

(d)

Figure 5.15: (a) Comparison of the two resistively coupled CP setups shown in Figure 4.4 with $R3 = 10$ EΩ (black) and 5 kΩ (blue). The values of Q_{int} are obtained from the fits of the S_{11} simulations in QUCS, where in Figure 5.14 two of those S_{11} fits are shown for the black graph. Zoom-in (b) and (c) allow to see the slightly off-center of the maximum simulated Q_{int} which is indicated by the red cross. (d) A different zoom-in of (a) showing the uncertainty resulting from the fit error by error-bars.

***offcenter* (mm)**	**0.0**	**-5.0**
f_0	9.98694001 GHz ± 0.01 kHz	9.98867 GHz ± 0.02 MHz
η	0.90499 ± 0.00002	0.03327 ± 0.00005
$\kappa/2\pi$	1.28122 MHz ± 0.04 kHz	35.51 MHz ± 0.08 MHz
ϕ_0	0.0021 ± 0.0002	0.024 ± 0.003
t_0	-0.003050 ± 0.000004	-0.00342 ± 0.00005

Table 5.3

where the parameters were used to fit the data as shown by the red lines in 5.16. Again the one furthest away from the center (see Figure 5.14b) follows the data worse for the same reason as before. The reason being that the fit-function does not take multiple resonances into account. So when the dip/peak becomes broader the resonances start to overlap.

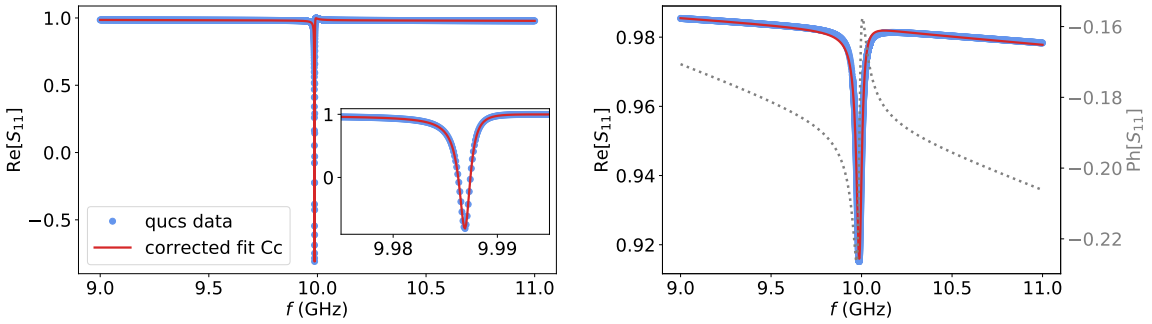

(a) (b)

Figure 5.16: QUCS S_{11} simulation of the 2 ports CP setup (capacitively coupled AC-port) as shown in Figure 4.5 with $R3$ = 10 EΩ for *offcenter* equalling (a) 0.0 and (b) -0.5 mm. The fits are obtained by means of equation 2.47 only A = 1 fixed. From the two fits the parameters listed in 5.3 are obtained. These parameters allow you to calculate the different Q's, where Q_{int} is retrieved by the use of equation 2.45. This gives (a) $Q_{\text{int}} = 8.204{\cdot}10^4 \pm 2 \cdot 10$ and (b) $Q_{\text{int}} = 291.0{\pm}0.7$.

For the S_{11} fits just shown and for 201 more values of *offcenter* ranging from -0.5 to 0.5 mm the Q_{int} is determined with the relation shown in equation 2.35 and plotted in black in Figure 5.17. Similar to the previous case is the maximum of Q_{int} not centered around zero, which is clearly visible from the inset of the figure. It is now on the left and even further away from its center as it is also visible in the full frequency range. At *offcenter* = -9 µm it obtains its maximum $Q_{\text{int}} = 9.084{\cdot}10^4{\pm}2{\cdot}10$, while at *offcenter* = 0 it obtains $Q_{\text{int}} = 8.204{\cdot}10^4{\pm}2{\cdot}10$. Different to the resistive coupler, where its maximum fell inside its uncertainty, is that we can clearly say its maximum Q_{int} is off-center.

As to why the maximum of Q_{int} is not on center is probably because of the AC-port. It adds an capacitance (C_c) to the cavity, altering the natural frequency (ω_0) of the system according to equation 2.5. And because the resonance frequency (ω_r) is closely related to the natural frequency by equation 2.12 it changes the resonance as well. From the equation you might expect that the resistance of the port $R1$ will affect ω_r too as it determines the damping ratio ζ occurring in the formula. However, the effect of ζ, and therefore $R1$, on ω_r is arguably much smaller than that of C_c. This has to do with the fact that for a good (high-Q) resonator ($Q \sim 10^5$) its damping ratio is small ($\zeta = 0.5{\cdot}10^{-6}$), where we used equation 2.37. To see how ω_r looks for small ζ we Taylor expand equation 2.12 up to third order, resulting in:

$$\omega_r = \omega_0 - 2\omega_0\zeta^2 + \mathcal{O}(\zeta^4) \tag{5.5}$$

where we can see that the lowest order for ζ appears to be ζ^2 and because ζ itself was already small this ζ^2 will be very small ($2.5{\cdot}10^{-11}$ for a good resonator). Therefore, to a good approximation $\omega_r \approx \omega_0$, where ω_0 with the inclusion of C_c will have the following form:

$$\omega_0 = \frac{1}{\sqrt{L(C + C_c)}} \tag{5.6}$$

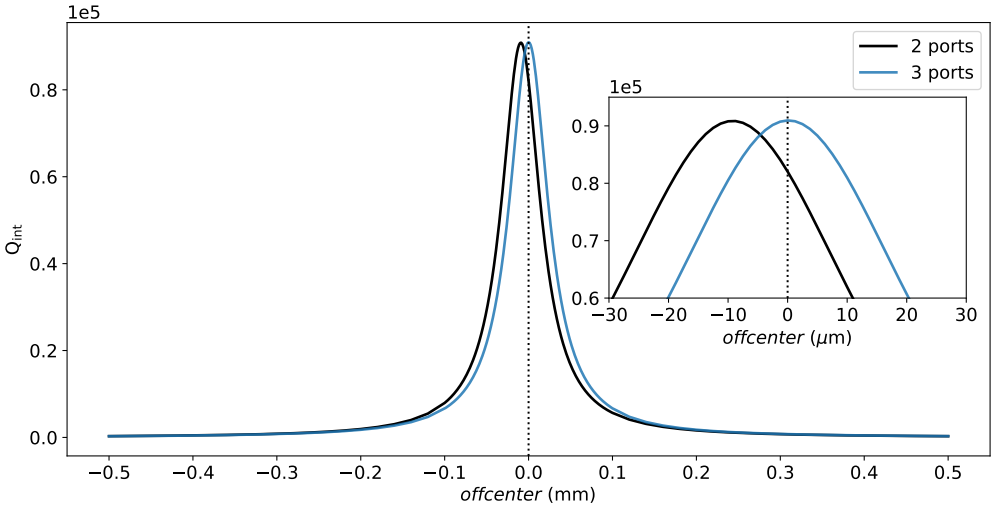

Figure 5.17: Comparison of the two CP (capacitively coupled) setups shown in Figure 4.5 with Rc = 10 EΩ (black) and 0 Ω (blue). The values of Q_{int} are obtained from the fits of the S_{11} simulations in QUCS, where in Figure 5.16 two of those S_{11} fits are shown for the black graph. In the inset a zoom-in of the maxima of the graphs is shown, which allows you to better see that for the 2 ports its off-center while for 3 ports its on center.

where L and C represent the RLC equivalence of the TL simulated cavity. Of course, it is not that by changing the resonance by the additional capacitance alone that the position of the peak in Q_{int} is affected. But not only does the input port add a capacitance, it also adds it asymmetrically as the port only occurs on one side of the cavity. In this way it could very well cause the resonance to shift in such a way that its standing wave is not symmetric anymore to the center port, but with a voltage node, say just on the right of it. If that is the case, then the maximum of Q_{int} will no longer be at *offcenter* = 0 and will be shifted to *offcenter* ≠ 0.

By comparing the maximum Q_{int} to its value at its center position we see that it is already quite off, and that is the case when you picked the right position for the DC-port. To see what happens if you get it wrong, we will just as before check for which value of *offcenter* the resonator becomes decent (10% max Q_{int}) and when it becomes bad (1% max Q_{int}). Q_{int} drops down to roughly 10% of its maximum to Q_{int} = 9035±6 (left) and 9117±6 (right) becoming a decent resonator for *offcenter* = -93 μm and reaching this lower rating for a smaller distance away from center at 75 μm. The resonator becomes poor, reaching 1% of the maximum Q_{int}, at *offcenter* = -300 and 280 μm with Q_{int} = 838±2 and 853±1, respectively.

What we have seen in this subsection is that none of the two types of 2-port resonators, resistive and capacitive, have their Q_{int} right in the center of the cavity at *offcenter* = 0. Although for the capacitive coupler this is certainly the case, for the resistive coupler, however, we cannot tell. The reason why we cannot tell is because the value of Q_{int} at the center falls well inside the uncertainty of the obtained maximum Q_{int} a distance 0.57 μm away from the center. What we can say is that both resonators deteriorate fast on small deviations from their center positions, but keep in mind that this holds for a non-isolated (50 ω) bias line. For the resistive case going from a good resonator (Q_{int}~ 100,000) to a decent resonator (10% max Q_{int}) for only 87 μm away to either side of the center, which is about 0.3% of its electrical length. The capacitive coupler is even a bit more sensitive to its center position degrading to a decent resonator for a mere 75 μm to the right. Although this has to do with the fact that its maximum Q_{int} occurs further away from the middle of the cavity and not with how Q_{int} changes for *offcenter*. Still, it remains a question if it is likely that one would end up with a DC-port that is off-center by roughly 100 μm or more. For example the e-beam would be at worst off by about 100 nm. However, it does show that it is sensitive to its center position and that the margin for error is small. Moreover for the capacitive coupler even if the DC-port is positioned exactly in the middle of the cavity you end up with just 90% of its maximum Q_{int}. You could try to position the port right on its maximum Q_{int}, but this would be very hard to accomplish as it is not known beforehand where the maximum lays. In the next subsection we will have a look if adding an additional port will do and if it will, due to symmetry in the ports, put the maximum Q_{int} of the capacitive coupler back where it belongs, right at the center of the cavity.

5.5.2. Influence of the presence of a third port on Q_{int} of the Center-Port device

In the previous subsection we observed an asymmetry in the Q_{int} for the 2-port setup with a capacitively coupled AC-port (see Figure 4.5 for $Rc = 10^{19}\ \Omega$), where its maximum was not found in the center of the cavity. A possible, and most likely, cause could be the connection of a single input port consisting of a coupling capacitance (C_c) on just one side of the cavity creating an asymmetry (the only asymmetry of the CP design). To check this we will add an additional AC-port in symmetry with the already existing one, making the design completely symmetric.

In order to examine the effect of adding an extra symmetric AC-port to the CP we will simulate the set-up's used in the former subsection of Figure 4.4 and Figure 4.5 but now with $R3 = R1$ and $Rc = 0\ \Omega$, and determine its Q_{int} for every value of *offcenter*. Apart from opening up port 3 ($R3 = R1$ and $Rc = 0$) the simulations are identical and therefore we refer for the details to subsection 5.5.1. Furthermore, the results of the S_{11} simulations will not be shown here as they are really similar to results discussed in the aforementioned subsection. What is however different, is the way to calculate the Q_{int} from these S_{11} simulations in order to relate the 2-ports of subsection 5.5.1 to the 3-ports discussed here.

To calculate the Q_{int} for the 3 ports and make them comparable to the 2-port setups we need to subtract the loss associated with port 3 in terms of the decay rate κ_3 from the internal loss κ_{int} along the lines of Theory section 2.5.2. The reason for this is that by determining the Q_{int} from S_{11} we only consider the loss of port 1 (κ_1) to be external (κ_{ext}). Therefore we are incorrectly attributing the loss of port 3 to the internal loss. So we need to extract κ_3 from κ_{int}, but in order to do so we first need to determine κ_3. This we do by using the simulation of the reflection of port 3 S_{33} instead of S_{11} we used before. From this simulation, which is apart from the port identical to the S_{11} simulation, the κ_{ext} we get is equal to κ_3 and shown in red by Figure 5.18. In blue we displayed the κ_{ext} we get from S_{11} (κ_1) for comparison. Both κ_1 and κ_3 make up the external loss of the 3-port setup. The most important thing the graphs show is that κ_1 and κ_3 are not equal, what you might have expected based on the fact that the ports are identical, and do depend on the position the ports are connected. This means that we could not just subtracted κ_1 twice.

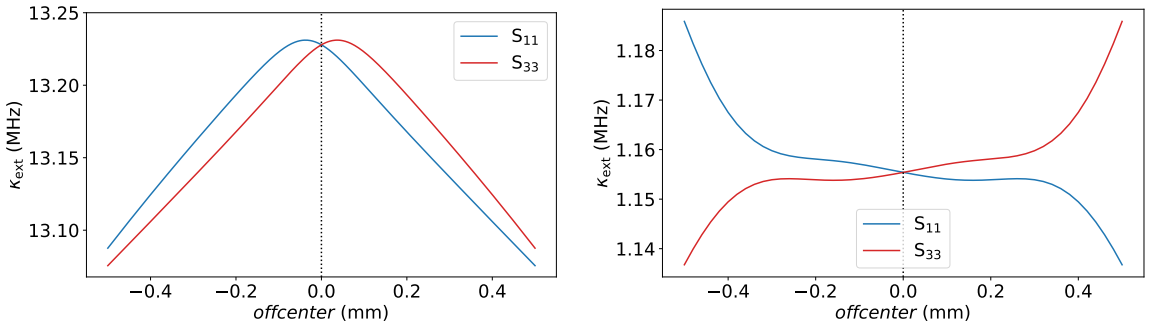

(a) (b)

Figure 5.18: Comparison between the two contributions to the external loss κ_{ext}, one attributed to port 1 (blue) and the other coming from port 3 (red). (a) κ_{ext} retrieved from the fit of the corresponding S-parameter QUCS simulation of the 3 ports ($R3 = 5\ \text{k}\Omega$) resistively coupled CP (see Figure 4.5) and (b) the 3 ports ($Rc = 0\ \Omega$) capacitively coupled CP. Two point of κ_{ext} related to the S_{11} fits for both types of coupling, resistive and capacitive, are shown in Figure 5.14 and Figure 5.16, respectively. From two of the parameters, κ and η, obtained from the S-parameter fits κ_{ext} ($= \eta\kappa$) is obtained.

Now that we established the correct way to determine Q_{int} for the 3-port case we finally are in the position to figure out the Q_{int} dependence on *offcenter* and compare it to the 2-port case. By combining the results of the fits of the S_{11} and S_{33} simulations we obtain for the resistive and capacitive 3 ports resonators, respectively the blue graph shown in Figure 5.15 and in Figure 5.17. From the results of the former figure, the resistive coupler, Q_{int} reaches a maximum $Q_{\text{int}} = 9{\cdot}10^4 \pm 2{\cdot}10^4$ at *offcenter* $= 1.2\ \mu$m. Again, as was the case for the 2 ports, is that Q_{int} reaches its maximum at a point away from the center of the cavity, but for the same reason as before we cannot say for certain if its maximum lies off-center or not. Once more the reason being its uncertainty, where at *offcenter* $= 0$ the maximum Q_{int} falls well inside its uncertainty. This can clearly be seen from Figure 5.15d showing the error in the data in light blue bars. Another thing to notice is that the maximum of Q_{int} of the 3 ports is significantly larger than that of its two ports counter part. But here as well it is due to its uncertainty that we cannot know if it is really larger. From the same figure you see that the error-bars of the 3-port case cover both the data and the uncertainty of the 2-port case. The reason why the errors for the

3 ports are much larger than for the 2 ports has to do with the fact that for the former two fits are used where for the latter only one is used.

For the other type of coupling, the capacitive one, we can see from the results (blue) in Figure 5.17 that it looks like Q_{int} reaches its maximum at the center of the cavity. This is indeed the case, at *offcenter* = 0 the 3-port capacitive coupled resonator obtains its maximum, $Q_{\text{int}} = 9.095 \cdot 10^4 \pm 7 \cdot 10$. That it reaches it maximum at the center is especially clear from the inset of the figure (note that for the capacitive coupler there are no error-bars plotted, the reason being that they would be too small to see). What this means is that for capacitive coupling adding an additional AC-port in symmetry with the existing one fixes the problem where the maximum of Q_{int} occurs away from its center. Also, it does what was initially expected in subsection 5.5.1 and it therefore makes the argued cause even more plausible. The cause being the asymmetry in the capacitance due to the position of the AC-port.

In summary, in this subsection we saw that it could be beneficial to use an additional AC-port in symmetry to the existing asymmetric one for the CP. However, for the resistive coupled resonator we cannot tell, it could be that it does nothing at all. On the other hand, for capacitive coupling it puts the maximum of Q_{int} where we want it to be, on center. This can be advantageous in practice as you would in that case know were its maximum is supposed to be, whereas without the extra port you would not. In that last case you will either have to settle for a lower than possible Q_{int} or try to find where it will end up being, which could be extremely hard to figure out.

5.5.3. Discussion: realization of a symmetry insensitive Center-Port design by isolation of the DC bias line

Even though the shift of the voltage node (inferred from the maximum of Q_{int}) away from the center of the cavity caused by an asymmetrically connected capacitance was fixed by adding an extra port in symmetry to the existing one (see subsection 5.5.2), it is not hard to imagine that other asymmetries (e.g. imperfect boundary conditions) can potentially occur in practice. This, in combination with the observed sensitivity of the resonators performance (Q_{int}) to the position of its bias line (see Figure 5.17), could quite possibly significantly degrade the Q of the CP.

To be less reliant on connecting to the exact location of the symmetry points of the cavity mode, it is common practice to isolate the DC line by making its input impedance on resonance as high as possible. For the CP isolation is done by a meander-line inductor (see Theory section 2.1.3) for which we achieved an impedance of only $\sim 90\ \Omega$ as shown in subsection 5.4.2. Using the same type of isolation were Chen et al. [17] with the DP, where our design is based upon, doing a slightly better job reaching an impedance of $\sim 150\ \Omega$ for a spiral inductor. In comparison the results discussed and shown in this section are based on a galvanically coupled DC-port without any isolation corresponding to an impedance of $50\ \Omega$ which is not substantially lower than that of CP and DP. This means that the isolation they offer is marginal and therefore their dependence on the position of the bias line for both resonators will not be drastically different than that of Figure 5.17. And thus for their performance they still rely heavily on the symmetry points of the cavity.

Luckily, there are several ways to reach much higher input impedances and by that achieving much better isolation. One of the approaches, already discussed in subsection 5.4.2, is by reducing the cross-section of the wire making up the inductor in order to increase its kinetic inductance as suggested by Annunziata et al.[44]. This allows, without any radical changes to the design, to significantly increase the inductance, while staying sufficiently far away from its SRF. They reported 105 nH for a $5 \times 5\ \mu$m meandering wire of l = 105 μm with a SRF of 37 GHz ($\gg f_0 \sim 7$ GHz). This means that at $f_0 \sim 7$ GHz it obtains an impedance of approximately 4.6 kΩ, an impressive 30 and 50 times larger than that of the DP and the CP, respectively. There appears however to be a limit to how thin you can make the wire, at a diameter of the order ~10 nm the superconductor seems to be starting to break down due to thermal and quantum fluctuations [46, 47]. From a practical point of view, as the thickness of the film reduces it becomes increasingly hard to make reproducible devices. Furthermore, chances of structural disordering as well as the role of proximity effects will increase leading to a reduced penetration depth [48].

Yet another way to realize isolation of the bias line is by making use of a band-stop filter as described by Li et al. [19]. The filter is made of a quarter wave ($\lambda/4$) TL in order to function as a impedance inverter [27]. It is actually really similar to the inductors discussed above, but rather than staying clear of the SRF it exploits those impedance 'sweet spots' (see Figure 5.11) in a controlled manner. By doing so they acquire an effective impedance at resonance of approximately 80 kΩ, much higher than achieved by both Chen's and our inductor. Remarkably, its impedance is so large that even if the bias line is connected to the worst possible point on the cavity (voltage antinode) it still provides good isolation. Its Q reduces only to 84 % of

the Q achieved at its ideal point (voltage node). This goes to show, that its reliance on the position of the DC line is, to say at least, minimal. Do keep in mind that for the filter to produce such a large impedance, the impedance of the external circuitry of the filter should be sufficiently small. Moreover, as we already saw in Figure 5.11 these high impedance 'sweet spots' are only obtained in a narrow band of frequencies. Outside these frequencies you will end up with impedances orders of magnitude lower as was the case for the meander-line inductor of the fabricated CP with an impedance of only $\sim 90\ \Omega$. Therefore isolation by a $\lambda/4$ band-stop filter is only guaranteed for a limited frequency band, hence the name.

These two suggested isolation methods provide the means to the CP to become more or less resilient to the position of its bias line. However, it is still recommended to position the DC-port as close as possible to the ideal symmetry point of the cavity in order to minimize the leakage and acquire the highest possible Q. But if you are a bit off its ideal point, because of the design, fabrication, operation or whatever the reason that causes asymmetries in the cavity mode, these high impedance isolations ensure you that the resonator will not noticeably degrade.

6

Conclusion

From the initial QUCS simulations of the Center-Port resonator (CP) it looked promising achieving $Q_{\text{int}} \sim$ 40,000. Of course this is in its most ideal environment, but it demonstrated that in principle it should work. Despite that, the cryogenic S_{21} reflection measurement showed a drastically lower Q_{int} of only $2.6{\cdot}10^2 \pm 1{\cdot}10$ at its full-wave resonance frequency f_0 = 6.98 GHz. Upon inspection of the meander-line inductor of the DC bias line, we discovered from the Sonnet simulations that it operates well above its self-resonance frequency, with a corresponding impedance of $\sim 90\ \Omega$ at f_0. Therefore is the inductor unable to block off high-frequency signals, leaving the microwave field free to decay into the bias line. By examining the transmission from the input port to the bias line S_{31}, recovered form the S_{32} measurement, and relating it to the reflection S_{21}, we obtained at resonance a transmission of about 6 %. Although this is still a significant amount of loss considering the low value of Q_{int}, it certainly is not the main source of loss. This leaves the only other option, internal loss of the cavity itself. What is actually causing this bad internal loss remains a guessing game. It is most likely due to suboptimal fabrication, because it is not typical for NbTiN superconducting coplanar waveguide (CPW) resonators too achieve such a low Q [10]. What this means, is that we cannot say much specifically about the CP design from these simulations and measurements. Only, that fabrication of such a resonator is perhaps not as straightforward as we might have thought.

To do obtain some useful insights in the CP design, we checked how its DC port's position affects Q_{int} in QUCS. We saw for both a resistively as well as a capacitively (CP) coupled AC input port that Q_{int} is very sensitive to the position of the galvanically connected DC port. It drops down to 10 % of its maximum for less than 0.1 mm away from its center, a mere 0.3% of its total length. Remarkably, for the capacitive case the maximum $Q_{\text{int}} = 9.084{\cdot}10^4 \pm 2{\cdot}10$ did not occur on center, where you expect the voltage node to be, but 9 μm away from it, to the input port. The most likely cause seems to be the asymmetric addition of the coupling capacitance directly (first-order) affecting the resonance and shifting the voltage node. To make this argument more appealing, adding an extra AC-port in symmetry to the existing one moves the maximum back to the center of the cavity. Still, it does not change the fact that it is very important for the performance of the resonator to connect the bias line on, or at least very close to, the voltage node. Which, as mentioned above, are not always at expected locations.

In order to rely less on the position of the cavity the bias line is connected to, it is common practice to isolate the DC line by making its input impedance on resonance as high as possible [17][19]. Based on the spiral inductor of Chen et al.[17], we used a meander-line inductor in order to form a high impedance point. For the latter we reached an impedance of only $\sim 90\ \Omega$, while Chen did only a little bit better achieving $\sim$ 150 Ω. Although, these impedances could be sufficient to isolate the DC-line up till a near-perfect voltage node ($Q > 10^3$ [17]), they arguably still rely heavily on the symmetry points of the cavity as their impedances are close to being galvanic (50 Ω). Based on this, we would not recommend to turn to the CP as opposed to designs that intrinsically do not rely on symmetry to apply a DC-bias [18][20]. Its potentially simpler design does not weigh against its high sensitivity to the location of its bias-line.

Fortunately, it is possible to achieve sufficiently high impedances by making use of $\lambda/4$ band-stop filters, for which Li et al. [19] obtained an effective impedance at resonance of approximately 80 kΩ. By connecting these filters to the worst possible points (voltage antinodes) with the Q reducing only from 18,300 (voltage node) to 15,320, they showed that its resonator's reliance on the position of the bias-line is, to say at least, minimal. While this makes the cavity independent of its bias-line position, it only allows for high enough

impedances in a limited band of frequencies. Therefore, we would like to propose another way of isolation for the CP, which is much closer to its original design, and that is by reducing the cross-section of the wire making up the inductor and thereby increasing its kinetic inductance, as suggested by Annunziata et al.[44]. In this way, they realized a meander-line inductor of 105 nH ($\sim$ 4.6 kΩ at f = 7 GHz) with a self resonant frequency (SRF) of 37 GHz. And thus, as long as you stay well below its SRF, it will allow for the application of a DC-bias that does not rely too much on the exact location of the symmetry points of the cavity.

This goes to show, that despite the CP being arguably inferior to resonators that do not rely on symmetry points, with the proposed alterations the CP could be a viable option. Baring, even with these alterations, the potential of a simpler design. Besides, investigation of the proposed isolations could very well lead to better performing inductors along the way, which is interesting on its own . Along the same lines, reducing the cross-section of the resonator could, furthermore, lead to possibly higher Q resonators with high resilience to magnetic fields [49].

Bibliography

[1] T. Lindström, J. E. Healey, M. S. Colclough, C. M. Muirhead, and A. Ya. Tzalenchuk. Properties of superconducting planar resonators at millikelvin temperatures. *Phys. Rev. B*, 80:132501, Oct 2009. doi: 10.1103/PhysRevB.80.132501. URL https://link.aps.org/doi/10.1103/PhysRevB.80.132501.

[2] J. J. Viennot, M. C. Dartiailh, A. Cottet, and T. Kontos. Coherent coupling of a single spin to microwave cavity photons. *Science*, 349(6246):408–411, 2015. ISSN 0036-8075. doi: 10.1126/science.aaa3786. URL https://science.sciencemag.org/content/349/6246/408.

[3] B. D'Anjou and Guido Burkard. Optimal dispersive readout of a spin qubit with a microwave resonator. *Phys. Rev. B*, 100:245427, Dec 2019. doi: 10.1103/PhysRevB.100.245427. URL https://link.aps.org/doi/10.1103/PhysRevB.100.245427.

[4] P. Scarlino, D. J. van Woerkom, U. C. Mendes, J. V. Koski, A. J. Landig, C. K. Andersen, S. Gasparinetti, C. Reichl, W. Wegscheider, K. Ensslin, T. Ihn, A. Blais, and A. Wallraff. Coherent microwave-photon-mediated coupling between a semiconductor and a superconducting qubit. *Nature Communications*, 10(1):3011, Jul 2019. ISSN 2041-1723. doi: 10.1038/s41467-019-10798-6. URL https://doi.org/10.1038/s41467-019-10798-6.

[5] Mika A. Sillanpää, Jae I. Park, and Raymond W. Simmonds. Coherent quantum state storage and transfer between two phase qubits via a resonant cavity. *Nature*, 449(7161):438–442, Sep 2007. ISSN 1476-4687. doi: 10.1038/nature06124. URL https://doi.org/10.1038/nature06124.

[6] J. Majer, J. M. Chow, J. M. Gambetta, Jens Koch, B. R. Johnson, J. A. Schreier, L. Frunzio, D. I. Schuster, A. A. Houck, A. Wallraff, A. Blais, M. H. Devoret, S. M. Girvin, and R. J. Schoelkopf. Coupling superconducting qubits via a cavity bus. *Nature*, 449(7161):443–447, Sep 2007. ISSN 1476-4687. doi: 10.1038/nature06184. URL https://doi.org/10.1038/nature06184.

[7] A. Wallraff, D. I. Schuster, A. Blais, L. Frunzio, R.-. S. Huang, J. Majer, S. Kumar, S. M. Girvin, and R. J. Schoelkopf. Strong coupling of a single photon to a superconducting qubit using circuit quantum electrodynamics. *Nature*, 431(7005):162–167, Sep 2004. ISSN 1476-4687. doi: 10.1038/nature02851. URL https://doi.org/10.1038/nature02851.

[8] M. Göppl, A. Fragner, M. Baur, R. Bianchetti, S. Filipp, J. M. Fink, P. J. Leek, G. Puebla, L. Steffen, and A. Wallraff. Coplanar waveguide resonators for circuit quantum electrodynamics. *Journal of Applied Physics*, 104(11):113904, 2008. doi: 10.1063/1.3010859. URL https://doi.org/10.1063/1.3010859.

[9] Peter K. Day, Henry G. LeDuc, Benjamin A. Mazin, Anastasios Vayonakis, and Jonas Zmuidzinas. A broadband superconducting detector suitable for use in large arrays. *Nature*, 425(6960):817–821, Oct 2003. ISSN 1476-4687. doi: 10.1038/nature02037. URL https://doi.org/10.1038/nature02037.

[10] R. Barends. *Photon-detecting superconducting resonators*. PhD thesis, TU Delft, 6 2009.

[11] C. A. Regal, J. D. Teufel, and K. W. Lehnert. Measuring nanomechanical motion with a microwave cavity interferometer. *Nature Physics*, 4(7):555–560, Jul 2008. ISSN 1745-2481. doi: 10.1038/nphys974. URL https://doi.org/10.1038/nphys974.

[12] T. Rocheleau, T. Ndukum, C. Macklin, J. B. Hertzberg, A. A. Clerk, and K. C. Schwab. Preparation and detection of a mechanical resonator near the ground state of motion. *Nature*, 463(7277):72–75, Jan 2010. ISSN 1476-4687. doi: 10.1038/nature08681. URL https://doi.org/10.1038/nature08681.

[13] Yulin Wu, Li-Ping Yang, Ming Gong, Yarui Zheng, Hui Deng, Zhiguang Yan, Yanjun Zhao, Keqiang Huang, Anthony D. Castellano, William J. Munro, Kae Nemoto, Dong-Ning Zheng, C. P. Sun, Yu-xi Liu, Xiaobo Zhu, and Li Lu. An efficient and compact switch for quantum circuits. *npj Quantum Information*, 4 (1):50, Oct 2018. ISSN 2056-6387. doi: 10.1038/s41534-018-0099-6. URL https://doi.org/10.1038/s41534-018-0099-6.

[14] Songyuan Zhao, Stafford Withington, David Goldie, and Chris Thomas. Suppressed-gap millimetre wave kinetic inductance detectors using dc-bias current. https://arxiv.org/abs/2001.09089v2, 03 2020.

[15] K. D. Petersson, L. W. McFaul, M. D. Schroer, M. Jung, J. M. Taylor, A. A. Houck, and J. R. Petta. Circuit quantum electrodynamics with a spin qubit. *Nature*, 490(7420):380–383, Oct 2012. ISSN 1476-4687. doi: 10.1038/nature11559. URL https://doi.org/10.1038/nature11559.

[16] Fei Chen, Juliang Li, A. D. Armour, E. Brahimi, Joel Stettenheim, A. J. Sirois, R. W. Simmonds, M. P. Blencowe, and A. J. Rimberg. Realization of a single-cooper-pair josephson laser. *Phys. Rev. B*, 90:020506, Jul 2014. doi: 10.1103/PhysRevB.90.020506. URL https://link.aps.org/doi/10.1103/PhysRevB.90.020506.

[17] Fei Chen, A. J. Sirois, R. W. Simmonds, and A. J. Rimberg. Introduction of a dc bias into a high-q superconducting microwave cavity. *Applied Physics Letters*, 98(13):132509, 2011. doi: 10.1063/1.3573824. URL https://doi.org/10.1063/1.3573824.

[18] Sal J. Bosman, Vibhor Singh, Alessandro Bruno, and Gary A. Steele. Broadband architecture for galvanically accessible superconducting microwave resonators. *Applied Physics Letters*, 107(19):192602, 2015. doi: 10.1063/1.4935346. URL https://doi.org/10.1063/1.4935346.

[19] Shao-Xiong Li and J. B. Kycia. Applying a direct current bias to superconducting microwave resonators by using superconducting quarter wavelength band stop filters. *Applied Physics Letters*, 102(24):242601, 2013. doi: 10.1063/1.4808364. URL https://doi.org/10.1063/1.4808364.

[20] Yu Hao, Francisco Rouxinol, and M. D. LaHaye. Development of a broadband reflective t-filter for voltage biasing high-q superconducting microwave cavities. *Applied Physics Letters*, 105(22):222603, 2014. doi: 10.1063/1.4903777. URL https://doi.org/10.1063/1.4903777.

[21] S. E. de Graaf, D. Davidovikj, A. Adamyan, S. E. Kubatkin, and A. V. Danilov. Galvanically split superconducting microwave resonators for introducing internal voltage bias. *Applied Physics Letters*, 104(5):052601, 2014. doi: 10.1063/1.4863681. URL https://doi.org/10.1063/1.4863681.

[22] S. Heyminck, B. Klein, R. Güsten, C. Kasemann, A. Baryshev, J. Baselmans, S. Yates, and T. M. Klapwijk. Development of a mkid camera for apex. page 262, 2010. Twenty-First International Symposium on Space Terahertz Technology, held March 23-25, 2010 at Oxford University's Said Business Center and the STFC Rutherford Appleton Laboratory, Oxford, UK. National Radio Astronomy Observatory (NRAO), 2010 ; Conference date: 23-03-2010 Through 25-03-2010.

[23] Y.-Y. Liu, J. Stehlik, C. Eichler, M. J. Gullans, J. M. Taylor, and J. R. Petta. Semiconductor double quantum dot micromaser. *Science*, 347(6219):285–287, 2015. ISSN 0036-8075. doi: 10.1126/science.aaa2501. URL https://science.sciencemag.org/content/347/6219/285.

[24] D Bothner, M Knufinke, H Hattermann, R Wölbing, B Ferdinand, P Weiss, S Bernon, J Fortágh, D Koelle, and R Kleiner. Inductively coupled superconducting half wavelength resonators as persistent current traps for ultracold atoms. *New Journal of Physics*, 15(9):093024, sep 2013. doi: 10.1088/1367-2630/15/9/093024. URL https://doi.org/10.1088%2F1367-2630%2F15%2F9%2F093024.

[25] Wikipedia contributors. Center tap, November 2019. URL https://en.wikipedia.org/wiki/Center_tap.

[26] Richard C. DiPrima William E. Boyce. *Elementary Differential Equations and Boundary Value Problems*, chapter Second Order Linear Equations, pages 195–209. John Wiley & Sons, 9th edition edition, 2010. ISBN 9780470398739.

[27] David M. Pozar. *Microwave Engineering*. John Wiley & Sons, University of Massachusetts at Amherst, fourth edition edition, 2012.

[28] Miloslav Čapek, Lukas Jelinek, and Pavel Hazdra. On the functional relation between quality factor and fractional bandwidth. *IEEE Transactions on Antennas and Propagation*, 63, 11 2014. doi: 10.1109/TAP.2015.2414472.

[29] Daniel Bothner. Daniel's response functions of lumped element and transmission line resonators [internal document], February 2016. URL https://nas-steelelab.tnw.tudelft.nl/SteeleLabWiki/index.php?title=Response_Functions_of_Cavities.

[30] Inder Bahl Ramesh Garg and Maurizio Bozzi. *Microstrip Lines and Slotlines*, chapter Coplanar Lines: Coplanar Waveguide and Coplanar Strips, pages 351–359. Microwave & RF. Artech House, 2013. ISBN 9781608075362. URL https://books.google.nl/books?id=1PQfAgAAQBAJ.

[31] G. Ghione and C. U. Naldi. Coplanar waveguides for mmic applications: Effect of upper shielding, conductor backing, finite-extent ground planes, and line-to-line coupling. *IEEE Transactions on Microwave Theory and Techniques*, 35(3):260–267, Mar 1987. ISSN 1557-9670. doi: 10.1109/TMTT.1987.1133637.

[32] W. Hilberg. From approximations to exact relations for characteristic impedances. *IEEE Transactions on Microwave Theory and Techniques*, 17(5):259–265, May 1969. ISSN 1557-9670. doi: 10.1109/TMTT.1969.1126946.

[33] G. Hasnain, A. Dienes, and J. R. Whinnery. Dispersion of picosecond pulses in coplanar transmission lines. *IEEE Transactions on Microwave Theory and Techniques*, 34(6):738–741, Jun 1986. ISSN 1557-9670. doi: 10.1109/TMTT.1986.1133427.

[34] Raj Das and Avishek Chanda. *Fabrication and Properties of Spin-Coated Polymer Films*, pages 283–306. Springer, 09 2016. ISBN 978-3-319-39713-9. doi: 10.1007/978-3-319-39715-3_10.

[35] Justin Henrie, Spencer Kellis, Stephen Schultz, and Aaron Hawkins. Electronic color charts for dielectric films on silicon. *Optics express*, 12:1464–9, 05 2004. doi: 10.1364/OPEX.12.001464.

[36] Wikipedia contributors. Reactive-ion etching, November 2019. URL https://en.wikipedia.org/wiki/Reactive-ion_etching.

[37] ALLRESIST GmbH, September 2018. URL https://www.allresist.com/.

[38] D. J. Thoen, B. G. C. Bos, E. A. F. Haalebos, T. M. Klapwijk, J. J. A. Baselmans, and A. Endo. Superconducting nbtin thin films with highly uniform properties over a ∅ 100 mm wafer. *IEEE Transactions on Applied Superconductivity*, 27(4):1–5, June 2017. ISSN 1051-8223.

[39] Sonnet Software Inc. 3d planar high-frequency electromagnetic software, October 2019. URL http://www.sonnetsoftware.com/products/sonnet-suites/index.html.

[40] Sonnet Software Inc. Adaptive band synthesis (abs), October 2019. URL http://www.sonnetsoftware.com/products/sonnet-suites/ef_abs.html.

[41] D. P. Pappas, M. R. Vissers, D. S. Wisbey, J. S. Kline, and J. Gao. Two level system loss in superconducting microwave resonators. *IEEE Transactions on Applied Superconductivity*, 21(3):871–874, June 2011. ISSN 2378-7074.

[42] Felix E. Schmidt, Mark D. Jenkins, Kenji Watanabe, Takashi Taniguchi, and Gary A. Steele. A ballistic graphene superconducting microwave circuit. *Nature*, 06 2018.

[43] M Goppl, A Fragner, M Baur, R Bianchetti, Stefan Filipp, Johannes Fink, Peter Leek, G Puebla, Lars Steffen, and Andreas Wallraff. Coplanar waveguide resonators for circuit quantum electrodynamics. *Journal of Applied Physics*, 104:113904 – 113904, 01 2009. doi: 10.1063/1.3010859.

[44] Anthony J Annunziata, Daniel F Santavicca, Luigi Frunzio, Gianluigi Catelani, Michael J Rooks, Aviad Frydman, and Daniel E Prober. Tunable superconducting nanoinductors. *Nanotechnology*, 21(44):445202, oct 2010. doi: 10.1088/0957-4484/21/44/445202. URL https://doi.org/10.1088%2F0957-4484%2F21%2F44%2F445202.

[45] E.B. Rosa and United States. National Bureau of Standards. *The Self and Mutual Inductances of Linear Conductors*, volume 4 of *Bulletin of the Bureau of Standards*. U.S. Department of Commerce and Labor, Bureau of Standards, 1908. URL https://books.google.nl/books?id=xGDWeXOFwpYC.

[46] Maciek Zgirski, Karri-Pekka Riikonen, Vladimir Touboltsev, and Konstantin Arutyunov. Size dependent breakdown of superconductivity in ultranarrow nanowires. *Nano Letters*, 5(6):1029–1033, Jun 2005. ISSN 1530-6984. doi: 10.1021/nl050321e. URL https://doi.org/10.1021/nl050321e.

[47] A.D. Zaikin and D. Golubev. *Dissipative Quantum Mechanics of Nanostructures: Electron Transport, Fluctuations, and Interactions*. Jenny Stanford Publishing, 2019. ISBN 9781000024203. URL https://books.google.nl/books?id=qKWaDwAAQBAJ.

[48] Alexey Gubin, Konstantin Ilin, SA Vitusevich, Michael Siegel, and N. Klein. Dependence of magnetic penetration depth on the thickness of superconducting nb thin film. *Physical Review B*, 72, 08 2005. doi: 10.1103/PhysRevB.72.064503.

[49] N. Samkharadze, A. Bruno, P. Scarlino, G. Zheng, D. P. DiVincenzo, L. DiCarlo, and L. M. K. Vandersypen. High-kinetic-inductance superconducting nanowire resonators for circuit qed in a magnetic field. *Phys. Rev. Applied*, 5:044004, Apr 2016. doi: 10.1103/PhysRevApplied.5.044004. URL https://link.aps.org/doi/10.1103/PhysRevApplied.5.044004.

[50] Artiom van den Broek. Josephson junctions made by atomic layer deposition. Master's thesis, TU Delft, 5 2019.

[51] T. Zijlstra, C. F. J. Lodewijk, N. Vercruyssen, F. D. Tichelaar, D. N. Loudkov, and T. M. Klapwijk. Epitaxial aluminum nitride tunnel barriers grown by nitridation with a plasma source. *Applied Physics Letters*, 91 (23):233102, Dec 2007. ISSN 1077-3118. doi: 10.1063/1.2819532. URL http://dx.doi.org/10.1063/1.2819532.

Appendices

A

Supplementary Material

A.1. Resist etch rates in O_2 and SF_6/O_2 plasmas

Resist		Before etch		Plasma			After etch	
Type	Recipe	Expected Allresist (nm)	Profiler (nm)	O2 flow (sccm)	SF6 flow (sccm)	Etch time (s)	AFM Δ(m)	Etch rate (nm/s)
ARP 6200.18	4000 rpm, 4min 155C	800	806	20	0	90	673	1.47
				13.5	5	30	765	1.36
ARN 7700.18	8000rpm, 2min 85C	300	297	20	0	90	191	1.17
				13.5	5	30	278	0.65
PMMA 950 A3	4000rpm, 2min 195C	130	91	20	0	90	0	1.01*
				13.5	5	30	0	3.03*

Table A.1: Extension of Table 3.1 shown in Fabrication Process & Techniques chapter 3 with the addition of the negative and positive tone resist ARN and PMMA, respectively. Where the resist is applied by means of spin coating and baking on a hot plate. The etch rates are obtained from the difference between the height measured before etching (Profiler) and after (atomic force microscope (AFM)), etched by the VLL Leybold F3 etcher. Note that for the PMMA no true etch rates are obtained, but lower bounds (indicated by *). The expected heights are retrieved from Allresist [37].

A.2. Cryogenic reflection S_{21} measurement of the CP

A.2.1. Analysis and comparison of the S_{21} fit for ϕ_0 fixed and variable

To check how well the reflection S_{21} DIY4K measurement data of the CP is fitted by equation 2.47 (with t_0 = 0), the magnitude, phase and imaginary part are shown (see Figure A.1) in addition to the real part. The data shown in the figure is corrected for by both a constant phase as well as a time delay, determined by a linear fit of the phase of S_{21} as shown in Results Figure5.6 by means of equation 5.1. Of the shown fits in Figure A.1 only the real part is actually fitted, from which the relevant fit parameters (ω_0,κ and η) are obtained, which in turn determine the Q's (Q, Q_{int} and Q_{ext}). From these fit parameters the imaginary part is taken and the magnitude and phase are derived from the real and imaginary part. By extending the form in which S_{21} is displayed you are able to see if the fit obtained from the real part agrees with the other forms, as it should.

Based on this extended view we decided to fix one of the fit parameters, the constant reference phase ϕ_0, which is actually already fitted for by the linear fit of the phase. As can be seen from the phase in Figure A.1 is that allowing ϕ_0 to vary results in an offset that does not correspond with the data. The data does not appear to have any offset anymore and therefore setting $\phi_0 = 0$ seems to be appropriate. Although, for the Q_{int} in this case it does not really matter if the ϕ_0 is fixed or not, because both the linewidth and the the resonance frequency differ only marginally between the two, which can been seen from the magnitude.

A.2.2. Q_{int} dependence on the VNA power

The DIY4K reflection S_{21} measurements of the CP where performed for different input powers of the VNA and is made visible in Figure A.2 for the Q_{int}. Q_{int} is derived from equation 2.45, where the variables are obtained by fitting the data by means of equation 2.47 (ϕ_0 and t_0 are retrieved from a linear fit in the phase of S_{21} (see Figure 5.6)). The power shown is, however, not the power that reaches the cavity. What does reach the cavity is the VNA power that is both attenuated by a directional coupler (-20 dB) as well as any dissipations of the wire that lead to the cavity. From the figure it is quite clear that Q_{int} is not very sensitive to the input power

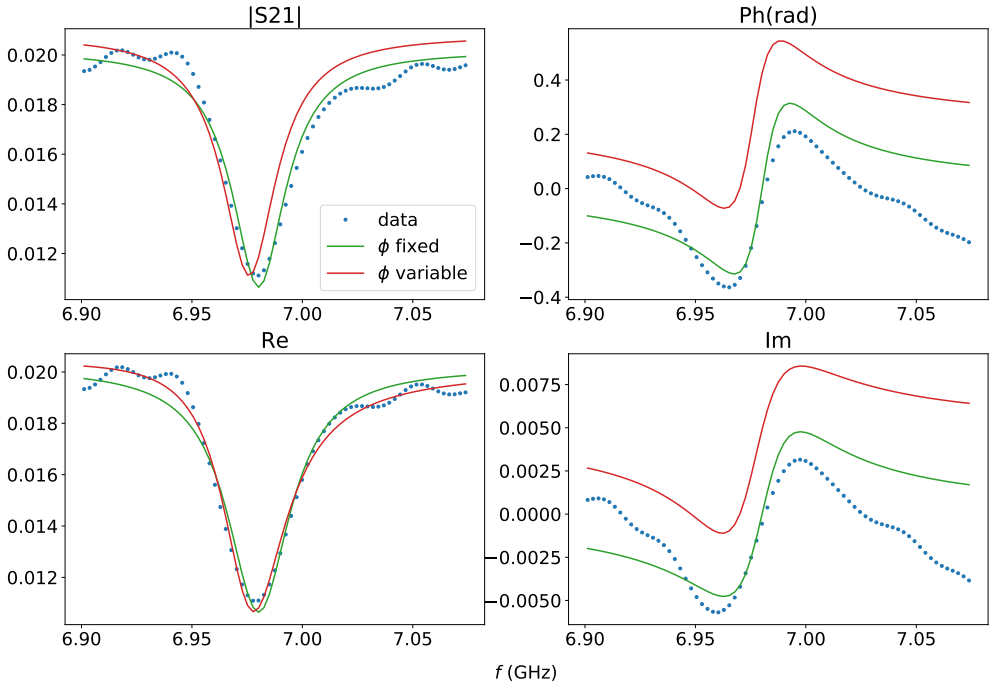

Figure A.1: The magnitude, phase, real and imaginary part of the cryogenic (DIY4K) measured reflection parameter S_{21} of the CP. S_{21} is corrected for by both a constant phase and a time delay as obtained from a linear fit of the phase of S_{21} (see Figure 5.6 and equation 5.1). The data points indicated by blue dots are fitted by equation 2.47 in Theory chapter 2, where the constant reference phase (ϕ_0) is fixed $\phi_0 = 0$ (green) and variable (red). Only the data of the real part is fitted, where the imaginary part is taken from the same set of parameters. Then, the magnitude and phase are derived from the real and imaginary part.

of the VNA, being almost constant and varying within the boundaries of the uncertainty. Then, to a good approximation Q_{int} is equal to its mean of 263 ± 2.2 for the measured range of powers, where the uncertainty (u_{mean}) is taken by:

$$u_{\text{mean}} = \frac{\sqrt{\sum_i u_{\text{i}}^2}}{N}$$

where u_{i} is the uncertainty of every individual Q_{int} with N number of Q_{int} data points.

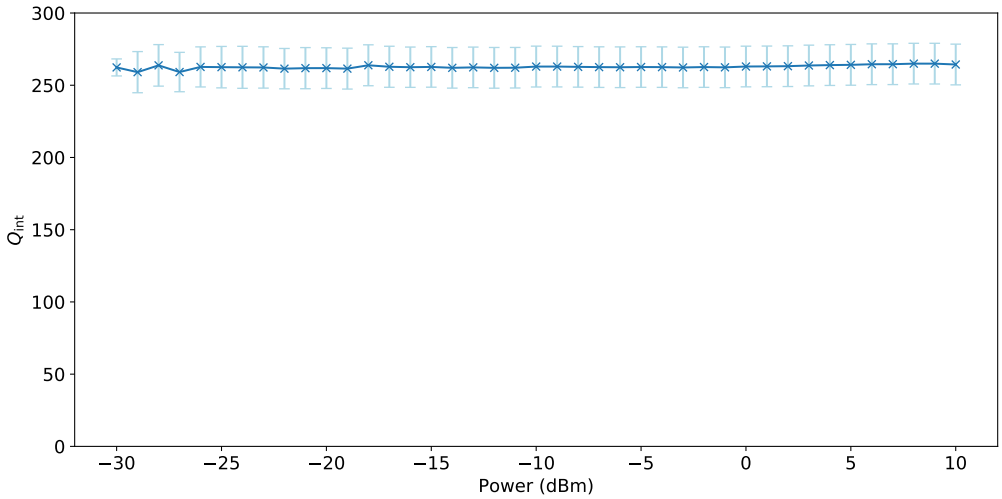

Figure A.2: Q_{int} obtained from the reflection (S_{21}) DIY4K measurement of the CP by means of equation 2.45 and 2.47, where ϕ_0 and t_0 are retrieved from a linear fit in the phase of S_{21} (see Figure 5.6). In addition, the errorbars coming from the fit parameters, and not the measurement, are displayed in light blue for every Q_{int}. For -30 dBm six measurements were taken, resulting in a smaller error. The shown power is not the power that reaches the cavity of the CP, but it is the power delivered by the VNA. Of that power only a fraction reaches the cavity as it is both attenuated by a directional coupler (-20 dB) and any dissipations of the wire that lead to the cavity.

From Figure A.3 you can see how the power affects the shape of S_{21}. It can be seen from the figure that Figure A.3a is more smooth than Figure A.3b probably due to lower noise. However, the noise does not really change the shape of the dip and that is why Q_{int} is to a high degree independent of the measured range of VNA powers.

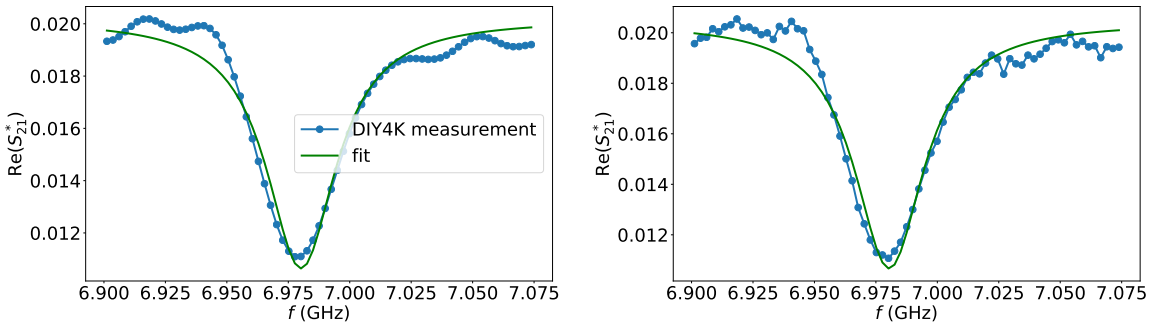

(a) (b)

Figure A.3: Phase corrected (*, see section 5.3) real part of the reflection parameter S_{21} of the CP for two different VNA powers, 10 dBm (left) and -30 dBm (right). The fit (green) is obtained from equation 2.47, where ϕ_0 and t_0 are retrieved from a linear fit in the phase of S_{21}.

A.3. Determination of attenuation factor as used in QUCS of the initial CP design

To make the QUCS simulation more realistic, losses of the transmission lines are implemented in the form of an attenuation factor, α = 1.00484 m^{-1}. This value for α comes from the 0.006073 m^{-1} found by Schmidt et al.[42] for their device, making use of MoRe. Where they extracted α by taking several cavity measurements and fitting the fundamental mode resonances. The reason for the difference between the two factors is due to the different mediums they were used in, and the conversion that QUCS uses. QUCS considers the medium to be vacuum with the frequency given as:

$$f = \frac{c}{\lambda} = \frac{1}{\sqrt{\mu_0 \epsilon_0}} \frac{1}{\lambda} \tag{A.1}$$

where c the speed of light and λ the wavelength. Furthermore μ represents permeability and ϵ the permittivity, with 0 indicating vacuum. However, for α = 0.006073 m^{-1} the waves do not travel in vacuum but through a different medium, this changes the speed accordingly:

$$v = \frac{1}{\sqrt{\mu\epsilon}} = \frac{1}{\sqrt{\mu_0 \mu_r \epsilon_0 \epsilon_r}} = \frac{c}{\sqrt{\mu_r \epsilon_r}}$$

here the 'r' denotes the relative component which is dependent on the material. This means that it is like the wave travels through a larger cavity. And as the effective length thus increases the attenuation factor has to decrease:

$$\alpha_0 = \frac{\alpha}{\sqrt{\mu_r \epsilon_r}} \tag{A.2}$$

with α_0 the attenuation factor in vacuum. The medium on the chip that is used consist of a coplanar waveguide and can be approximated as half of it being air and half of it silicon. For both air and silicon the permeability is the same as in vacuum, so μ_r = 1. What is different, is the permittivity and because of the two different media it can to a very good approximation be averaged (see Theory section 2.6):

$$\epsilon_r = \frac{1}{2}(\epsilon_{silicon} + \epsilon_{air})$$

With $\epsilon_{silicon}$ = 11.68 F/m and ϵ_{air} = 1.00 F/m, resulting in a ϵ_r = 6.34 F/m. Putting this back into equation A.2 gives α_0 = = 0.002412 m^{-1}. Now, using the QUCS conversion:

$$\alpha_{QUCS} = e^{2\alpha_0}$$

And there you have it, the attenuation factor of 1.00484.

B

Off-topic: fabrication proposal and design of ALD Josephson junctions and SQUIDs

B.1. Fabrication proposal of NbTiN-AlN-NbTiN Josephson junctions

We present here a fabrication proposal of NbTiN-AlN-NbTiN Josephson junctions (JJs) as suggested by G.A. Steele, shown in Figure B.1. This proposal actually builds on the results obtained from the Thesis of A. van den Broek [50], where a very low reproducibility of the junctions was observed. Most likely caused by the way the layers of NbTiN-Al_2O_3-NbTiN of the junction were stacked, breaking vacuum after the first layer with the risk of contamination. In order to prevent this, the proposed fabrication forms the trilayer in-situ, which is actually common practice for JJs [51]. Furthermore, with this proposal we also move away from the use of AlO_x to AlN as the insulating barrier. The reason for AlN as opposed to AlO_x is mainly because it appears to be suffering from OH contamination, either by H_2O that is left in the fabrication chamber or by the use of H_2O as a precursor to grow AlO_x. Backed by the promising obtained junctions of Zijlstra et al. [51]. In addition, they report that AlN is a great etch-stop for SF_6/O_2 plasma, which is very handy for the reactive-ion etching (RIE) in the final step of the process (see Figure B.1) since we do not have to worry too much about etching all the way through, till the substrate.

Although the fabrication process is quite clear from Figure B.1, some remarks are in place. First of all, the function of the Si layer is to allow for the desired junction area, acting as an insulator to prevent a short to the top NbTiN layer. Moreover, the fabrication process is pretty extensive consisting of time consuming techniques like the e-beam and the ALD. Although there is a possibility of skipping step 3, saving one e-beam step, by using the trilayer of NbTiN-AlN-NbTiN as alignment markers. However, the trilayer does not produce a high contrast, and therefore manual marker search is needed. But even then, it is hard to find. These markers do play a crucial role as the process relies on sensitive alignment of the pattern, twice. So sensitive even, that it needs alignment accuracy in the order of 100 nm to achieve the desired junction overlap, forming a possible risk.

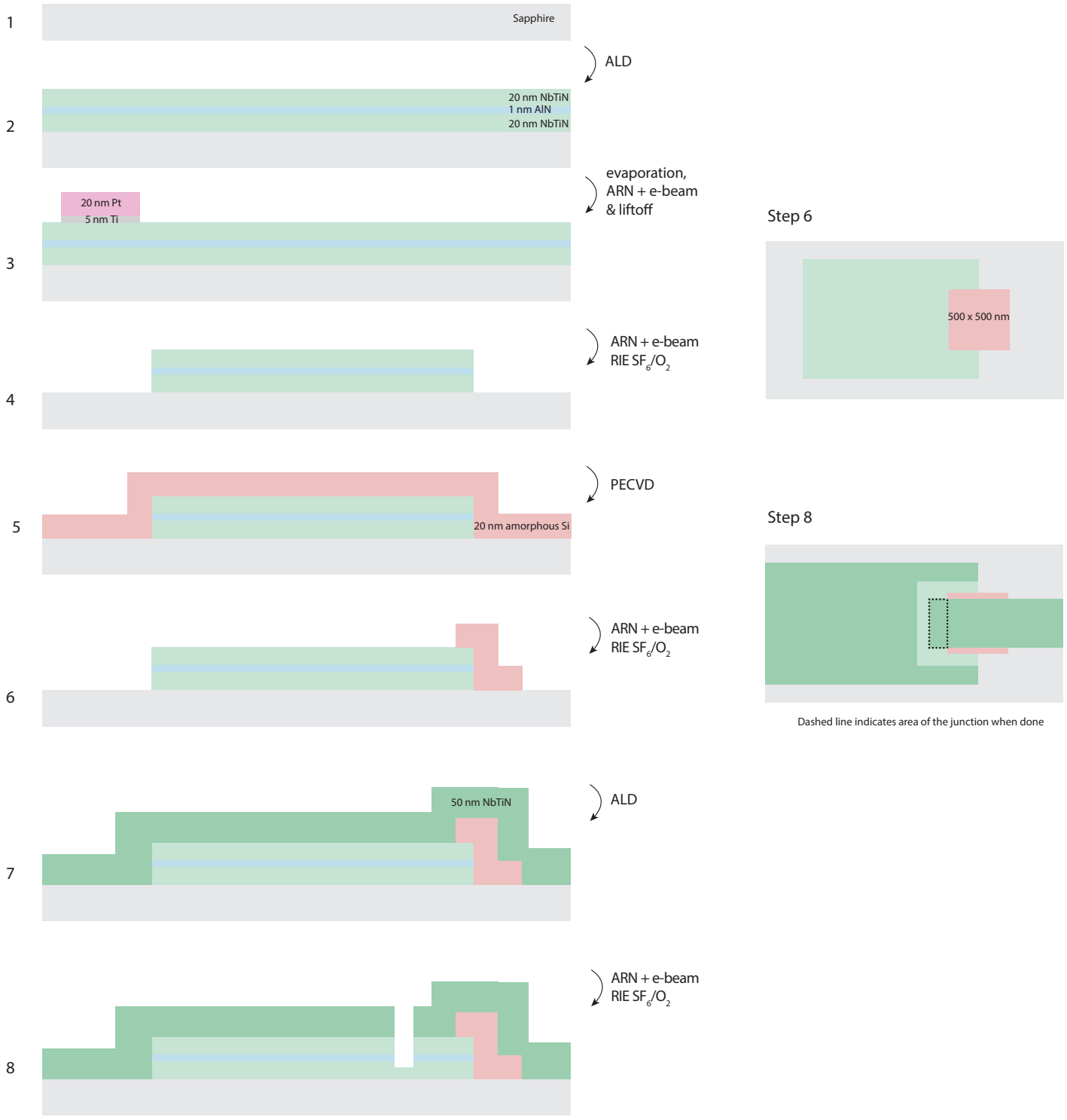

Figure B.1: Slightly modified fabrication proposal of NbTiN-AlN-NbTiN Josephson junctions as suggested by G.A. Steele. It consist of eight fabrication steps of which four are e-beam, four are deposition, and three are removal steps. Prior to all e-beam steps the negative-tone resist ARN is proposed. Deposition is done by three techniques, atomic layer deposition (ALD), evaporation and plasma-enhanced chemical vapor deposition (PECVD). Removal is done either by lift-off or reactive-ion etching. The figures on the left show the cross-section throughout the fabrication process, whereas the two figures on the left show the top view at the corresponding steps. Note that while the Ti/Pt markers are not displayed after step 3, they are not removed in any of the steps and protected by ARN resist.

B.2. Design of Josephson junctions and SQUIDS

Based on the proposed fabrication by G.A. Steele (Figure B.1), the design of JJs and SQUIDs shown in Figure B.2 was made. It allows for the fabrication of twelve 1×1 cm chips on a 2-inch wafer (see Figure B.2a) each containing nine different junction areas of either eight JJs or SQUIDs (see Figure B.2b). For every JJ there is one junction area, whereas for the SQUID there are two (see Figure B.2c). Furthermore, the area of junction varies in 17 steps from 100×100 nm to 667×667 nm throughout the wafer. In this way it is possible to test a multitude of JJs and SQUIDs both for a wide variety of different junctions as well as for there reproducibility.

In order to overcome the alignment issues, mentioned in the previous section, or at least make the proposed fabrication of Figure B.1 less sensitive to alignment, two solutions have been implemented in the design. The first one is the hole in the insulating layer (Si, red), which forces the junction area to be constant. Of course, the entire hole should be covered by both the layer underneath (NbTiN) as well as the top layer (NbTiN), while it should remain within the boundaries of the insulator. For the latter part the second solution takes partially care of, by the use of a L-shaped trilayer (NbTiN-AlN-NbTiN). This allows the top-layer to exceed the insulator boundaries along the direction of the top lead. These solutions address both the alignment of step 5-6 (solution 1) and 7-8 (solution 1+2) of the fabrication proposal (see Figure B.1).

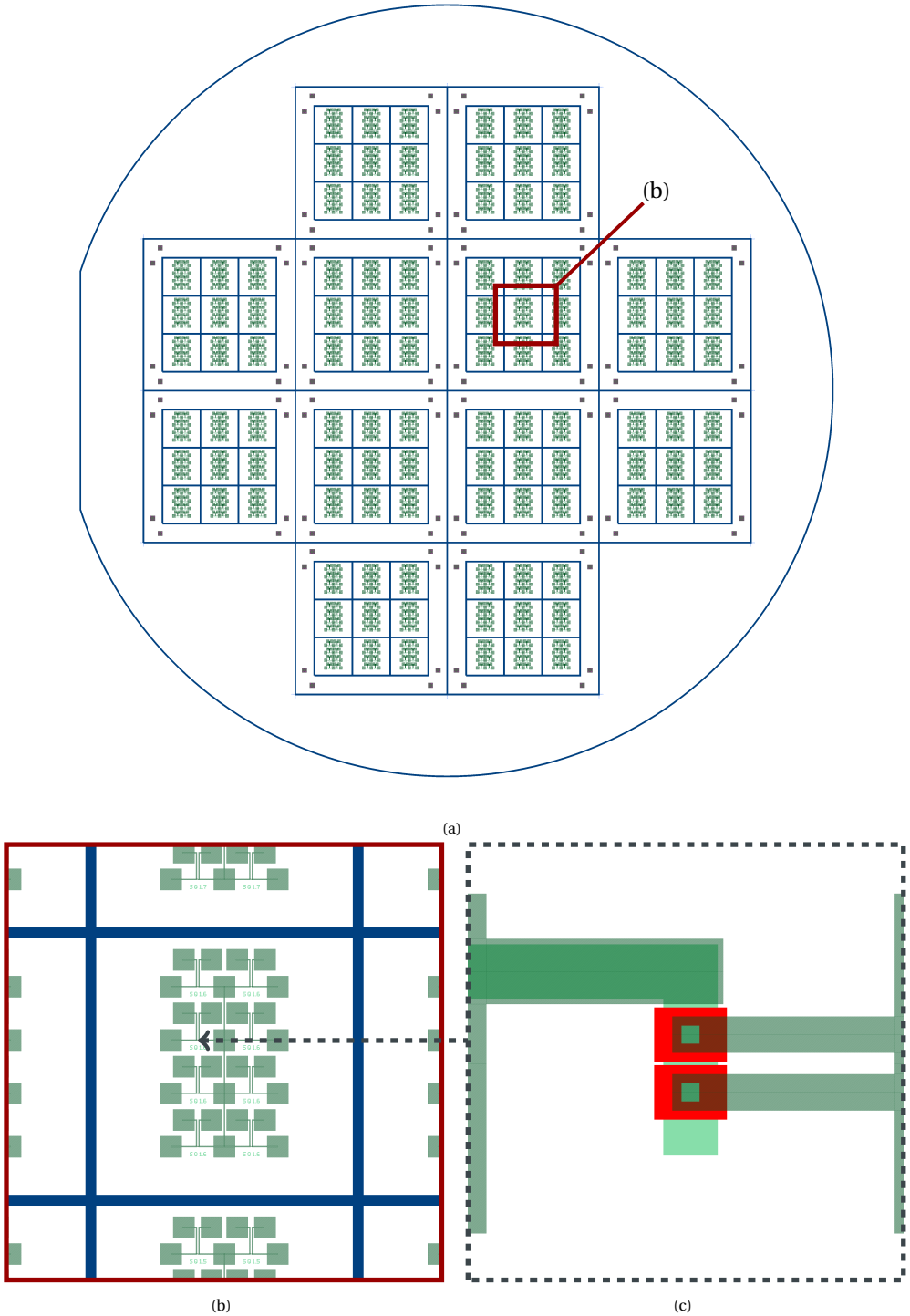

Figure B.2: Design of multiple JJs and SQUIDs based on the fabrication proposal of Figure B.1, where the colors of the SQUID (c) are in correspondence with the proposal. (a) 2 inch wafer composed of twelve 1×1 cm chips, (b) each containing nine different junction areas of either eight JJ or eight SQUIDs, where the junction area (indicated by the square hole in the red part) varies in 17 steps from 100×100 nm to 667×667 nm throughout the wafer. (c) a zoom in of (b) showing a single SQUID, for a JJ there is only one junction area with just one arm leading to the L-shape. The design is based on negative-tone resist, where the written pattern (excluding the frames indicated in dark blue) is supposed to remain after any removal method (e.g. RIE).

B.3. ALD growth of AlN

Although the proposed fabrication and design of the JJs and SQUIDs were never realised, some first steps were made on the growth of AlN in the Ultratech Fiji ALD as shown by Table B.1 and Figure B.3. Based on the recipe of AlN obtained from Ultratech/Cambridge NanoTech (see Figure B.4) and by measuring the thickness after deposition on the Woollam M5000 ellipsometer. This recipe is, however, not recommended to be used with NbTiN at 400 °C (typical), although lower temperatures have been used by the company. Therefore it is advisable to switch to a different material like TiN with a deposition temperature in 270-300 °C (based on recipes by A. Bruno), much closer to the 250 °C of the AlN.

From Figure B.3 a growth rate of 0.053 nm/cycle with a offset of 0.11 nm is obtained from the linear fit (blue) of all the available data points, see Table B.1. However, some of the data points have a relatively high root mean square error (RMSE) of > 24 as shown in the table. For these values it is uncertain if the true minimum of RMSE of the fit is obtained and therefore if they are representable or not. These points we excluded for the other fit (green), shown in the figure. This fit gives a slightly higher growth rate of 0.061 nm/cycle with a offset of 0.034 nm closer to zero, where it should be. The growth rate reported by the company is 0.53 Å/cycle equal to 0.053 nm/cycle, which is at least up to two significant numbers exactly the same as the growth rate obtained from the fit of all data points (blue). And thus seems to be growing as expected, potentially even faster (0.061 nm/cycle).

number of cycles	thickness (nm)	thickness uncertainty (nm)	RMSE
0	-0.01	0.003	3.457
5	0.42	0.002	1.864
10	0.68	0.002	2.326
15	1.15	0.002	2.751
20	1.14	0.002	2.725
30	1.57	0.002	2.71
40	2.49	0.004	4.037
50	3.25	0.005	5.966
200	9.46	0.018	24.389
400	21.04	0.016	35.631
600	32.02	0.022	48.972

Table B.1: Deposition of the Ultratech Fiji ALD with thicknesses obtained by measuring with the Woollam M5000 ellipsometer. The thickness is actually a derived parameter and not a fit parameter, where the root mean square error (RMSE) quantifies the 'goodness' of the fit, the lower the better.

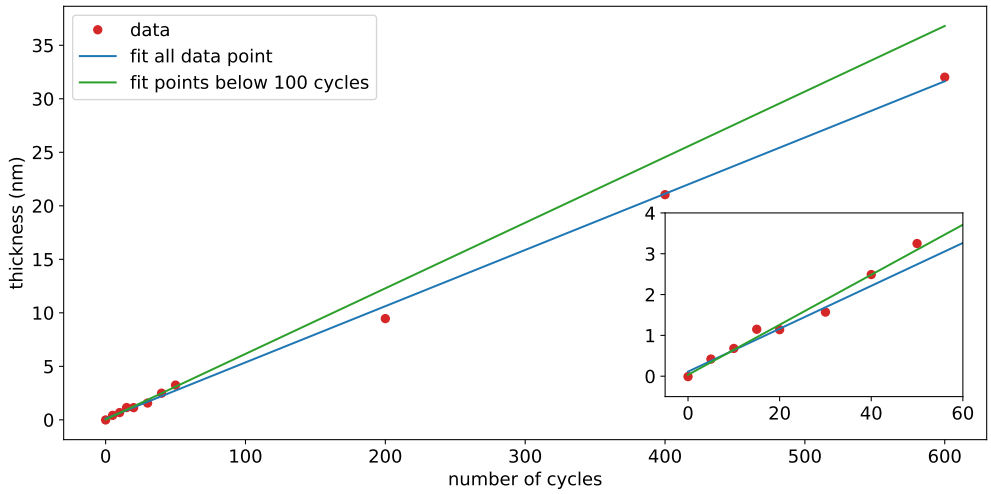

Figure B.3: Plotted data of Table B.1 (red) fitted linearly for all points (blue) and for the points below 100 cycles (green). From the fits growth rates of 0.053 nm/cycle (blue) and 0.061 nm/cycle are obtained with offsets of 0.11 nm (blue) and 0.034 (green).

Plasma AlN with TMA and N_2 Plasma

	INSTRUCTION	CHAN	VALUE	UNITS	COMMENTS
0	flow	0	30	sccm	
1	flow	1	100	sccm	
2	heater	13	250	°C	Upper Reactor Heater
3	heater	14	250	°C	Lower Reactor Heater
4	heater	15	250	°C	Chuck and Wafer Holder
5	heater	16	150	°C	Precursor Delivery Line
6	heater	17	150	°C	ALD Manifold
7	heater	24	150	°C	Exhaust Tee
8	heater	25	125	°C	Exhaust Valve
9	heater	30	150	°C	Load Lock Transfer Tunnel
10	stabilize		see below	sec	Stabilize all heaters
11	mfc valve	2	1	open	Open N2 MFC valve
12	flow	2	50	sccm	N2 Flow
13	turbo purge		0	close	Transition from turbo pumping to non-turbo pumping
14	turbo gate		0	close	
15	turbo iso		0	close	
16	reactor rough		1	open	
17	gate purge		1	open	
18	wait		5	sec	plasma purge
19	pulse	TMA	0.06	sec	TMA Pulse
20	wait		5	sec	TMA purge #1
21	gate purge		0	close	
22	reactor rough		0	close	Transition from non- turbo pumping to turbo pumping
23	turbo iso		1	open	
24	turbo gate		1	open	
27	turbo purge		1	open	
28	wait		5	sec	Gas stabilization
29	plasma		300	watts	
30	wait		20	sec	N2 plasma time
31	plasma		0	watts	
32	goto	13	x	cycles	

Temperature	Growth per cycle (Å/cycle)	Refractive Index	Uniformity (%)
250	0.53	1.99	4

Figure B.4: AlN recipe for the Ultratech Fiji ALD from Ultratech/Cambridge NanoTech.

B.4. Final remarks about ALD

While the ALD seems very attractive, being capable of forming multiple different uniform layers with thicknesses controllable to the size of an atom, we observed first handed that it can be one of the most unreliable deposition machines out there. Its main issue possibly arises from the numerous materials that can be used, which will very likely lead to contamination due to previous deposition inherently leaving material behind in the chamber. Moreover, because of the wide variety of material options the machine becomes significantly more complex and therefore much more sensitive. This increases the changes of different heaters to break down and, worst of all, to the possibility of clogging the line with an unknown composition. Therefore, it is not recommended to use an ALD with more than one metal. Although it is theoretically possible to use more than one, in practice this becomes a real big nuisance.

An alternative to ALD could be magnetron sputtering [51]. This would still allow the proposed fabrication and design, discussed in the first two sections of this chapter, to be used, without the need for the ALD.